Università degli Studi di Napoli "Federico II"

Dottorato in
Fisica Fondamentale ed Applicata

- 20° ciclo -

Lidar remote sensing for the characterization of the atmospheric aerosol on local and large spatial scale

Maria Grazia Frontoso

Coordinatore:
Prof. Gennaro Miele

Tutor:
Prof. Nicola Spinelli
Co-tutors:
Prof. Adolfo Comeron
Dr. Xuan Wang

anno accademico 2006 - 2007

INDEX

Introduction

Climate is changing. The contribution of the aerosols to the climate changes and radiative forcing is not negligible but not well estimated.
Atmospheric aerosols are a significant source of direct and indirect global climate forcing.
As direct effect, aerosols can determine the positive or negative radiative forcing in function of its chemical composition. In fact, aerosols act heating or cooling the Earth's atmosphere with both heating and cooling effects due to scattering and absorption processes of electromagnetic radiation.
The indirect effect involves increased average aerosol number concentration. An increased aerosol population means that there are more cloud condensation nuclei, which would lead to more clouds forming. This situation is slightly more complicated, as the effect of the clouds on the Earth's radiation budget depends upon the cloud height, but increased tropospheric aerosol would also have a cooling effect on the atmosphere.
There is a natural aerosol component consisting mostly of soil dust, sea salt, biogenic sulphates, and organic matter that is geographically and seasonally variable. Major volcanic eruptions such as Pinatubo, which occur infrequently and presumably randomly, inject large amounts of sulphuric compounds into the stratosphere, producing a globally dispersed aerosol that reduces the solar energy input and cools the global climate for a period of several years.
There is also an anthropogenic component that is linked to fossil-fuel and biomass burning, as well as other human activity; this component has been steadily increasing with global industrialization and has been implicated as being responsible for at least partially masking the greenhouse warming due to past greenhouse-gas increases.
Model estimates of the radiative forcing from aerosols are highly uncertain, largely because current capabilities to observe aerosol from space are insufficient to constrain key assumptions in these models. Unfortunately, the strong variability both in space and in time of the aerosols and thus the difficulty to characterize their global basic properties (number concentration, size distribution, chemical composition, optical parameters, etc.) induce large uncertainties in the predictions of the numerical models. A large improvement in the description of aerosol microphysics can be obtained only by measurements. Therefore, more measurements (both *in situ* and remote sensing) are needed.
In the last years, different kinds of atmospheric monitoring techniques (*in situ* and *remote sensing*) have been developed. The remote sensing lidar (**li**ght **d**etection **a**nd **r**anging) technique is a well-established technique to study the vertical profiles of the atmospheric aerosol parameters with high vertical and temporal resolution.
The urban area of Naples is characterized by a large amount of anthropogenic aerosol produced by combustion system and vehicular traffic. Moreover, due to its location, the city of Naples is also characterized by frequent strong presence of Saharan dust carried out from North Africa and by circulation phenomena like land/sea breeze. Therefore, the study and the monitoring of the evolution of aerosols in this area seem to be very interesting.
The present thesis deals with the characterization of the atmospheric aerosol on different spatial scale through the lidar remote sensing technique; numerical models and satellite data have been also used for the present work.
The multiwavelengths Raman lidar system used is located at the Naples lidar station (40°50'N, 14°11'E, 118 m asl).
Since February 2000 the Naples lidar group is part of EARLINET (**E**uropean **A**erosol **R**esearch **LI**dar **NET**work), the European network on aerosol research by lidar measurements. EARLINET provides a quantitative, comprehensive and statistically significant database of the horizontal, vertical and temporal distribution of aerosols on continental scale.

Aerosols on different spatial scales have been investigated:

- *local scale*: Field campaigns have been performed by lidars systems located in different sites in order to study the temporal and spatial evolution of the aerosol optical properties in the

boundary layer and in the free troposphere. Measurements on local scale are very important because they give information generally parameterized by model.

- *synoptic scale:* This research activity has been carried out in the framework of the EARLINET-ASOS (**E**uropean **A**erosol **R**esearch **LI**dar **NET**work – **A**dvanced **S**ustainable **O**bservation **S**ystem) project, in collaboration both with the **U**niversitat **P**olitècnica de **C**atalunya (UPC, Barcelona - Spain) and the **B**arcelona **S**upercomputing **C**enter (BSC, Barcelona - Spain). The synergy between lidar measurements and the **D**ust **RE**gional **A**tmospheric **M**odel (DREAM) model has been investigated in order to study the transport phenomena of the Saharan dust over the Mediterranean basin. The objective of this study was two-fold: (1) evaluate the skills of the model to forecast the Saharan dust vertical distribution in the Mediterranean region and (2) derive and interpret the validated dust model 2-year climatology concerning the Saharan dust vertical distribution. The dependence of the Saharan dust episodes on the driving synoptic pattern has been investigated by cross-comparing patterns of backtrajectories, as well as wind fields, temperature, geopotential and sea level pressure maps. Three synoptic patterns have been found. For each pattern, differences between the dust vertical distribution over the western and central Mediterranean area have been observed. Also the seasonal variation of the Saharan dust concentration over the western and central Mediterranean has been investigated.
- *large scale:* As demonstrated by LITE (**L**idar **I**n-space **T**echnology **E**xperiment) mission of the space shuttle Columbia and ICESat/GLAS (**I**ce, **C**loud and land **E**levation **Sat**ellite/**G**eoscience **L**aser **A**ltimeter **S**ystem) satellite missions, lidars operating from space have a significant ability to profile multi-layer aerosol and cloud structures. This research activity has been carried out in the framework of the CALIPSO (**C**loud-**A**erosol **L**idar and **I**nfrared **P**athfinder **S**atellite **O**bservation) satellite mission (April 2006-April 2009). For space-borne lidars, validation is a central issue to test the confidence level of the satellite data products and thus assure a high quality dataset. For this reason, simultaneous ground-based lidar measurements have been performed in coincident with the satellite's overpasses. To directly compare ground-based and space-borne aerosol lidar products, an algorithm (CESC, **C**ounter-propagating **E**lastic **S**ignals **C**ombination) has been derived. This algorithm permit to retrieve the aerosol backscattering and extinction vertical profiles from simultaneously detected ground and space elastic lidar signals, without any a priori hypothesis on aerosol particles properties. Therefore, the CESC algorithm seems to be a strong methodological contribution for the investigation of global-scale aerosol by spaceborne lidars.
  To test the accuracy of the algorithm, both numerical simulations and its applications to real signals have been performed.

The present thesis is organized into 6 chapters.
The 1st chapter describes the principle of the radiative budget of the Earth and highlights the main agents of the radiative forcing, in particular the direct aerosol radiative forcing. Moreover, the advantages and drawbacks of the *in situ* and remote sensing aerosol measurements are presented briefly.
The 2nd chapter deals with the basic principle of the lidar technique. In order to fully understand this technique, a short overview of the involved physical processes is presented. Rayleigh, Mie and Raman scattering are briefly described.
The 3rd chapter describes in details the experimental setup of the Naples LIDAR system. Data treatment and error propagation in the data analysis are discussed.
The 4th chapter deals with the study of aerosol and water vapor on local scale. The Naples - Pontecagnano and the Launch (International **L**indenberg campaign for **A**ssessment of h**U**midity a**N**d **C**loud profiling systems and its impact on **H**igh-resolution modelling) field campaign are presented and discussed.

The 5th chapter deals with the Saharan Dust vertical distribution over the western and central Mediterranean studied by the synergy of LIDAR measurements and the **D**ust **RE**gional **A**tmospheric **M**odel (DREAM). The dependence of the Saharan Dust episodes dynamics on the driving synoptic pattern has been also investigated. Composite patterns of backtrajectories, wind fields, temperature and geopotential maps are analyzed for all the measured SD cases. Furthermore, the seasonal variation of the desert dust aerosol loading above the western and central Mediterranean has been studied.
The 6th chapter describes briefly the CALIPSO (**C**loud **A**erosol **L**idar and **I**nfrared **P**athfinder **S**atellite **O**bservations) project and the EARLINET strategy for CALIPSO validation program. Then, the novel algorithm CESC (**C**ounter-propagating **E**lastic **S**ignals **C**ombination) is described in detail. Results of simulations and the application to real cases are also presented.

Introduction

During the last century the number of natural disasters has increased: floods, tropical cyclones, drought, storms, etc [Houghton, 1997]. There is not any more a doubt that the climate is changing. A vast majority of the world's scientific community estimates that a significant climatic change of anthropogenic source is now evident [Santer, 1995; Houghton, 1997; Shine, 1999; Ramanathan, 2001]. However for some, this evidence is contestable, even equivocal [Lomborg, 2001]. As it is impossible to make full-scale experiments in the atmosphere and as an experiment on a regional scale would hardly make sense because of the complexity of the involved phenomena, numerical models are the only provider of detailed estimates of climate responses and of regional features [de Félice, 2001]. Such model cannot yet simulate all aspects of the climate and there are considerable uncertainties associated with clouds, aerosols and their interactions with radiation [Jennings, 1993; Charlson, 1995; Houghton, 1997; Seinfeld and Pandis, 1998; Kondratyev, 1999; Finlayson-Pitts, 2000; de Félice, 2001].

A key aspect of this problem is the difficulty to characterize the global basic properties of the principal types of aerosol such as the number concentration, size distribution and optical parameters. This difficulty arises from the fact that the most important typical feature of the aerosols is their strong variability both in space and in time [Charlson, 1995; Kondratyev, 1999; Ramanathan, 2001]. To solve this problem it is necessary to improve the set of well-calibrated instruments (both *in situ* and remote sensing) with the ability to measure the changes in stratospheric and tropospheric aerosols amounts and their radiative properties, changes in atmospheric water vapour and temperature distributions, and changes in clouds cover and cloud radiative properties [Charlson, 1995; Ramanathan, 2001].

This chapter describes the principle of the radiative budget of the Earth and highlights the main agents of the radiative forcing, in particular the direct aerosol radiative forcing. Moreover, the advantages and drawbacks of the *in situ* and remote sensing aerosol measurements are presented briefly.

1.1. The Earth-atmosphere system

The Earth-atmosphere system is a vital global environmental segment together with the water and soil.

Some simple consideration of the rate of the incoming solar radiation and the emitted infrared and reflected visible radiation shows which factors are important for the average temperature of the Earth. In the case of long-term global average, the radiation balance has to be zero, i.e. the incoming and outgoing radiation should be equal. With no energy sources within the planet the same amount of the solar radiation S has to be emitted or reflected by the body.

Schematics of the fluxes considered in the following cases are shown in Figure 1-1.

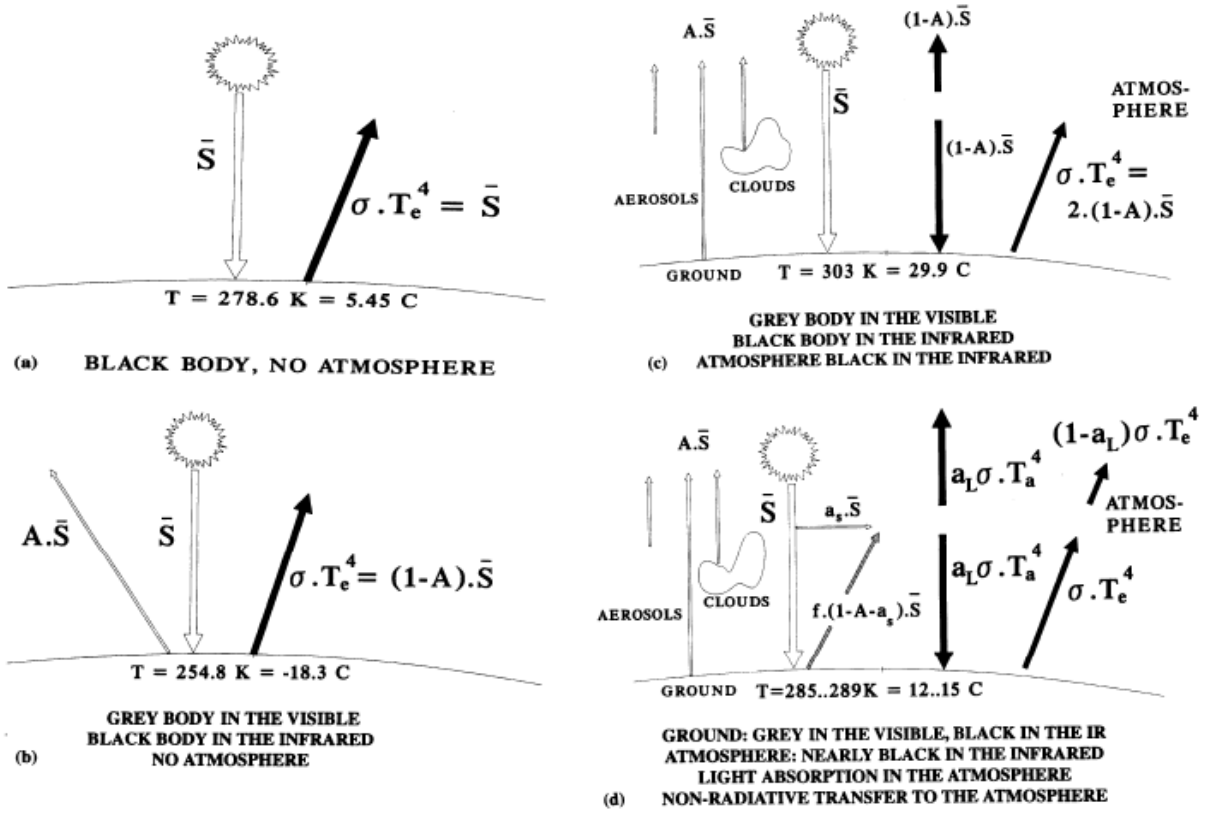

Fig. 1.1 Radiative fluxes of a body receiving solar radiation and emitting infrared radiation: (a) black body; (b) grey body in the visible and black body in the infrared; (c) but with a greenhouse atmosphere; (d) model of realistic atmosphere with light absorption in the visible, a non-radiative energy transfer from the ground to the atmosphere, and some transmission in the infrared. The meaning of the symbols which appear in the formulas are explained in the text. From Harrison, 1998.

The simplest case is the Earth as a black body without atmosphere (Fig. 1-1(a)). In this case the solar flux is totally absorbed by the planet and emitted as infrared radiation to space. Equating the solar radiation to the temperature of a black body given by the Stefan Boltzmann law (the energy emitted is proportional to the fourth power of the absolute temperature of the body), one obtains a mean temperature of Te=278.6K. But the Earth is not a black body in the visible and has a global mean albedo A=0.3, i.e. a fraction of 30% of the incoming radiation is reflected and thus only (1-A), i.e. 70% of the solar radiation can be emitted as infrared.

This is only possible if the surface temperature decreases with regard to the previous case as it is shown in Figure 1-1(b). This corresponds to a surface temperature of 254.8K which is cold. Thus, a change in the albedo drastically alters the surface temperature.

In this way, the atmosphere around the body has been taken into account and it contains some compounds which absorbs the infrared radiation emitted by the planet. By this absorption the atmosphere heats itself and emits radiation in all directions according to its temperature (Fig. 1-1(c)). As a first approximation, the atmosphere is a black body in the infrared. Radiation budget out of the atmosphere makes it clear that the average absorbed solar flux density has to be emitted by the atmosphere. But the atmosphere emits upwards and downwards and therefore the radiation received at the Earth's surface is twice the absorbed solar radiation. This amount has to be emitted by temperature radiation, which is only possible if the surface temperature is higher.

The atmosphere of the Earth is not completely absorbing and some other transfers not yet discussed take place as well. Some sunlight passing through the atmosphere is absorbed and transferred as heat to the atmosphere, obtained from the absorbance of short-wave (solar) radiation a_s (Fig. 1-1(d)). A fraction f of the absorbed energy is transported from the ground to the atmosphere by non-

radiative processes (latent and sensible heats). The other energy is radiated in the infrared from the surface of temperature T_e to the atmosphere which has an absorbance a_l for the infrared (long-wave) radiation and thus absorbs this fraction of the radiation from the Earth and transmits (1-a_l) upwards. Finally the atmosphere, having a temperature T_a, emits its grey body infrared radiation both upwards and downwards.
The balance of the fluxes for the surface is given by

$$\overline{S}(1-A-a_s)+a_l\sigma T_a^4=\sigma T_e^4+f\cdot\overline{S}(1-A-a_s) \tag{1.1}$$

where σ is the Stefan-Boltzmann constant. For the atmosphere the balance of the fluxes is

$$\sigma T_e^4+f\cdot\overline{S}(1-A-a_s)+a_s\overline{S}=(1-a_l)\sigma T_e^4+2a_l\sigma T_a^4 \tag{1.2}$$

Solving Eq. 1.1 and Eq. 1.2 for the atmospheric temperature T_a and rearranging gives

$$\overline{S}\frac{(2-f)(1-A-a_s)}{2-a_l}=\sigma T_e^4 \tag{1.3}$$

With a fraction f=30% of non-radiative transfer, a_s=1% of light absorption of the atmosphere and a_l=92-97% of infrared absorbance of the atmosphere, a global mean temperature between 285.0 and 288.4 K is obtained. The corresponding temperatures of the atmosphere are -21.5 and -19.6 °C [Harrison 1998]. Eq. 1.3 shows the effects of the different variables on the global mean surface temperature:

- Increasing the short-wave absorption (visible) a_s reduces the surface temperature but increases the atmospheric temperature.
- Increasing the long-wave absorption (infrared) a_l increases both the surface and atmospheric temperatures.
- Increasing the non-radiative heat transfer f reduces the surface temperature.

More infrared absorption by the atmosphere causes an increase in the temperature since the radiation is reradiated to the ground by the atmosphere: this is the *greenhouse effect*.
The main greenhouse gases (GHG) are: water vapour (H_2O), carbon dioxide (CO_2), ozone (O_3), methane (CH_2), nitrous oxide (N_2O), and halocarbons (CFC). These gases, except CFC, have both natural and anthropogenic sources and an increase by the anthropogenic sources induce an enhanced greenhouse effect. More reflectivity in the visible causes a decrease in temperature; this is the *whitehouse effect* [Schwartz, 1996]. This effect is mainly due to scattering by atmospheric particles (aerosols) and air molecules, clouds, and to the reflection by the Earth's surface itself.

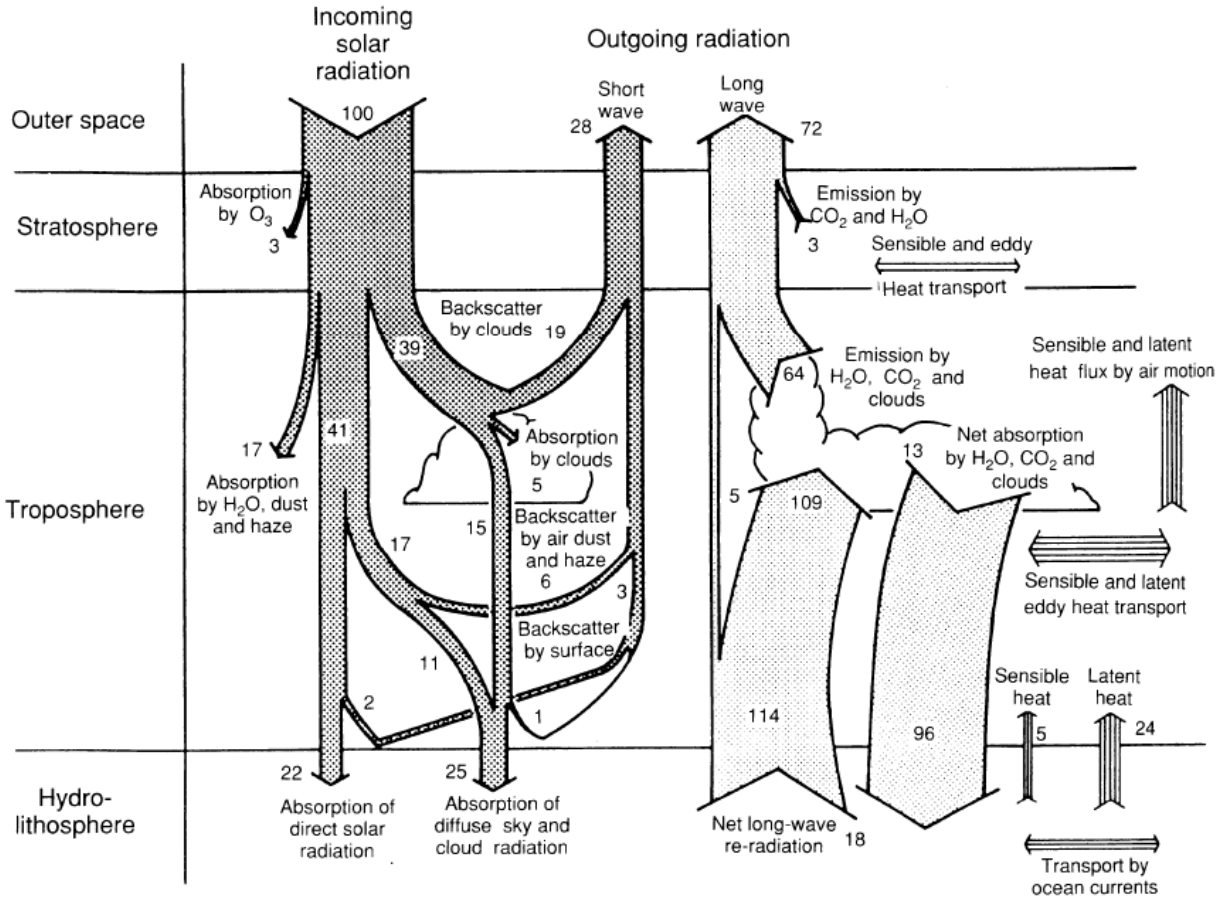

Figure 1.2. The annual mean global energy balance for the Earth-atmosphere system. Sensible heat is that one transferred to the atmosphere from the heated surface by turbulent eddies; latent heat is that one supplied to the atmosphere upon condensation of water vapour. The numbers are percentages of the energy of the incoming solar radiation. From Graedel, 1993.

Fig. 1.2 illustrates the efficiency of reflection, absorption and radiation with respect to the incoming solar radiation. An average of 28% of the incoming radiation is returned into space by backscattering from clouds (19%), air molecules and particles (6%), and by the surface (3%). Almost 25% is absorbed within the atmosphere, mostly by stratospheric ozone (3%), clouds (5%) and tropospheric water vapour (17%). The remaining 47% is absorbed by the Earth [Graedel 1993]. A little bit more than half of the solar radiation absorbed at the surface is transformed into latent heat (24%) and sensible heat (5%) whereas only 5% is lost by radiation, because the remainder is captured in the atmosphere by the greenhouse gases. But all these components have not the same impact on the energy balance and thus on the climate change. The quantity used to assess the importance of one compound to the climate system is the *radiative forcing.*

1.2. Radiative forcing

The definition given by the Intergovernmental Panel Climate Change [IPCC, 1990] of the radiative forcing of the climate system is: «The radiative forcing of the surface-troposphere system due to perturbation in or the introduction of an agent (say, a change in greenhouse gas concentrations) is the change in net irradiance (solar plus long-wave; in Wm^{-2}) at the tropopause after allowing for stratospheric temperatures to readjust to radiative equilibrium, but with surface and tropospheric temperatures and states held fixed at the unperturbed values.». Thus this definition is applied to perturbation in the radiation balance of the surface-troposphere system without any feedbacks. In

order to re-establish equilibrium, a temperature change ΔT_e results, which is related to the radiative forcing ΔF_{net} by the climate sensitivity factor λ_0 [K $(Wm^{-2})^{-1}$]. The radiative forcing is not the climate response. The former is a change imposed on the planetary energy balance whereas the latter is the meteorological results of those *forcings*, such as global temperature change, rainfall changes, or sea level changes.

Fig. 1.3 shows the global mean radiative forcing (RF) of the climate system [IPCC, 2007]. The height of the rectangular bar denotes a central or best estimate value. The vertical line about the rectangular bar delimiters indicates an estimate of the uncertainty range. It is also shown the level of scientific understanding (LOSU), which represents subjective judgement about the reliability of the forcing estimate, involving factors such as the assumptions necessary to evaluate the forcing, the degree of knowledge of the physical and chemical mechanisms determining the forcing, and the uncertainties surrounding the quantitative estimate of the forcing. The typical geographical extent (spatial scale) of the forcing is also showed.

A positive radiative forcing, such as that produced by increasing concentration of greenhouse gases, tends to warm the surface whereas a negative radiative forcing, which can arise from an increase in some types of aerosols tends to cool the surface (whitehouse effect).

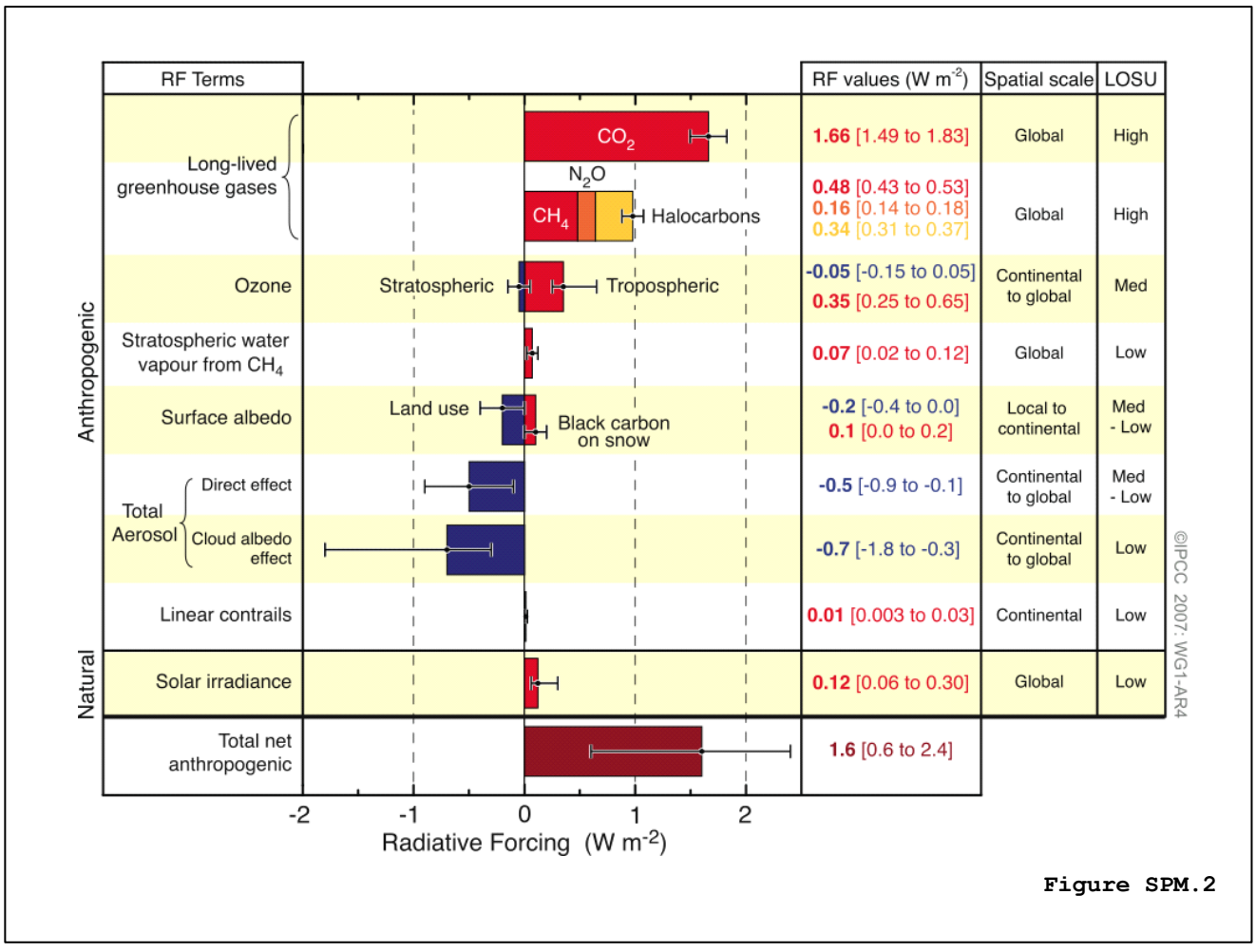

Figure 1.3. Global average radiative forcing (RF) estimates and ranges in 2005 for anthropogenic carbon dioxide (CO_2), methane (CH_4), nitrous oxide (N_2O) and other important agents and mechanisms, together with the typical geographical extent (spatial scale) of the forcing and the assessed level of scientific understanding (LOSU). The net anthropogenic radiative forcing and its range are also shown. These require summing asymmetric uncertainty estimates from the component terms, and cannot be obtained by simple addition. Additional forcing factors not included here are considered to have a very low LOSU. Volcanic aerosols contribute an additional natural forcing but are not included in this figure due to their episodic nature. The range for linear contrails does not include other possible effects of aviation on cloudiness.

The distribution of water vapour is strongly variable in space and in time. This distribution is mainly driven by the air motions and the changes of physical states of the water, but is only slightly affected by human activities, e.g. deforestation on a large scale [Brasseur, 1999]. This assumption is disputed and the sign of the greenhouse effect could be inverted if the atmospheric motions of the water vapour are taken into account [de Félice, 2001].
The radiative forcing due to increases of well-mixed greenhouse gases is estimated to be +2.43 Wm^{-2}: +1.46 Wm^{-2} from the CO_2, +0.48 Wm^{-2} from the CH_4, +0.34 Wm^{-2} from the halocarbons, +0.15 Wm^{-2} from the N_2O. The depletion of the stratospheric ozone is estimated to have caused a negative radiative forcing of -0.15 Wm^{-2}, whereas the radiative forcing of the tropospheric one is +0.35 Wm^{-2}. Ozone forcing varies considerably by region and responds much more quickly to changes in emission than the long-lived greenhouse gases (CO_2, CH_4, N_2O and CFCs).
Concerning the well-mixed greenhouse gases, the infrared absorption and radiative transfer are well quantified, while concerning the short-lived greenhouse gases, their infrared absorption is reasonably well quantified, radiative aspect is well posed, but they are highly variable in space and time [Seinfeld and Pandis, 1998].

Aerosol particles affect the radiative balance of the Earth both directly, by scattering and absorbing solar and terrestrial radiation, and indirectly through their action as cloud condensation nuclei (CCN) with subsequent effects on the microphysical and optical properties of clouds. Concerning the direct radiative forcing, the aerosols are divided into four categories: 1) sulphate (-0.4 Wm^{-2}), 2) fossil fuel burning (black carbon, +0.2 Wm^{-2} and organic carbon, -0.1 Wm^{-2}), 3) biomass burning (-0.2 Wm^{-2}) and 4) mineral dust. The sign of the effects due to mineral dust is uncertain. Aerosol radiative forcing also varies considerably by region and responds quickly to changes in emissions. The determination of the forcing is relatively a well-posed problem, but is strongly dependent on empirical values for several key aerosol properties and is also dependent on models for geographical and temporal variations of forcing.
The indirect aerosol radiative forcing is divided into the first indirect effect (increase in droplet number associated with increases in aerosols) and the second indirect effect (decrease in precipitation efficiency with increases in aerosols). The former has strong observational support [Charlson, 1995] whereas the latter has only limited support [IPCC, 2001]. The indirect radiative forcing depends on aerosol number distribution, but the inadequacy of descriptions of aerosols and clouds seriously restricts abilities to predict this forcing. Furthermore, the radiative forcing associated with the stratospheric aerosols from volcanic actions is highly variable. Generally, volcanic eruptions lead to a negative radiative forcing, which lasts a few years after the eruptions.
Changes in the physical character of the land surface can affect land-atmosphere exchanges of radiation, momentum, heat and water. The radiative forcing due to change in surface albedo leads to a negative radiative forcing. The radiative forcing due to a change in solar irradiance, which is a natural forcing, is estimated to be about +0.3 Wm^{-2}.
Unfortunately, the resulting radiative forcing cannot be a simple sum of the positive and negative bars due to the strong regional signatures of certain radiative forcing agents, such as aerosols.
Nevertheless the simulations indicate that the estimated net effect of these perturbations is to have warmed the global climate since 1750 [IPCC, 2001]. But the uncertainties, in particular on the aerosols, are unacceptably large and present serious limitations to modelling of climate [Charlson, 1995]. This uncertainty is as high as the absolute level of the additional greenhouse forcing. The radiative forcing attributable to aerosol changes is still available only as semiquantitative estimate. Part of the reason for this is the greater radiative complexity of aerosols, their large variabilities in space and in time, and their relatively short atmospheric lifetime. However, in addition to these modelling related problems, the persistent uncertainty in aerosol forcing is due to the continued absence of monitoring system that is capable of measuring and monitoring changes in aerosol amounts and their radiative properties with sufficient accuracy [Charlson, 1995].

1.3. Aerosol direct effects on climate

An aerosol is defined as: «a suspension of fine solid or liquid particles in a gas» [Seinfeld and Pandis, 1998]. Their natural sources are soil and rock debris (terrestrial dust), volcanic action, sea spray, biomass burning, and reaction between natural gaseous emissions. Emissions of particulate matter attributable to the human activities arise primarily from four source categories: fuel combustion, industrial processes, non-fugitive sources (roadway dust, wind erosion of cropland, construction, etc.) and transportation sources (automobiles, etc.) [Seinfeld and Pandis, 1998]. Aerosols range in size from a few nanometers to tens of micrometers as it is illustrated in Figure 1.4. This figure shows the surface area distribution of an idealized atmospheric aerosol. Fines aerosols have a diameter smaller than 2.5 μm whereas coarse particles have a diameter greater than 2.5 μm. The coarse particles are formed by mechanical processes and consist of man-made and natural dust particles. The fine particles are divided into two modes: the transient nuclei or Aitken nuclei range (from about 0.005 to 0.1 μm) and the accumulation range (from 0.1 to 2.5 μm). The former are formed from condensation of hot vapours during combustion processes and from nucleation of atmospheric species to form fresh particles. They are lost principally by coagulation with larger particles. The latter are formed from the coagulation of particles in the nuclei mode and from condensation of vapours into existing aerosols, causing them to growth into this size range. The removal mechanisms are least efficient causing particles to accumulate there.

Greenhouse gases such as CO_2, CH_4, N_2O and CFCs are virtually uniform globally distributed in the troposphere due to their high atmospheric lifetimes (from decades to centuries), whereas aerosol concentrations are highly variable in space and time as water vapour and ozone concentrations.

With lifetimes of about a week, sulfate aerosols are most abundant close to their sources in the industrialized areas of the Northern Hemisphere. Biomass aerosols are emitted predominantly during dry season in tropical areas. Mineral dust appears down wind of large arid regions. Moreover, greenhouse gas forcing operates day and night; aerosol forcing operates only during day.

The aerosols influence directly the radiative budget by the scattering and the absorption of the solar radiation. This effect depends on the amount of light scattered back to space. This amount is the fraction of light that is scattered into the upwards hemisphere relative to the horizon.

The upscatter fraction *b* depends on the size distribution and optical properties of the particles, and on the solar angle.

The direct radiative forcing of an aerosol layer, with the assumptions of the Sun at its zenith and cloud free atmosphere, is given by [Finlayson-Pitts, 2000]:

$$\Delta F_R = -\left(\frac{1}{4}F_T\right)(1-A_c)T^2\left[(1-R_s)2\beta\tau_{scat} - 4R_s\tau_{abs}\right] \tag{1.4}$$

where ΔF_R is the net global average short-wave radiative forcing due to aerosols, F_T is the incoming solar radiation, A_c is the fraction covered by clouds, T is the fraction of light transmitted above the aerosol layer, R_s is the surface albedo, β is the upscatter fraction, τ_{scat} is the effective aerosol optical depth due to scattering and τ_{abs} is the optical depth due to aerosol absorption.

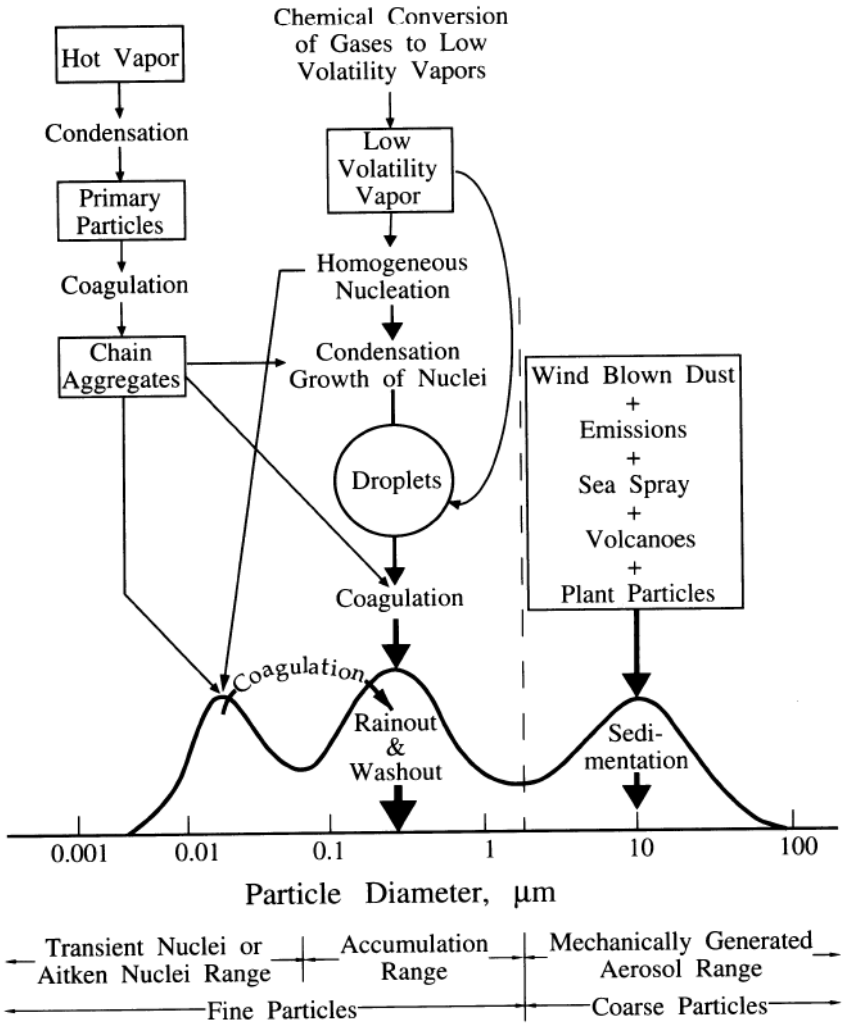

Figure 1.4. Idealized schematic of the distribution of particle surface area of an atmospheric aerosol. Principal modes, sources, and particles formation and removal mechanism are indicated. From Seinfeld and Pandis, 1998.

The radiative forcing depends on the optical depth and the upscatter fraction of the aerosols.
Those parameters depend on the chemical composition and size distribution of the aerosols.
Thus the key parameters of the radiative forcing are the chemical composition through its refractive index, the size distribution of the aerosols and number density. And the largest uncertainties of this radiative forcing are associated with the radiative properties of the aerosols and the influence of the relative humidity.
As it was mentioned in the previous section, those semiquantitative estimates can seldom be compared to atmospheric data and thus limit the validation of the models. So the 3D global database of the aerosol properties and effects needs to be enhanced drastically [Heintzenberg, 2001].

1.4. Aerosol measurements

Aerosol measurements can be divided into two types: *in situ* and remote sensing. The latter can also be divided in active and passive remote sensing. The former uses its own source of radiation (radar, lidar, etc) while the latter is dependent on an external source (spectral radiometers, sunphotometers, etc).
The *in situ* measurements have the advantage that optical, chemical and microphysical parameters can be determined, but do not have any vertical resolution, except the airborne platforms.

The data of *in situ* measurements of size distribution and chemical composition of aerosols, although reliable, cannot, however, be considered representative for large spatial and temporal scales. Therefore new complex results of ground, aircraft, balloon, and satellite observations should form the basis for climatological aerosol models [Kondratyev, 1999].

1.5. Conclusion

The greenhouse effect allows the life on the planet in keeping the surface temperature around +15° C. This effect is natural and do not alter the climate, whereas the enhanced greenhouse effect whose origin is anthropogenic, is certainly the prime environmental problem of this new millennium. The climatic response to this effect is a global warming of the surface.
Up to now the aerosol contribution to climatic change was generally not taken into account. This gap, both in the modelling and monitoring, induces large uncertainties. Therefore new complex results of synergy of ground, aircraft, balloon, and satellite observations should form the basis for climatological aerosol models.

1.6. References

Brasseur G. P., Orlando J. J., and Tyndall G. S., **Atmospheric Chemistry and Global Change**, Oxford University Press, (1999).

Graedel T. E., and Crutzen P.J., **Atmospheric Change: an Earth system perspective**, New-York, W. H. Freeman and Compagny, (1993).

Harrison R. M. and van Grieken R. E., **Atmospheric particles**, New-York, John Wiley & Sons. Ltd, (1998).

Heintzenberg J., **Aerosol influence on the radiation budget: Where do we stand?** Palaiseau, Editions de l'Ecole polytechnique, (2001).

Houghton, J., **Global Warming: the complete briefing**, Cambridge University Press, (1997).

IPCC, Intergovernmental Panel Climate Change, Cambridge University Press, (1990).

IPCC, Intergovernmental Panel Climate Change, Cambridge University Press, (2007).

Jennings S. G., **Aerosol Effects on Climate**, the University of Arizona Press (1993).

Kondratyev K. Y., **Climatic effects of aerosols and clouds**, Berlin, Springer-Verlag, (1999).

Lomborg, B., **The sceptical environmentalis**t, Cambridge University, (2001).

Ramanathan V., Crutzen P.J., Kiehl J.T., Rosenfeld D, "**Aerosols, Climate, and the Hydrological Cycle**." Science **294**: 2119-2124, (2001).

Santer, B., and al., **Towards the detection and attribution of an anthropogenic effect on Climate**, Climate Dynamics **12**: 77-100, (1995).

Schwartz S. E., **The whitehouse effect: Shortwave radiative forcing of climate by anthropogenic aerosols**, Journal of Aerosol Science **27**, pp. 359-382, (1996).

Seinfeld J. H. and S. N. Pandis, **Atmospheric Chemistry and Physics**, Wiley Interscience, (1998).

Shine, K. P., de Forster, P.M., **The effect of human activity on radiative forcing of climate change: a review of recent developments**, Global and Planetary Change **20**: 205-225, (1999).

Introduction

Different kinds of atmospheric monitoring techniques have been developed in the past years. With respect to the sampling procedure, such techniques can be distinguished in *in situ* and *remote sensing*. In the former ones, the pollutants and/or the aerosols are measured directly and in many cases non–destructively. Otherwise, by the *remote sensing* technique it is possible to measure samples at a certain distance. The advantage is the contactless measurement, which provides three–dimensional concentration or integrated profile of pollutions and/or aerosols.

The lidar (**li**ght **d**etection **a**nd **r**anging) technique is an active remote sensing technique because it uses an artificial light source (laser) for the retrieval of atmospheric parameters. This is different from passive methods, which use light emission from natural light sources (sun, moon) or thermal emission. Probing the atmosphere with a laser is similar to using a radar, with the difference that the lidar uses electromagnetic radiation (light) from the optical domain instead of radio waves. The laser beam is emitted into the atmosphere and the portion scattered back is subsequently detected. Since the light travels at known velocity, the range of the scattering volume producing the signal can be uniquely determined from the time interval since the transmission of the pulse. The magnitude of this signal is determined by the backscattering properties of the atmosphere and by the two-way atmospheric attenuation. Those properties depend upon the wavelength of the laser energy used and the number, size distribution, shape and refractive index properties of the molecules or particles intercepted by the incident laser energy [Hinkley, 1976; Measures, 1992].

More information is available in the received signal because of additional parameters. For example, the depolarization ratio is a good indicator of the shape of the aerosols and the Angstrom exponent [Angstrom, 1964], but do not provide reliable information on the aerosol size distribution. With multiple-wavelength lidar configurations, it is possible to determine independent extinction and backscatter coefficients and thus to retrieve aerosol microphysical parameters.

Therefore, lidar is a well-established technique for measuring trace constituents, aerosols, atmospheric structure and dynamics, clouds, and also meteorological parameters, such as temperature, humidity and wind velocity. Moreover, it is able to provide high-quality data with high vertical and temporal resolution.

This chapter deals with the basic principle of the lidar technique. In order to fully understand the lidar technique, a short overview of the involved physical processes is presented. As the transmitted laser energy passes through the atmosphere, the gas molecules and aerosols encountered cause scattering (Rayleigh, Mie and Raman) and absorption. These interactions can be divided into two classes, the elastic interaction for which the wavelength of the scattered light is the same as that one of the incident beam and the inelastic interaction, for which the scattered radiation has a wavelength different from that one of the incident radiation.

2.1. Atmospheric interactions

When a beam of light impinges on a molecule or particle, electric charges are excited into oscillatory motion. The excited electric charges re-radiate energy in all directions (scattering) and may convert a part of the incident radiation into internal energy (absorption). Light scattering mechanisms can be divided into three categories:

- Elastic scattering, where the wavelength of the scattered light is the same as that of the incident beam);
- Quasi-elastic scattering, where the wavelength shift is due to Doppler effects and diffusion broadening;
- Inelastic scattering, where the emitted radiation has a wavelength different from that one of the incident radiation;

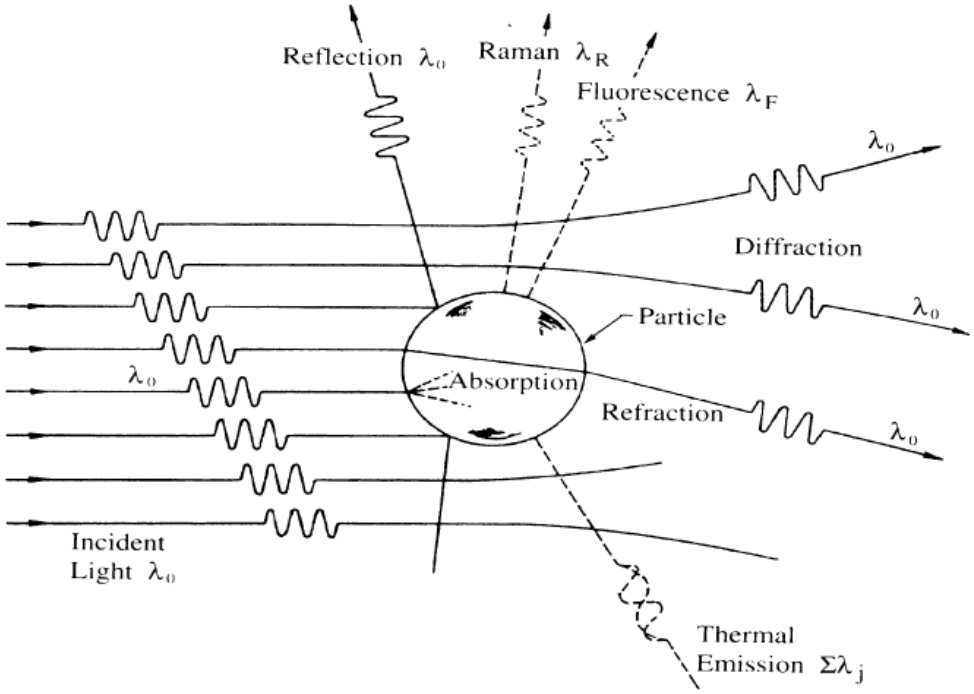

Figure 2.1 Mechanisms of interaction between incident radiation and a particle. From Seinfeld and Pandis, 1998.

Figure 2.1 illustrates the various processes occurring when radiation of wavelength λ_0 interacts with a diffuser (molecule or particle). Inelastic scattering processes include Raman and fluorescence. The key parameters governing the scattering of light by a diffuser are:

- The wavelength λ_0 of the incident radiation.
- The size of the diffuser, usually expressed as a dimensionless size parameter χ which is the ratio between the circumference of the spherical diffuser and the wavelength of the light:

$$\chi = \frac{2\pi r}{\lambda} \tag{2.1}$$

- The complex refractive index, whose the real part, n, and the imaginary part, k, are functions of the wavelength. The real and imaginary parts represent the not-absorbing and absorbing components, respectively:

$$m = n + ik \tag{2.2}$$

Mie theory provides a basis of a computational procedure to calculate the scattering and the absorption of light by any target as a function of the wavelength [Bohren, 1983]. There are, in addition, approximate expressions, valid in certain limiting cases, which provide insight into the physics of the problem. Based on the value of χ, light scattering can be divided into three domains

- $\chi << 1$, Rayleigh scattering
- $\chi \sim 1$, Mie scattering
- $\chi >> 1$, Geometric scattering.

The description of the laser beam interaction with atmospheric constituents (i.e. molecules, particles, clouds) is based on the fundamental theory of electromagnetic wave propagation in various media. The atmosphere contains constituents with a wide range of diameters d, extending from atoms and molecules (Angstrom range, d ~ 10^{-3} - 10^{-4} μm) to aerosols (d ~ 10^{-3} - 5 μm), cloud water droplets and ice crystals (d ~ 1 - 15 μm and even larger).
The mixture of these different components results in a series of complex atmospheric interactions that take place with a laser beam. The intensity of the light scattered by these processes is proportional to the initial intensity I_o, the number density *n* of the active diffusers and their differential angular cross-section σ.
If a monochromatic and coherent light (i.e. a laser beam) is sent to the atmosphere, different processes may take place with different probabilities determined by their corresponding cross-sections, σ = f(λ, process, atmospheric diffuser). The interaction may lead to elastic (Rayleigh and Mie) and inelastic (Raman) scattering, absorption, reflection, and/or diffraction. The interactions may be "non-selective", like Rayleigh, Mie or Raman scattering, and more or less important depending on the atmospheric composition (e.g. aerosol loading in the case of Mie scattering). Absorption, for example, is a selective process, and is dependent on the absorption cross section at the laser wavelength. The resonant processes (Rayleigh or Raman) are also selective, meaning that the laser wavelength radiation matches specific electronic transitions of the molecule.
The next three sections present the theory of the elastic scattering by molecules (Rayleigh) and particles (Mie), and of the inelastic scattering by molecules (Raman), respectively.

2.2. Elastic (Rayleigh) scattering

Rayleigh scattering refers to the light elastically scattered from the molecules and can be extended to scattering from particles up to about one tenth of the light wavelength. In the Rayleigh scattering regime, a closed form solution of the scattering problem is possible.
The electromagnetic incident wave induces a dipolar moment (P) within the molecular system:

$$\overline{P} = \alpha \cdot \overline{E} \tag{2.3}$$

where E is the intensity of the electric field of the incident electromagnetic wave and α is the polarisability tensor of the molecule. For the atmospheric diffusers, such as nitrogen and oxygen molecules, α can be considered independent from E and this explains the re-emission of the radiation at the same frequency of the incident electromagnetic wave. For one incoming photon, one photon is re-emitted with the same energy.
The Rayleigh backscatter is proportional to the diffusers' number density and to the Rayleigh differential cross section. The differential (angular) Rayleigh cross-section, $d\sigma_m/d\Omega$ [cm^2 $molecule^{-1}sr^{-1}$], may be expressed as given by Bohren (1993) by the following equation:

$$\frac{d\sigma_m(\phi,\theta,\lambda)}{d\Omega} = \frac{9\pi^2\left(n_{air}^2-1\right)^2}{\lambda^4 N_{air}^2\left(n_{air}^2+2\right)^2}\left(\frac{6+3\rho}{6-7\rho}\right)\left\{\cos^2\phi\ \ \cos^2\theta+\sin^2\phi\right\} \tag{2.4}$$

where λ [cm] is the wavelength, N_{air} [molecules cm^{-3}] is the air molecule number density, n_{air} is the air complex refraction index, ρ is the depolarization ratio (see paragraph 2.8), ϕ [rad] is the polarization angle, and θ [rad] is the scattering angle (see Fig. 2.2).

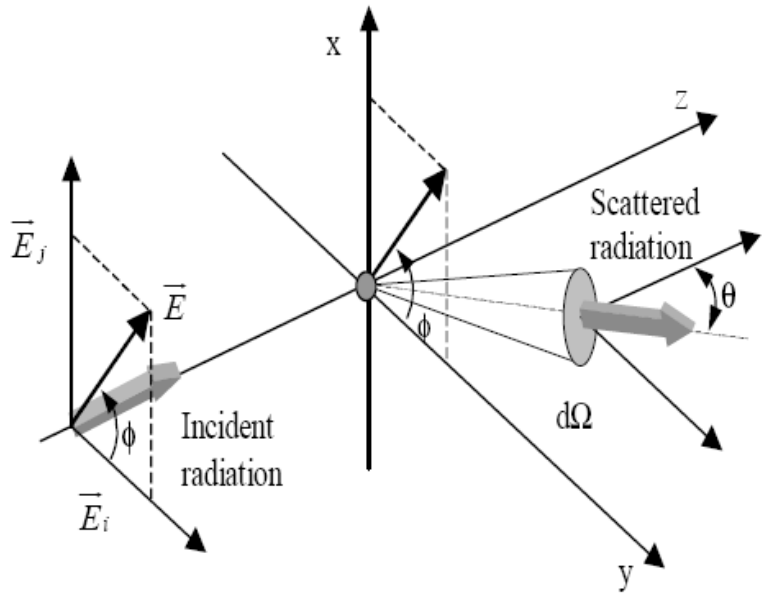

Figure 2.2 Schematic of the incident and scattered light waves. From Lazzarotto, 2000.

The Rayleigh scattering phase function is isotropic (i.e. ratio of one direction/all directions scatter powers) and is 3/8π leading to:

$$\sigma_m(\lambda) = \frac{8\pi}{3} \cdot {}^{\pi}\sigma_m(\lambda) \tag{2.5}$$

where ${}^{\pi}\sigma_m$ is the backscatter (at 180°) molecular (correspondent to the sum of N_2 and O_2) cross - sections:

$${}^{\pi}\sigma_m(\lambda) = \frac{d\sigma_m(\phi,\pi,\lambda)}{d\Omega} \tag{2.6}$$

The scattered light intensity pattern is symmetric in the forward and backward directions, and totally polarized at 90° [Bodhaine, 1999].
For this work, a simpler but realistic semi-empirical formula for the estimation of the differential backscattering cross section is:

$${}^{\pi}\sigma_m(\lambda) = 5.45 \cdot 10^{-32}\left(\frac{550}{\lambda}\right)^{4.09} \tag{2.7}$$

with $d\sigma/d\Omega$ expressed in m^2 $molec^{-1}$ and λ in nm. The backscatter coefficient, β_m, is obtained by multiplying Eq. 2.7 with the air number density n_{air} *(Z)*. Then by multiplication with the inverse of Rayleigh phase function, the molecular extinction coefficient α_m *(Z)* is obtained

$$\alpha_m(Z) = \frac{8\pi}{3}\beta_m(Z) = \frac{8\pi}{3} n_{air}(Z)^{\pi}\sigma_m(\lambda) \tag{2.8}$$

with α_m expressed in m^{-1} and β_m in $m^{-1}sr^{-1}$. The air number density $n_{air}(Z)$ is determined from the air pressure and temperature profiles as measured by radiosondes or estimated using atmospheric models such as the US-Standard Atmosphere 1976 model (see paragraph 2.2.1).
The formula above indicates a Rayleigh cross-section that follows a λ^{-4} wavelength dependency, and for this reason, the shorter the wavelength, the more scattered the corresponding radiations. The scattering cross-section is relatively small, on the order of ~ 10^{-28} cm^2 $molec^{-1}$, but the air concentration number i.e. ~ 10^{19} molec cm^{-3} partially compensates for the inefficiency of this process.

2.2.1. US-Standard Atmosphere 1976

Various «standard atmospheres» have been established as reference for general scientific purposes and for designing and testing aerospace vehicles. Each of these references incorporated the best data available from the real atmosphere at the time. The real atmosphere at a given time and location necessarily differs from an annual model constructed for a single latitude band. Weather, on both local and synoptic scales, produces large fluctuations in the properties of the troposphere, and the fluctuations frequently extend into the stratosphere. In addition, there are systematic variations due to latitude and season, and solar factors become important at high altitudes [Mc Cartney, 1976]. The US-Standard-Atmosphere 1976 was used in the present work. It is an idealized as a steady-state representation of the earth's atmosphere from the surface up to 1000 km; it is assumed to exist in a period of moderate solar activity. The atmosphere is assumed to be homogeneously mixed with a relative-volume composition leading to a mean molecular weight.
The standard atmosphere is divided into five layers: from 0 to the altitude of the tropopause (12 km), from this altitude to 20 km, from 20 to 35 km and from 35 to 50 km with gradients of temperature of -0.65 K/100 m, +0.0 K/100 m, +0.1 K/100 m and +0.24 K/100 m, respectively.
The temperature and the pressure at a given altitude are calculated by the following equations:

$$T(r) = T(r_0)\left(\frac{1-\frac{dT}{dr}}{T(r_0)(r-r_0)}\right)$$

$$P(r) = P(r_0)\left(\frac{1-\frac{dT}{dr}}{T(r_0)(r-r_0)}\right)^{\frac{g}{R\frac{dT}{dr}}} \tag{2.9}$$

where r [m] is the altitude in a layer, r_0 [m] is the altitude of the bottom of the layer, g [$m\ s^{-2}$] is the acceleration due to gravity and R is the gas constant.

2.3. Elastic (Mie) scattering

In the presence of particles with a size comparable to the incident wavelength, the Mie scattering becomes predominant. Its efficiency is generally much bigger than the Rayleigh's one.

The angular characteristics of the Mie scattering for all particle sizes and wavelengths are expressed by two intensity distribution functions. The light scattered by a particle at observation angle θ may be treated as consisting of two components having intensities $I_c(\theta)$ and $I_p(\theta)$, perpendicular and parallel to the plane of observation, respectively. The components are proportional to intensity distribution function i_c and i_p, respectively:

$$i_c(\chi, m, \theta) = \left| \sum_{n=1}^{\infty} \frac{2n+1}{n(n+1)} \left(a_n \pi_n + b_n \tau_n \right) \right|^2 \tag{2.10}$$

$$i_p(\chi, m, \theta) = \left| \sum_{n=1}^{\infty} \frac{2n+1}{n(n+1)} \left(a_n \tau_n + b_n \pi_n \right) \right|^2 \tag{2.11}$$

where n is a positive integer. The values of a_n and b_n are the Ricatti-Bessel functions, the arguments of which are the size parameter χ and the complex refractive index, m. The functions π_n and τ_n depend only on the angle θ and involve the first and second derivatives of the Legendre polynomials having order n and argument $\cos(\theta)$.

The intensity of the light scattered by the particles is:

$$I(\theta, \phi) = E_\phi \frac{\lambda^2}{4\pi^2} \left(i_c \sin^2 \phi + i_p \cos^2 \phi \right) \tag{2.12}$$

where E_ϕ is the irradiance of the incident light. The differential cross-section $d\sigma_p/d\Omega$ for particle is given by:

$$\frac{d\sigma_p(\theta, \phi)}{d\Omega} = \frac{I(\theta, \phi)}{E_\phi} = \frac{\lambda^2}{4\pi^2} \left(i_c \sin^2 \phi + i_p \cos^2 \phi \right) \tag{2.13}$$

Figure 2.3 shows the scattering phase function for several diameters D_p at $\lambda = 0.550$ μm. When the diameter is small compared with λ, the phase function is symmetric in the forward and backward directions (see also Fig. 2.4).

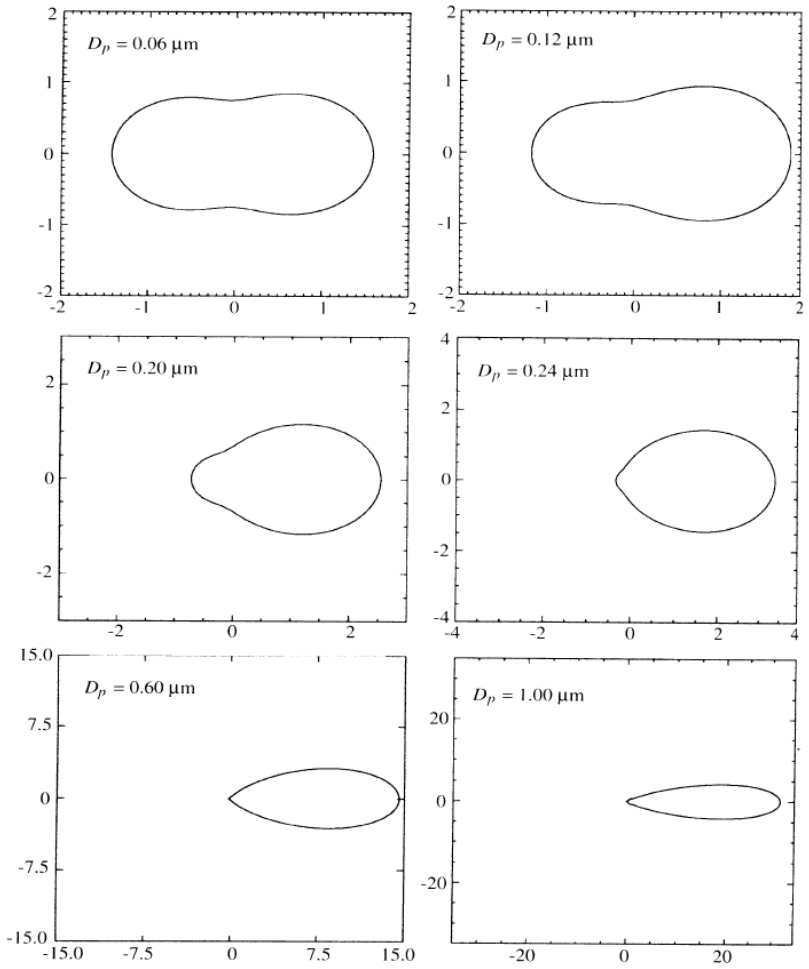

Figure 2.3 Mie scattering phase function at λ = 550 nm versus diameter of the particle. The incident light enters from the left. From Seinfeld and Pandis, 1998.

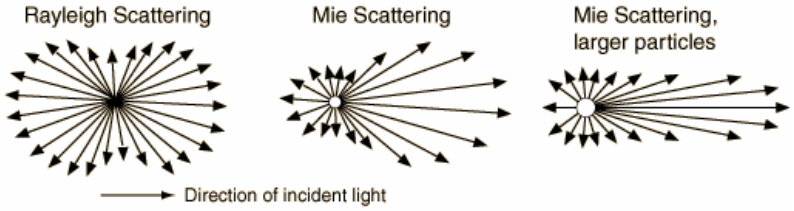

Figure 2.4 Angular distribution of the scattered intensity. When the diameter of the particle increases, there is a "peak" of the scattered intensity in the forward direction.

The directional asymmetry becomes more and more pronounced as the particles size increases. The asymmetry parameter g, is defined as

$$g = \frac{\int_0^{\pi} \frac{d\sigma_p(\theta,\phi)}{d\varphi}\cos(\theta)\sin(\theta)d\theta}{\int_0^{\pi} \frac{d\sigma_p(\theta,\phi)}{d\varphi}\sin(\theta)d\theta} \tag{2.14}$$

For isotropic or symmetric scattering (e.g. Rayleigh scattering) the asymmetry parameter is zero, for a purely forward scattering particle it is 1. The asymmetry parameter of the cloudless atmosphere ranges from 0.1 (very clean) to 0.75 (polluted); for a cloudy atmosphere the values are between 0.8 and 0.9 [Harrison, 1998].
The total scattering cross section σ_p [cm^2 $molec^{-1}$] may be calculated by integrating Eq.2.13 over 4π sr

$$\sigma_p = \int_0^{4\pi} \frac{\sigma_p(\theta,\phi)}{d\Omega} d\omega = 2\pi \int_0^{\pi} \frac{\sigma_p(\theta,\phi)}{d\phi} \sin(\theta) d\theta \tag{2.15}$$

The total scattering cross section values cover a wide range greater than the corresponding range of geometric cross section. The ratio of the scattering to geometric cross section is defined as the efficiency factors as follows:

$$Q_{sc} = \frac{\sigma_p}{\pi r^2} = \frac{2}{r^2} \int_0^{\pi} \frac{\sigma_p(\theta,\phi)}{d\phi} d\theta$$

$$Q_{\pi} = \frac{\frac{d\sigma_p(\theta,\phi)}{d\phi}(\theta = \pi)}{\pi r^2} \tag{2.16}$$

where r is the radius of the particle and the complex part of the refractive index is not taken into account. The link between the extinction α and the backscatter β coefficients and the efficiency factors Q_{sc} and Q_{π} is given by:

$$\alpha_p = \pi \int_0^{\infty} r^2 Q_{ext} n(r) dr$$

$$\beta_p = \pi \int_0^{\infty} r^2 Q_{\pi} n(r) dr \tag{2.17}$$

where n(r) is the particle size distribution and in the calculation of Q_{ext} the complex part of the refractive index is taken into account (i.e. $Q_{ext} = Q_{sc} + Q_{ab}$, where Q_{ab} is the absorption efficiency factor).
It is useful in some cases to represent the wavelength dependence by the Angstrom exponent (*a*). It is calculated from measured values of the extinction coefficient as a function of wavelength by

$$a = -\frac{d\log(\alpha)}{d\log(\lambda)} \cong -\frac{\log\left(\frac{\alpha(\lambda_1)}{\alpha(\lambda_2)}\right)}{\log\left(\frac{\lambda_1}{\lambda_2}\right)} \tag{2.18}$$

In the Rayleigh regime, the extinction coefficient varies with wavelength to a power of -4, whereas in the large-particle regime, this exponent ranges between 1 and 0 [Mc Cartney 1976; Seinfeld and Pandis 1998].

2.4. Inelastic (Raman) scattering

When the Raman scattering is involved the laser radiation is inelastically scattered from molecules and is observed with a frequency shift characteristic of the molecule (and with a known backscattering cross-section), In Fig. 2.5 two types of Raman scattering that occurred simultaneously are shown: the Stokes process which shifts the wavelength to upper ones, and the anti Stokes one which shifts the wavelengths to lower values. In this scheme one photon is re-emitted with less (Stokes) or more (anti Stokes) energy than the incoming one. This scattering results from the interaction between the exciting radiation and the electric dipole moment of the molecule. It induces a change in the rotational or/and vibrational states of the molecule.

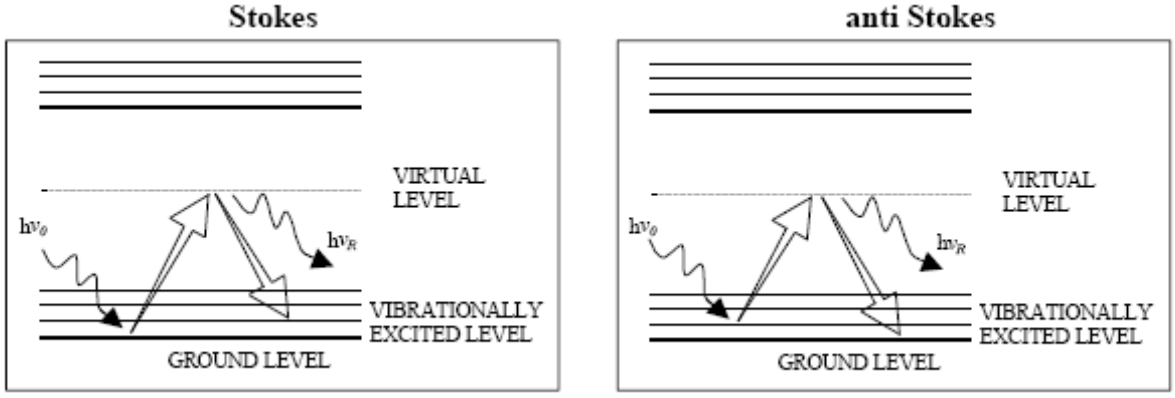

Figure 2.5. Raman interaction. From Lazzarotto, 2000.

The interaction life time is very small, and smaller than 10^{-14} s.

The study of the Raman spectrum allows the simultaneous measurement of a wide variety of components and the absolute measurement of their mixing ratio. This process has a very low efficiency (cross-sections about 10^{-32} - 10^{-28} cm^2 molecule^{-1}), and can be improved by working in the UV, at shorter wavelengths, because the Raman differential cross-section is proportional to λ^{-4}.

The expression for the total vibrational Raman backscattering cross-section of a Stokes shifted vibrational-rotational Raman band υ_j is given by [Inaba and Kobayashi, 1969]:

$$\frac{d\sigma}{d\Omega}(\nu_0) = \frac{(2\pi)^4}{45} \frac{(\nu_0 - \nu_j)^4 b_j^2}{1 - \exp\left(-\frac{hc\nu_j}{kT}\right)} g_j \left(45 a_j^2 + 7\gamma_j^2\right) \tag{2.19}$$

where υ_j [cm^{-1}] is the frequency of the jth vibrational mode of the molecule, b_j is the zero amplitude of this jth vibrational mode, T [K] is the temperature, g_j is the degeneracy of the jth vibrational mode, a_j and γ_j are the isotropic and anisotropic parts of the polarizability tensor derived with respect to the normal coordinates and k is the Boltzmann constant.

At atmospheric temperature most molecules are in their vibrational ground state $\upsilon = 0$ (and also the electronic one). The Stokes bands will then be much more important than the anti-Stokes ones. In addition each vibrational line gives rise to a closely spaced band of lines corresponding to different

transitions in the rotational quantum number. Thus, the laser excitation of the O_2, N_2 and H_2O atmospheric molecules due to the laser beam will give essentially the Stokes type transition υ 0–>1. For a given excitation wavelength the Raman scattering will provide a shifted spectra characteristic of the excited molecule. The wavenumber k [cm^{-1}] is defined by:

$$\lambda = \frac{c}{\nu} = \frac{1}{k} \tag{2.20}$$

and the Raman shift Δk is given by

$$\Delta k = k_L - k_R \tag{2.21}$$

where k_L [cm^{-1}] is the laser pump wavenumber and k_R [cm^{-1}] is the Raman shifted wavenumber. The Raman shifts from the exciting wavelength are the following: 2331 cm^{-1} for N_2 and 3652 cm^{-1} for H_2O. The related Raman shifted wavelength λ_R [cm] is

$$\lambda_R = \frac{\lambda_L}{1 - \Delta k \cdot \lambda_L} \tag{2.22}$$

where Δk [cm^{-1}] is the Raman shift, λ_L [cm] is the laser pump wavelength.

2.5. Molecular absorption

In both Rayleigh and Mie cases, neither the linewidth nor the wavelengths are critical. It is important, obviously, to avoid coincidences with the absorption wavelengths of the atmosphere components.

The molecular absorption coefficient $\alpha_a(\lambda, r)$ [cm^{-1}] for a group of molecules is given by

$$\alpha_p(\lambda, r) = \sum n_i(r)\sigma_i^{ab}(\lambda, r) \tag{2.23}$$

where $n_i(r)$ [molecule cm^{-3}] is the concentration of the component i and $\sigma_i^{ab}(\lambda)$ [cm^2 $molecule^{-1}$] is the absorption cross section of the component i.

Figure 2.6 shows some molecular absorption coefficients between 250 and 1100 nm, for a temperature of 243 K which is representative of an altitude of 8 km above the sea level and is taken as average value of the free troposphere. The absorption cross sections are calculated from Hitran and UV/Vis spectra of atmospheric constituents [HITRAN database].

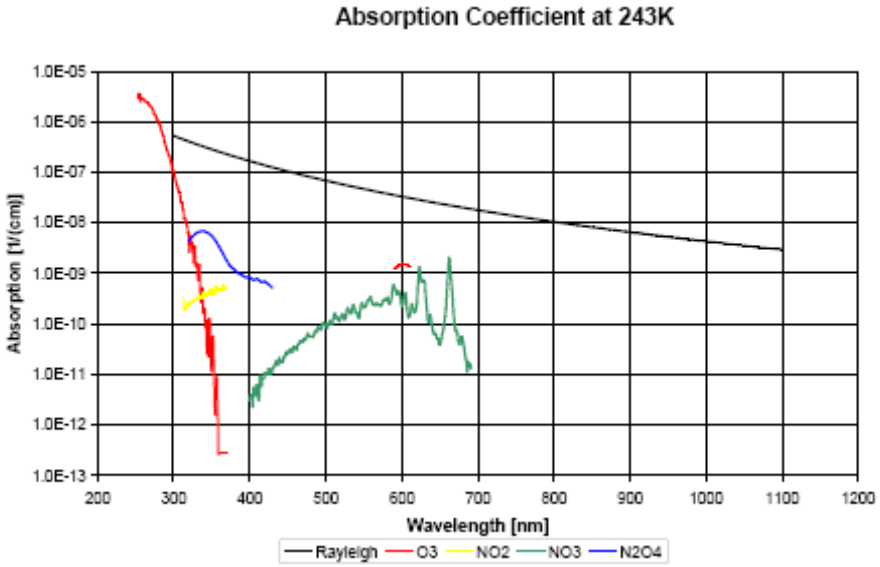

Figure 2.6. Molecular absorption coefficients at 243 K versus the wavelength.

Absorption by molecules is sometimes called "true absorption" to emphasize its difference from extinction due to scattering; or "selective absorption" to emphasize its concentration in narrow spectral bands. At the wavelengths of our interest (355, 387, 407, 532 and 607 nm), the absorption by atmospheric gases is minimal and can be ignored in the free troposphere. But, the ozone absorption will increase in the stratosphere due to the ozone layer, which absorbs in the Chappuis bands, in the orange part of the spectrum. Other absorbers are the water vapor (several bands in the longer-wavelength regions, noticed mainly under very humid conditions — hence the name "rain bands") and oxygen (which produces Fraunhofer's A and B bands).

2.5. Elastic Lidar equation

A typical lidar system (see Fig. 2.7) consists of a transmitter and a receiver. The transmitter emits short-time laser pulses into the atmosphere. The laser beam interacts with the atmospheric constituents as it propagates through a multitude of phenomena such as elastic light scattering (molecular-Rayleigh, aerosols-Mie), and inelastic (molecular–Raman) light scattering, fluorescence and absorption. A receiving telescope collects a very small fraction of the backscattered light. In addition to the telescope, the receiver usually contains a polychromatic filter for the spectral separation, high sensitivity photodetectors, and fast sampling rate analog-to-digital converters. The magnitude of the received signal is proportional to the number density of the atmospheric scatterers (molecules or aerosols), their intrinsic properties (i.e. probability of interaction with the electromagnetic radiation at the laser wavelengths, called cross–section value) and the laser incident energy. The 3rd chapter will describe the Naples lidar systems in detail.

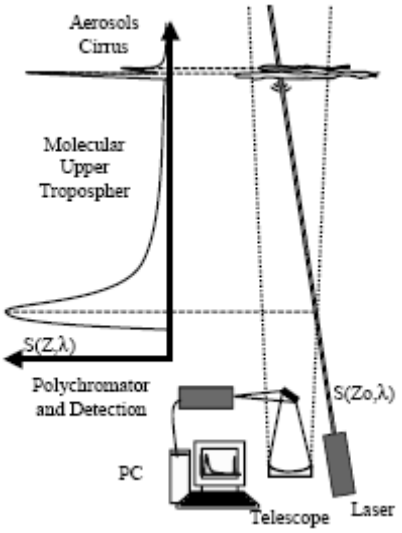

Figure 2.7. A schematic setup of a lidar system [Balin, 2004]

If the elastic (Rayleigh or Mie) scattering is considered, the detected light backscatter power P(z, λ) at the wavelength λ from a distance z can be expressed by the so-called lidar equation for single scattering, as follows:

$$P(z,\lambda) = P_L \frac{A_0}{z^2}\eta(\lambda)\xi(z,\lambda)\frac{c\tau}{2}\beta(z,\lambda)\exp\left[-2\int_0^z \alpha(r,\lambda)dr\right] \tag{2.23}$$

where P_L is the laser power, A_0/z^2 is the acceptance angle (A_0 is the collecting aperture area in the receiver), η is the efficiency, ξ(z) is the overlap function, β is the backscattering coefficient and α he extinction coefficient.
A variety of methods [Fenner, 1973; Klett 1981; Klett 1985; Sasano 1985; Krichbaumer and Werner 1994] have been proposed to obtain quantitative profiles of extinction and backscattering coefficients from an elastic lidar signal including both molecules and aerosols properties. The molecular atmosphere scattering properties, $\alpha_m(z)$ and $\beta_m(z)$, can be determined from appropriate standard atmosphere values; therefore only the aerosol scattering properties, $\alpha_p(z)$ and $\beta_p(z)$, have to be calculated from the measured power P(z). In any case, Eq. 2.23 is an ill-posed problem because two unknowns are related to only one equation.
A useful parameter is the aerosol lidar ratio (referred as S [sr], hereinafter), defined as follows:

$$S(z) = \frac{\alpha_p(z)}{\beta_p(z)} \tag{2.24}$$

where $\alpha_p(z)$ [m^{-1}] is the aerosol extinction and $\beta_p(z)$ [$m^{-1}sr^{-1}$] is the aerosol backscatter coefficient. The relationship between those two coefficients is a function of chemical and physical characteristics of aerosol but not of their number density. It has been shown [Klett, 1985] that if such ratio is known, the inversion of Eq. 2.23 is possible.
It has also been shown that the backscatter coefficient profile for a longer wavelength has less sensitivity to the lidar ratio than those for a shorter wavelength [Sasano, 1989].

Furthermore, another *a priori* information must be used to specify the value of the aerosol and molecular scattering properties at a reference altitude (referred as z_f, hereinafter). Then the solution for the total backscattering coefficient can be written as [Sasano, 1985]:

$$\beta_p(z)+\beta_m(z)=\frac{P(z)z^2\exp\left\{-2\int_{z_f}^{z}\left[S(r)-\frac{8\pi}{3}\right]\beta_m(r)dr\right\}}{\frac{P(z_f)z_{ref}^2}{\beta_p(z_f)+\beta_m(z_f)}-2\int_{z_f}^{z}S(r)P(r)r^2\exp\left\{-2\int_{z_f}^{z}\left[S(r')-\frac{8\pi}{3}\right]\beta_m(r')dr'\right\}} \quad (2.25)$$

The aerosol backscatter cross section is uniquely determined according to the physical and chemical properties of the aerosols (size, shape and index of refraction). The wavelength dependence of the backscatter coefficient is mainly dependent on the aerosol size distribution and refraction index. A multiwavelength lidar can, in principle, be used to measure the wavelength dependence of this coefficient. Different aerosol types are expected to have different size distribution and index of refraction, which implies that it may be possible to discriminate aerosol type according to the wavelength dependence [Sasano, 1989].

2.6. Raman lidar equation

A step towards a solution of the ill-posed problem of the elastic lidar equation is the additional use of Raman scattering. Indeed, the Raman backscattered signal from N_2 or O_2 molecules is affected by aerosol extinction but the backscatter coefficient is well known. Therefore, analysis of this signal alone permits the determination of the aerosol extinction [Leonard, 1967; Cooney, 1968; Inaba and Kobayashi, 1969; Melfi, 1969; Ansmann, 1990]. While the Raman lidar approach has the advantage of the simplicity in that one laser line can be used for a number of molecular species, it suffers in general from the reduced sensitivity and difficulty in daytime operation due to low Raman cross section. The Raman lidar equation for single scattering can be written as [Measures, 1992]:

$$P(z,\lambda_L,\lambda_R)=P_L\frac{A_0}{z^2}\eta(\lambda_R)\xi(z,\lambda_R)\frac{c\tau}{2}\beta(\lambda_L,\lambda_R,z)\exp\left[-2\int_0^z\left(\alpha(\lambda_L,r)+\alpha(\lambda_R,r)\right)dr\right] \quad (2.26)$$

where the backscatter coefficient $\beta(\lambda_L, \lambda_R, z)$ at the elastic wavelength λ_L and Raman wavelength λ_R is linked to the differential Raman backscatter cross section $d\sigma/d\Omega$ of a gas with a molecule number density N(z) by the relation:

$$\beta(\lambda_L,\lambda_R,z)=N(z)\frac{d\sigma(\lambda_L,\lambda_R,\pi)}{d\Omega} \quad (2.27)$$

The profiles of either nitrogen of oxygen can be used since these molecules are well mixed in the atmosphere and their number densities are usually well known. Thus, the extinction coefficients are given by:

$$\alpha_p(\lambda_L, z) + \alpha_p(\lambda_L, z) = \frac{d}{dz} \ln\left\{ \frac{\xi(z)N(z)}{P(z)z^2} \right\} - \alpha_m(\lambda_L, z) + \alpha_m(\lambda_R, z) \tag{2.28}$$

Particle scattering is assumed to have an Angstrom coefficient equal to *a* and since $\Delta\lambda/\lambda_L$ is small, Eq. 2.28 can be written approximately as

$$\alpha_p(\lambda_L, z) = \frac{\frac{d}{dz} \ln\left\{ \frac{\xi(z)N(z)}{P(z)z^2} \right\} - \alpha_m(\lambda_L, z) + \alpha_m(\lambda_R, z)}{1 + \left(\frac{\lambda_L}{\lambda_R} \right)^k} \tag{2.29}$$

For particles and water droplets with diameters comparable with the measurement wavelength, k = 1 is an appropriate value, while in the case of large particles and ice particles, which are usually large compared with the laser wavelength, k = 0 is justified.
The particle backscatter coefficient $\beta_p(\lambda_L, z)$ can be determined by using both elastically and Raman backscattered signals [Cooney, 1969; Melfi, 1972].

2.7. Water vapour mixing ratio

The water vapour mixing ratio is defined as the mass of water vapour per unit mass of dry air. It can be obtained from the measurement of the water vapour to reference gas ratio, where the reference gas is either oxygen or nitrogen [Melfi, 1969; Melfi, 1985; Ansmann, 1992; Whiteman, 1992; Sherlock, 1998]. Using two Raman lidar equations for the wavelengths λ_{H_2O} and λ_R, forming the signal ratio, and rearranging the terms, the resulting equation, the mixing ratio m(z) is obtained as

$$m(z) = K_m \frac{P(z_f, \lambda_L, \lambda_{H_2O})}{P(z_f, \lambda_L, \lambda_R)} \frac{\exp\left\{ -\int_0^z \left[\alpha(\lambda_{H_2O}, r) \right] dr \right\}}{\exp\left\{ -\int_0^z \left[\alpha(\lambda_R, r) \right] dr \right\}} \tag{2.30}$$

where m(z) [g_{H_2O} g^{-1}dry air] is the water vapour mixing ratio, K_m [g/kg] is the overall system calibration constant and can in principle be deduced from the known Raman cross sections and the measured properties of the receiver's spectral transmission, but in practice it is determined from comparison of the lidar measurement with evaluated data from radiosonde.

2.8. Depolarization ratio

A useful quantity to characterize the shape of the aerosols is the depolarization ratio ρ, commonly defined as the ratio of the backscatter coefficients for scattering perpendicular and parallel relative to the polarization of the transmitted laser beam, $\beta_\perp$ and $\beta_{//}$, respectively,

$$\rho(z) = \frac{\beta_{\perp}(z)}{\beta_{\parallel}(z)} \tag{2.31}$$

The molecular backscatter coefficients in Eq. 2.31 may depend on atmospheric temperature and thus on height. ρ(z) is measured with polarization lidar as:

$$\rho(z) = k\frac{P_{\perp}(z)}{P_{\parallel}(z)} \tag{2.32}$$

where $P_{\perp}$ and $P_{//}$ are the lidar signals with polarization perpendicular and parallel to the polarization of the transmitted laser light, respectively, and *k* is a calibration factor equal to the inverse of the ratio of the channel efficiencies. Generally, the efficiency of the lidar receiver is not the same for the parallel and the perpendicular channel and *k* can be determined by two methods [Behrendt, 2002]:

- experimentally by comparing the signals of both lidar channels when coupling unpolarized light into the receiver.
- by normalizing ρ(z) to the value of the molecular depolarization ratio at a altitude R where only the molecular contribution to the lidar signal is expected.

2.9. Retrieval of microphysical aerosol parameters

The size distribution and the chemical composition are key parameters for aerosols. Lidar systems can deliver information on particle extinction and backscatter coefficients at multiple wavelengths. This information can be used to derive physical particle properties as particle size, number, surface-area, and volume concentration, as well as the complex refractive index. The problem of determining these properties by multispectral lidar measurements belongs to a class of inverse ill-posed problems.

Several methods were applied to solve this problem: the singular value decomposition method [Yoshiyama, 1996], the iterative method [Rajeev, 1998], the regularization method [Muller, 1999; Muller, 2000] and the hybrid regularization method [Böckmann, 2001].

Within the frame of the EARLINET project (for more information, see the 3rd chapter), a program was developed by the Institute of Mathematics of the University of Potsdam (IMP) based on the hybrid regularization method. The IMP mathematical model, which relates the optical and the physical particle parameters, consists of a system of two Fredholm integral equations of the first kind for the backscatter and extinction coefficients. This set of equations is reformulated into a more specific and more solid form as follows:

$$\alpha_p^{ext} = \int_{R_{\min}}^{R_{\max}} \frac{3}{4r} Q_{ext} v(r) dr = \int_{R_{\min}}^{R_{\max}} K_p^{v} v(r) dr$$

$$\beta_p^{\pi} = \int_{R_{\min}}^{R_{\max}} \frac{3}{4r} Q_{\pi} v(r) dr = \int_{R_{\min}}^{R_{\max}} K_p^{\pi} v(r) dr \tag{2.33}$$

where v(r) is the volume concentration distribution [$\mu m^3\ cm^{-3}\ \mu m^{-1}$], K is the volume extinction (or backscatter) kernel and R_{min}, R_{max} are the minimum and maximum radius of the distribution.

A hybrid regularization method is applied that uses variable projection dimension and variable B-spline order as well as truncated singular-value decomposition (TSVD) simultaneously for that ill-posed inversion [Böckmann, 2001]. This method can be used with a known or an unknown refractive index. In the latter case, by using a refractive index grid between suitable limits, this method is performed for each grid point and the solution or set of solutions is the one which minimizes the errors between the input extinction and backscatter coefficients and the calculated coefficients using Mie theory.

3.0. Multiple scattering

The scheme for deriving the optical parameters of the atmosphere is based on inversion of the Eqs. 4.2 and 4.5. But in these equations only the first order scattering (single scattering) is considered, as multiple scattering (referred as MS, hereinafter) is negligible in many applications. But when the optical depth of the atmospheric target is not negligible or the phase function of the scattering particles is strongly forward peaked, as in cirrus clouds, or the observation is from long distance, the MS contribution to the lidar signals cannot be neglected. In general, in MS conditions, the preferred forward scattering by particles produces an enhancement of forward path of photons, thus leading to a measured aerosol extinction coefficient lower than its actual value.

Since the early 1970's a variety of MS models for lidar applications has thus been developed [Liou, 1971]. By Monte Carlo simulations, Platt [Platt, 1977] found that MS is significant in cirrus clouds and varies with cloud optical depth, cloud extinction, and lidar penetration depth.

An important experimental evidence of MS contribution to lidar signal is found in the analysis of data from lidar in-space technology experiment (LITE) as found in the work by Buscaglioni et al. [Buscaglioni et al., 1995].

An overview of state-of-the-art MS modelling has been worked out in a collaboration of groups involved in the Multiple-Scattering Lidar Experiments (MUSCLE) workshop series [Flesia, 1995]. In a common effort these groups have compared and discussed the results obtained with various models.

The contribution to MS to backscattering and extinction coefficient has been also analyzed by Wandinger [Wandinger, 1998], who considered phase functions pertaining to different scattering media such as clouds at low and high range. In particular, for different altitudes, clouds such as cumulus, nimbostratus, spherical water drops and cirrus ice crystal were studied respectively.

Wang [Wang, 2005] reports the results of a Monte Carlo-based iterative procedure to evaluate the effects of multiple scattering in Raman lidar returns. By solving the inverse problem, the experimental values of backscatter and extinction coefficients can be corrected. The results showed that whereas backscattering coefficient profile is almost unaffected by multiple scattering, the effective extinction coefficient is up to a factor of 2.5 larger than the effective one.

Different parameters are known to determine the intensity of multiple-scattered light. On one hand, the measurement geometry is important. In fact, the larger the volume from which scattered light is detected, the larger is the MS effect. Therefore, the intensity of multiple-scattered light increases with increasing laser beam divergence, increasing receiver field of view (referred as RFOV, hereinafter), and increasing distance between the light source and the scattering volume. For example, the MS effect is much larger for a space-based than for a ground-based system if the same cloud is detected with the same RFOV [Winker, 1995]. On the other hand, the scattering medium itself determines the MS influence. For example, optical depth and the size of the scattering particles are important. Because of the low laser beam divergence and the narrow RFOV used by lidars, forward scattering from large (compared with the laser wavelength) particles is the most important process in this context. The larger the particles, the more photons are scattered into the forward direction.

3.1 Conclusion

This chapter describes the lidar equations involved in the multiple-wavelength lidar system. A special attention has been devoted also to the Rayleigh and Mie scattering theories.
The optical characterization of the atmospheric aerosol can be performed just using the properties of the interaction between the radiation and the atmosphere. Moreover, this chapter also shows that the lidar technique is a powerful tool to measure and monitor the optical parameters of the atmosphere with high spatial and temporal evolution.

3.1. References

Angstrom, **The parameters of atmospheric turbidity**, Tellus 16, 64-75, (1964).

Ansmann, A., M. Riebesell, et al., **Combined Raman Elastic-Backscatter Lidar for Vertical Profiling of Moisture, Aerosol Extinction, Backscatter, and Lidar Ratio**, Applied Physics B-Photophysics and Laser Chemistry **55**(1): 18-28, (1992).

Ansmann, A., M. Riebesell, et al., **Measurement of Atmospheric Aerosol Extinction Profiles with a Raman Lidar**, Optics Letters **15**(13): 746-748, (1990).

Balin I., **Measurement and analysis of aerosols, cirrus-contrails, water vapour and temperature in the upper troposphere with the Jungfraujoch lidar system,** PhD Thesis, (2004).

Behrendt A., Nakamura T., **Calculation of the calibration constant of polarization lidar and its dependency on atmospheric temperature,** Optics Express, vol. 10, No.16, pp. 805-806, (2002).

Böckmann, C., **Hybrid regularization method for the ill-posed inversion of multiwavelength lidar data in the retrieval of aerosol size distribution**, Applied Optics **40**(9): 1329-1342, (2001).

Böckmann, C., and Wauer, J., **Algorithms for the inversion of light scattering data from uniform and non-uniform particles**, Aerosol Science **32**: 49-61, (2001).

Bodhaine, B. A., **On Rayleigh Optical Depth Calculations**, American Meteorological Society **16**: 1854-1861, (1999).

Bohren, C. F., and Huffman, D. R., **Absorption and scattering of light by small particles**, New-York, Wiley, (1983).

Bruscaglioni P., A. Ismaeli, and G. Zaccanti, **Monte Carlo calculations of LIDAR returns: procedure and results**, Appl. Phys. B **60,** 325–330, (1995).

Cooney, J., **Measurements of the Raman component of Laser Atmospheric backscatter**, Applied Physics Letters **12**(2): 40-42, (1968).

Cooney, J., **Measurements Separating the Gaseous and Aerosol Components of Laser Atmospheric Backscatter**, Nature **224**: 1098-1099, (1969).

Fenner, W. R., H. A. Haytt, et al., **Raman cross sections of simple gases**, Journal of the Optical Society of America **63**(1): 73-77, (1973).

Flesia C. and P. Schwendimann, **Analytical multiple scattering extension of the Mie theory: The lidar equation**, Appl. Phys. B **60,** 331–334, (1995).

Hinkley, E. D., **Laser Monitoring of the Atmosphere**, Springer-Verlag, (1976).

HITRAN, database, http://cfa-www.harvard.edu/hitran/

Inaba, H. and T. Kobayashi, **Laser-Raman Radar for Chemical Analysis of Polluted Air**, Nature **224**: 170-172, (1969).

Klett, J. D., **Stable analytical inversion solution for processing lidar returns**, Applied Optics **20**: 211-220, (1981).

Klett, J. D., **Lidar inversion with variable backscatter/extinction ratios**, Applied Optics **24**(11): 1638-1643, (1985).

Krichbaumer, W. and C. Werner, **Current state of-the-art of lidar inversion methods for atmospheres of arbitrary optical density**, Applied Physics B-Lasers and Optics **59**: 517-523, (1994).

Leonard, D. A., **Observation of Raman Scattering from the Atmosphere using a Pulsed Nitrogen Ultraviolet Laser**, Nature **216**: 142-143, (1967).

Liou K. N. and R. M. Schotland, **Multiple backscattering and depolarization from water clouds for a pulsed lidar system**, J. Atmos. Sci. **28,** 772–784, (1971).

Mc Cartney, E. J., **Optics of the Atmosphere**, Wiley, (1976).

Measures, R. M., **Laser Remote Sensing. Fundamentals and Applications**, New-York, Krieger, (1992).

Melfi, S. H., **Remote Measurements of the Atmosphere Using Raman Scattering**, Applied Optics **11**(7): 1605-1610, (1972).

Melfi, S. H., J. D. Lawrence, et al., **Observation of Raman Scattering by Water Vapour in the Atmosphere**, Applied Physics Letters **15**(9): 295-297, (1969).

Melfi, S. H. and D. Whiteman, **Observation of Lower-Atmospheric Moisture Structure and Its Evolution Using a Raman Lidar**, Bulletin of the American Meteorological Society **66**(10): 1288-1292, (1985).

Muller D., Wagner, F., Wandiger, U., Ansmann, A., Wendisch, M., Althausen, D., and Hoyningen-Huene, W., **Microphysical particle parameters from extinction and backscatter lidar data by inversion with regularization: experiment**, Applied Optics **39**(12), 1879-1892, (2000).

Muller D., Wandiger, U., and Ansmann, A., **Microphysical particle parameters from extinction and backscatter lidar data by inversion with regularization: simulation**, Applied Optics **38**(12): 2358-2368, (1999).

Muller D., Wandiger, U., and Ansmann, A., **Microphysical particle parameters from extinction and backscatter lidar data by inversion with regularization: theory**, Applied Optics **38**(12): 2346-2357, (1999).

Platt C. M. R, **Remote sounding of high clouds. III: Monte Carlo calculations of multiple-scattered lidar returns**, J. Atmos. Sci. **38,** 156–167, (1981).

Rajeev, K., and Parameswaran, K., **Iterative method for the inversion of multiwavelength lidar signals to determine aerosol size distribution**, Applied Optics **37**(21), 4690-4700, (1998).

Sasano, Y., and Browell, E., V., **Light scattering characteristics of various aerosol types derived from multiple wavelength lidar observations**, Applied Optics **28**(9), 1670-1679, (1989).

Sasano, Y., Browell, E., V., and Ismail S., **Error caused by using a constant extinction/ backscattering ratio in the lidar solution**, Applied Optics **24**(22), 3929-3932, (1985).

Seinfeld, J. H. and S. N. Pandis, **Atmospheric Chemistry and Physics**, Wiley Interscience, (1998).

Wang et al., **An algorithm to determine cirrus properties from analysis of multiple-scattering influence on lidar signals**, Appl. Phys. B 80, 609-615, (2005).

Wandinger, U., **Multiple-scattering influence on extinction- and backscatter- coefficient measurements with Raman and high-spectral- resolution lidars**, Applied Optics **37**(3), 417-427, (1998).

Whiteman, D. N., S. H. Melfi, et al., **Raman Lidar System for the Measurement of Water-Vapour and Aerosols in the Earths Atmosphere**, Applied Optics **31**(16), 3068-3082, (1992).

Winker D. M. and L. R. Poole, **Monte-Carlo calculations of cloud returns for ground-based and space-based lidars**, Appl. Phys. B **60,** 341–344, (1995).

Yoshiyama, H., Ohi, A., and Ohta, K., **Derivation of the aerosol size distribution from a bistatic system of a multiwavelength laser with the singular value decomposition method**, Applied Optics **35**(15): 2642-2648, (1996).

Introduction

The urban area of Naples is characterized by a large amount of anthropogenic aerosol produced by combustion system and vehicular traffic. Moreover, due to its location, the city of Naples is also characterized by frequent strong presence of Saharan dust carried out from North Africa and by circulation phenomena like land/sea breeze. Therefore, the study and the monitoring of the evolution of aerosols are very interesting in this area.

Since February 2000 the Naples lidar group is part of EARLINET (**E**uropean **A**erosol **R**esearch **LI**dar **NET**work), the European network on aerosol research by lidar measurements. EARLINET provides a quantitative, comprehensive and statistically significant database of the horizontal, vertical and temporal distribution of aerosols on continental scale.

The Naples multiwavelenghts Raman lidar system is located in the laboratories of the Physics Department at the University of Naples "Federico II".

In this chapter the experimental setup of this system is described in detail. The way to take into account the incomplete overlap between the laser beam and the receiver field of view which affects lidar observations of particle optical properties in the near range is also discussed.

Moreover, data treatment and error propagation in the data analysis are discussed. For the retrieval of the backscattering and the extinction profiles, the Raman method is used for night-time measurements, while the Klett-Fernald inversion is used for daytime measurements.

3.0. The Naples lidar system

The lidar system of the present work is a monostatic multiwavelenghts Raman lidar, mainly used for aerosol measurements in the troposphere. Aerosol optical properties in the UV and visible regions such as backscatter, extinction water vapour mixing ratio and the Angstrom exponent profiles can be retrieved from this system. The Naples station also provides complementary ground data of temperature, pressure, humidity, wind speed and direction.

The system took part in several International campaigns such as LITE, EAQUATE, LAUNCH, and CALIPSO [LITE, EAQUATE, LAUNCH and CALIPSO webpages].

Fig. 3.1 shows two pictures of the Naples lidar system.

Figure 3.1. Two pictures of the Naples lidar system. External view of the container (on the left) and details of the optical assembly (on the right).

Fig. 3.2 shows the general layout of the multiwavelenghts Raman lidar system at the Naples station; the main technical characteristics are summarized in Table 3.1.

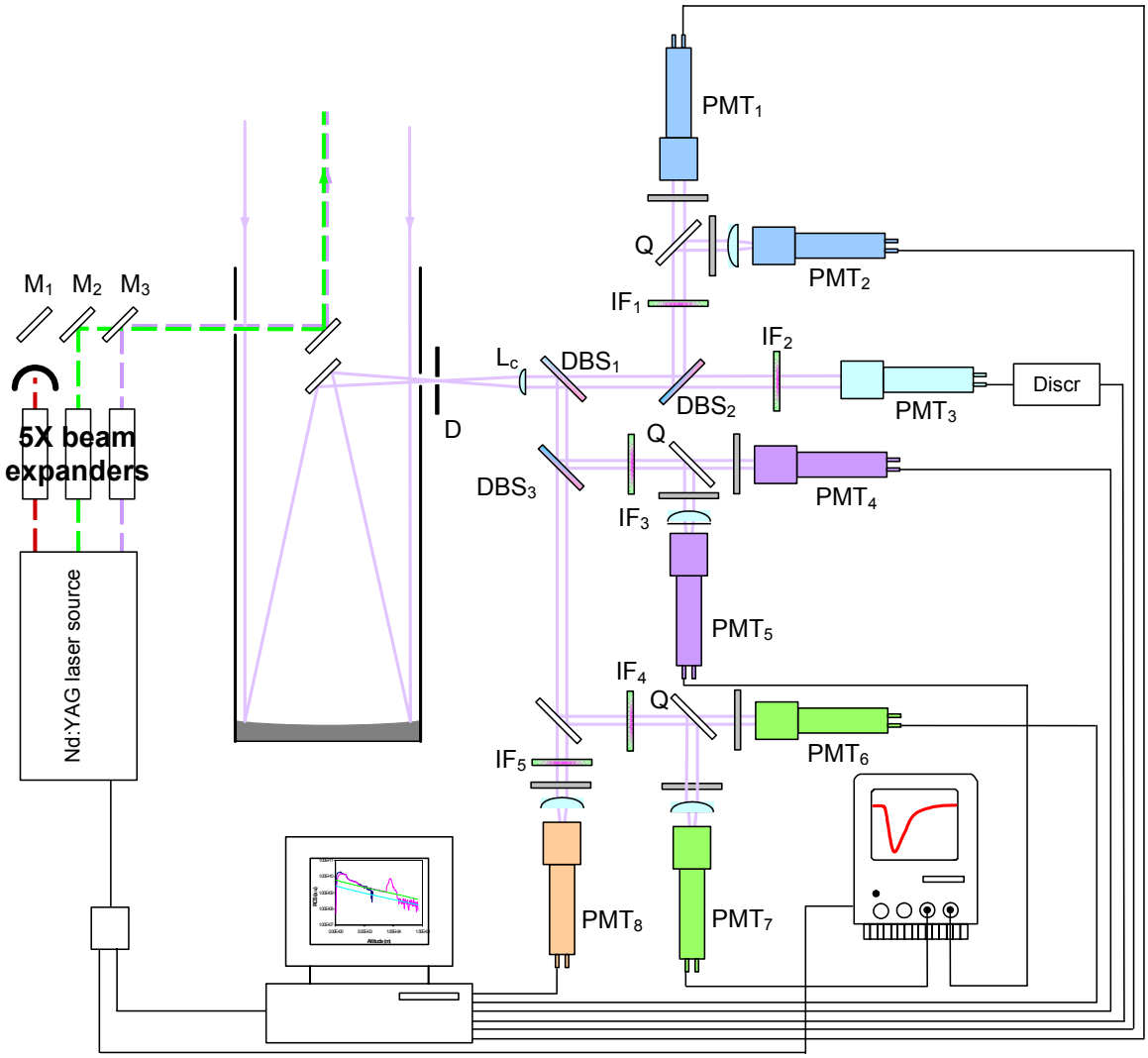

Figure 3.2. The experimental layout of the lidar system installed at the Naples station. The diaphragm D selects the telescope field of view at 1. 33 mrad. Fused silica plan-convex lens (L_c) is used to collect the backscattered light. The beam is separated from a system of dichroic beam splitters DBS_i; IF_i are the 0.5 nm bandwidth interference filters and PMT_i are the photomultipliers (for more information, see also Table 3.1). Moreover, grey filters are used to prevent photocathode saturation.

Table 3.1. Main characteristics of the Naples lidar system. For more information, see also Fig. 3.2

LASER SOURCE	
Type	Nd-Yag
Wavelength (nm)	355; 532
Pulse width (ns)	5
Energy (mJ)	100 @ 355 nm; 90 @ 532 nm
Repetition rate (Hz)	20
Divergence (mrad)	0.1 @ 355 nm; 0.5 @ 532 nm
RECEVEING SYSTEM	
Newtonian telescope	30 cm (diameter)
Field of view (mrad)	1.33
Elastic channel analog @ 355 nm (PMT_5)	Bandwidth 0.5 nm
Elastic channel analog @ 532 nm (PMT_7)	Bandwidth 0.5 nm
Elastic channel photocounting @ 355 nm (PMT_4)	Bandwidth 0.5 nm
Elastic channel photocounting @ 532 nm (PMT_6)	Bandwidth 0.5 nm
Raman N_2 channel @ 387 nm (PMT_1 and PMT_2)	Bandwidth 0.5 nm
Raman N_2 channel @ 607 nm (PMT_8)	Bandwidth 0.5 nm
Raman H_2O channel @ 407 nm (PMT_3)	Bandwidth 0.5 nm

The Naples lidar system is a monostatic lidar with respect to all available wavelengths. This means that the telescope optical axis is coincident with the laser beam axis. The advantage to use this configuration instead of the bi-static one (where the telescope optical axis is parallel to the laser beam axis) is the possibility to detect the backscattering at lower height.
The transmitter is a pulsed Nd:YAG laser (QUANTEL mod. Brilliant-B), equipped with two non-linear crystals for second and third harmonic generation. The repetition rate is 20 Hz, the maximum pulse energy for each wavelength is 0.65 J, 0.35 J and 0.15 J for 1064, 532 and 355 nm, respectively. Beam divergence is 0.5 mrad and pulse duration is 5 nsec.
At the output of the third harmonic generator, in order to reduce the divergence of the laser beam the three wavelengths (1064, 532 and 355 nm) are expanded by a factor of five before being transmitted into the atmosphere. This is done by three beam-expanders optimized for each wavelength.
The expanded beams are directed into the atmosphere by dielectric mirrors, which are able to have high values of reflectivity.
After atmospheric interactions, the elastic backscattered radiations at 355 and 532 nm (the backscattered radiation at 1064 nm is not yet detected), and the Raman shifted backscattered signals at 387 nm (nitrogen shift from 355 nm), 407 nm (water vapour shift from 355 nm) and 607 nm (nitrogen shift from 532 nm) are collected by a Newtonian-type telescope. It has a 30 cm spheric primary mirror and its focal length (F) is 120 cm. A secondary mirror reflects the converging light through a diaphragm (D) and a plano-convex lens (L_c) provides the collimation of the beam.
The diaphragm is in the focal plane of the telescope and sets the field of view (referred as FOV, hereinafter) of the receiver. From simple geometric considerations the telescope FOV can be expressed as a function of the diaphragm diameter D and the telescope focal length F:

$$\mathrm{FOV} \cong \frac{D}{F} \tag{3.1}$$

As Eq. 3.1 shows, the larger is the diaphragm diameter, the larger is the FOV and so it is possible to lower the minimum height of full overlap. But, on the other hand, the larger is the diaphragm the greater are some unwanted effects. In fact, with increasing the telescope field of view, multiple scattering and background light increase leading to an uncorrected estimation of retrieved optical parameters and to a worse signal to noise ratio, respectively. A good arrangement has been obtained with a field of view of 1.3 mrad, corresponding to a diaphragm diameter of 1.6 mm. Actually, before performing measurements, in order to check the alignment of the lidar system with high accuracy, it can be useful to use a diaphragm with a smaller diameter.
The optical receiver ensures the spectral separation of the elastic backscattered signal and also the N_2 and H_2O Raman backscattered ones. The filter polychromators are built by a set of beam-splitters (BS) and interference filters (IF) with high out-of-band rejection. The beamsplitters, optimized for the different wavelengths, operate at a 45^o angle of incidence. The choice of IF has been done taking into account two opposite requirements: it should have a relatively broad bandwidth to collect as much signal as possible, but it should work as a blocker for background radiation.
The backscattered signals at 355, 387, 407, 532 and 607 nm are detected by photomultiplier tubes (referred as PMT, hereinafter), which convert the optical signal into an electrical signal. The basic technical characteristics in determining the choice of a photodetector include the spectral response, the quantum efficiency, the frequency response, the gain, and the dark current. In most cases, the wavelength of the detected signal constitutes the primary factor in selecting the class of photodetector to be employed. For wavelengths that range between 200 and 1000 nm photomultipliers are generally preferred because of their high gain and low noise. For the near-infrared wavelengths, photodiodes and in particular avalanche photodiodes are a good compromise.
PMT have fast response, high gain and high enough quantum efficiency and relatively low noise levels. Many studies have examined the influence of the PMT linearity, the dynamic range and the signal induced noise on the quality of the lidar signal [Cairo 1966; Pettifer 1975; Swinesson 1991]; generally there was less concern about the effect of the PMT spatial uniformity on the signal. The spatial uniformity of the PMT is defined as the variation of its sensitivity with the position of incident light on the photocathode.
In order to reduce the effects of possible spatial non-uniformity in the PMT photocathode, one plano-convex lens (L) is positioned in front of the photocathode (in direct contact with its entrance window) in order to spread the incoming light more homogeneously over the photocathode surface. Moreover, grey filters are inserted in front of photocathode and are employed to adapt the light intensity of the signals to the corresponding PMT sensitivity in order to prevent the photocathode saturation. The choice of the grey filters depends on the atmospheric conditions (e.g., clear sky, high concentration of aerosol), the time of the measurement (day, night) and the type of the detected radiation (elastic or Raman backscatter signal).
Non-linearities due to dead time phenomenon can be corrected through the following formula:

$$N = \frac{n}{1 - nT} \tag{3.2}$$

where N is the true count rate, n is the measured count rate and T is the count rate correction factor (it is specified from factory).
In order to extend the dynamic range of the elastic signal, both analog and photon-counting modes are used. Analog acquisition is done by a Tektronix oscilloscope: a rough space resolution of 3 m is

obtained by sampling the atmosphere with a time resolution of 20 nsec. The oscilloscope is computer controlled by means of an IEEE 488 card. Far range elastic signals are detected by means of two Hamamatsu photo-counting heads (mod. H6180-01) and they are acquired through two EG&G Ortec MCS-PCI boards, with a time resolution of 100 nsec for 200 μsec (corresponding to 15 m space resolution for a distance of 30 km). Also the acquisition of the N_2 Raman channel at 387 nm is splitted into two parts, both acquired in photon-counting mode. Table 3.2 summarizes the PMT used for each channel.

Table 3.2. Photomultipliers used for the acquisition channels.

Elastic 355 nm	
PMT low height (analog)	Hamamatsu mod. R2079 select
PMT high height (photon-counting)	Hamamatsu mod. H-6180-01
Elastic 532 nm	
PMT low height (analog)	EMI mod. 9202 QB
PMT high height (photon-counting)	Hamamatsu mod. H-6180-01
Raman N_2 (387 nm)	
PMT low height (photon-counting)	EMI mod. P25PC
PMT high height (photon-counting)	Hamamatsu mod. H-6180-01
Raman H_2O (407 nm)	
PMT (photon-counting)	Hamamatsu mod. R1828-02
Raman N_2 (607 nm)	
PMT (photon-counting)	Hamamatsu mod. H-6180-01

If there are two acquisition channels for the same signal (one optimized for low height and the other for high height, respectively), the merging of the two profiles is performed. A fit between the two signals is performed, generally in the range 3000-5000 m. By this procedure, the analog signal is used for low height below the merging height (z^*, in the range 3000-5000 m) and the photon-counting signal is used for high height above z^*. Fig. 3.3 shows in blue line the analog elastic range corrected signal (referred as RCS, hereinafter) and in pink line the photon-counting RCS optimized for high height, at 355 nm.

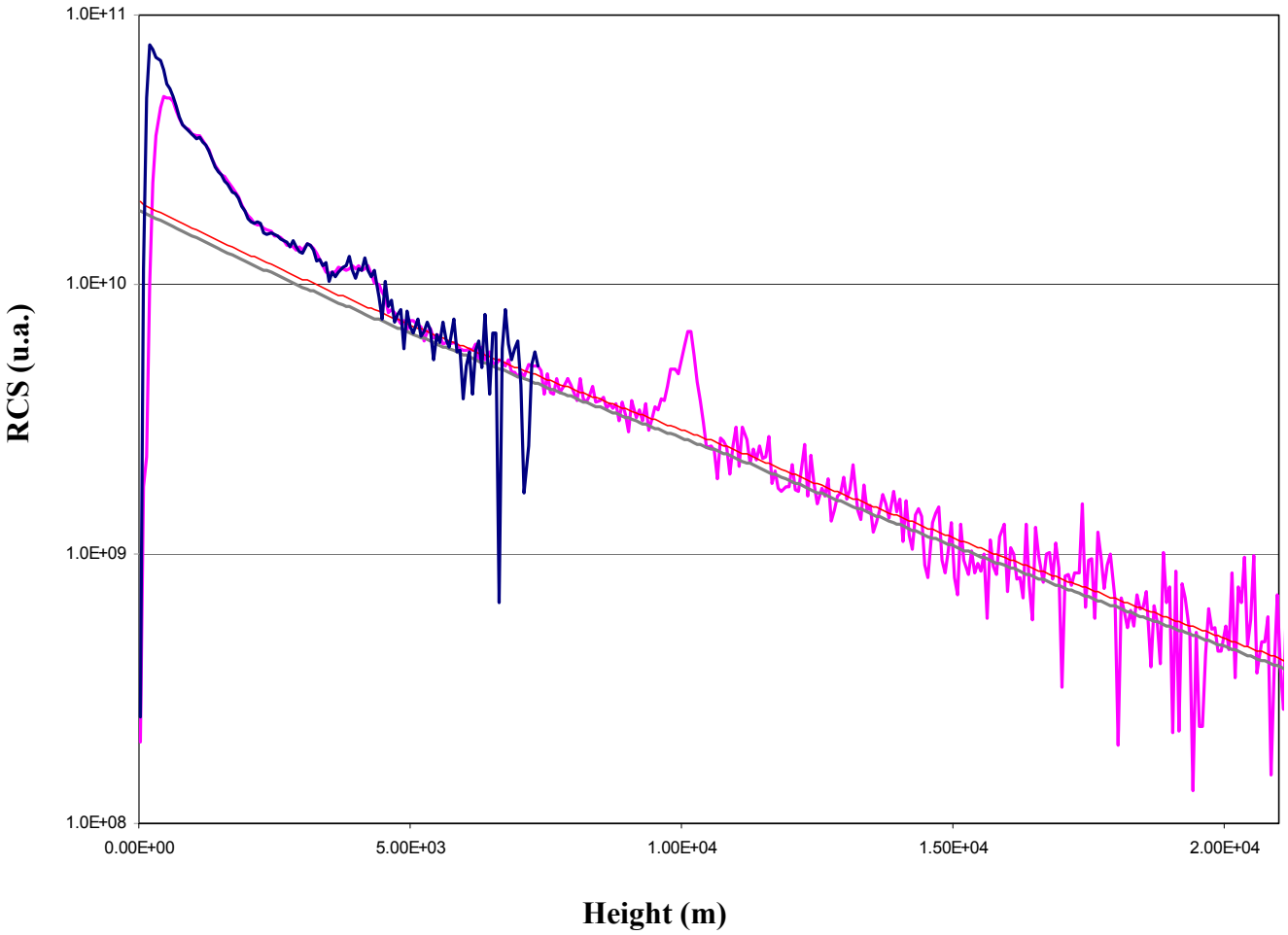

Figure 3.3. The vertical profile of the Range Corrected Signal (RCS) at 355 nm. The blue line indicates the analog elastic signal, the pink line indicates the photocounting elastic signal. The red and grey line indicates the molecular profile, fitting the signal after and before the cirrus cloud (clearly visible in the pink line at about 10 km), respectively.

3.1. Ancillary systems

Meteorological parameters at ground level are acquired by means of temperature, pressure, relative humidity, speed and direction of the wind. Those data are needed because lidar signal is strictly linked to physical atmospheric parameters that affect the collected signal through of backscatter and extinction coefficients. The knowledge of the temporal behaviour of meteorological parameters is useful to understand the atmospheric dynamics at ground level as well.
Data are acquired with a temporal resolution of one second and averaged over one minute.

3.2. EARLINET

The European Aerosol Research LIdar NETwork (EARLINET) project started in February 2000 in order to establish a quantitative, comprehensive and statistically significant database of the horizontal, vertical and temporal distribution of aerosols on continental scale. The goal is to provide aerosol data with unbiased sampling, for important selected processes, and air-mass history, together with comprehensive analyses of these data. At present, EARLINET consists of 25 stations (see Fig. 3.4): 16 Raman lidar stations, including 8 multi-wavelength Raman lidar stations which are used to retrieve aerosol microphysical properties.
EARLINET performs a rigorous quality assurance program for instruments and evaluation algorithms.

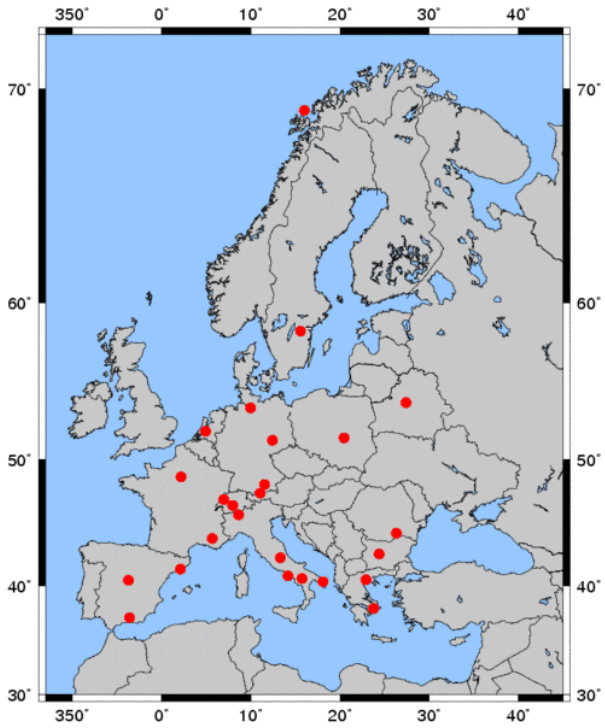

Fig. 3.4 EARLINET lidar stations (red circles) in the year 2007

EARLINET contributes to the understanding of the aerosol long range transport and their influence on the clouds modifications. A major effort is spent to evaluate the human contribution to particles emissions, so special care is taken in analysis of anthropogenic aerosol source and their concentrations, the quantification of their budgets, radiative properties and prediction of future trends.

At the moment the network is fully operational according to a protocol that schedules three measurements per week to obtain unbiased data for climatological studies. Furthermore, since June 2006 EARLINET is involved in the NASA-CALIPSO project (for more information, see Chapter 6), whose protocol schedules measurement in coincidence with the CALIPSO satellite overpasses.

Measurements are also realized in case of special events like long range transport events, volcanic eruptions, forest fire.

EARLINET-ASOS (European Aerosol Research LIdar NETwork – Advanced Sustainable Observation System) is a 5-year EC Project started in 2006. Based on the EARLINET infrastructure, it will provide appropriate tools to improve the quality and availability of the continuous observations.

The project is addressing the optimization of instruments and algorithms existing within EARLINET, and exchanging expertise, with the main goal to build a database with high quality aerosol data.

3.3. The overlap function

The incomplete overlap (for more information, see Chapter 2, Eq. 2.23) between the laser beam and the receiver field of view significantly affects lidar observations of particle optical properties in the near range. Without correction of the range-dependent overlap characteristics, a proper study of the important exchange processes of anthropogenic pollution between the sources and the lower layers of the troposphere is not possible.

The theoretical development of the overlap function (ξ) is given by Measures, [Measures, 1992]. This factor depends on the telescope field of view and primary diameter, the laser beam divergence and diameter as a function of the altitude, and the angle and the distance between the axes of the laser beams and of the receiver. In monostatic lidar, the ξ function corrects the underestimation due

to the shadow of the secondary mirror of the telescope (see Fig. 3.5), which stops the atmospheric backscatter photons coming from low heights.
A good knowledge of the overlap function is very important, because the bulk of the aerosol is in the lower atmosphere. Several methods have been proposed to determine the overlap function profile.

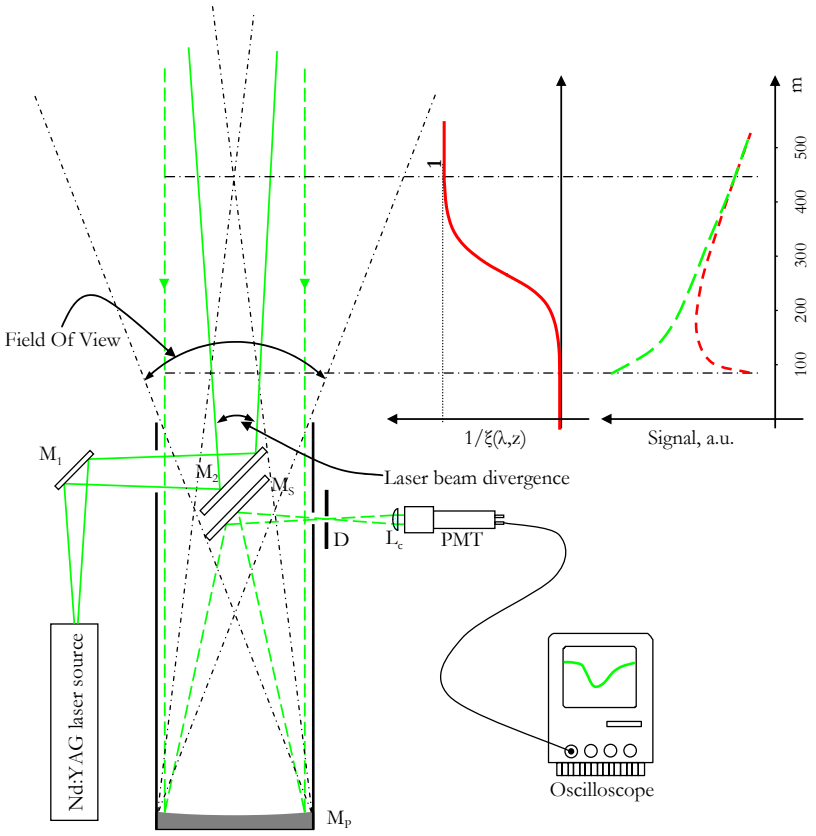

Fig. 3.5 Geometrical description of the overlap correction.

For theoretical approaches, a good understanding of the actual laser distribution in the laser beam cross section, the beam divergence, the beam direction, and the characteristics of the receiver unit is needed to obtain an overlap profile with sufficient accuracy. However this approach requires rough approximations about the system: the laser beam is supposed to be Gaussian and its divergence should be small compared with telescope field of view, all optics should be aberration free, PMT sensitive surface should be uniform. Often, all these hypotheses are not verified in a real lidar system. In particular, for the Naples lidar systems the following conditions are not satisfied: the laser beam is not Gaussian, the singlet collimating lens suffers for chromatic aberration and the laser spot image falls on quite different parts of the sensitive area on the photocathode depending from the altitude of the object plane focalized on the sensible area.
Another method is based on the application of optical ray tracing software, but its application in our case is limited by the complexity of receiving system. In addiction, this approach may need using parameters that are not easily known.
An experimental approach has been used in our experiment using a rotating mirrors system, by which the lidar can be pointed horizontally. If the atmosphere is stable and uniformly stratified, the extinction $\alpha(z)$ and backscatter $\beta(z)$ coefficients in the lidar equation can be considered as constant (α_0 and β_0, respectively), and the lidar equation can be written as (for the explanation of the terms, see Chapter 2 Eq. 2.23):

$$P(\lambda,z)=P_L\frac{A_0}{z^2}\eta(\lambda)\xi(z,\lambda)\frac{c\tau}{2}\beta_0\exp\left[-2\int_0^z\alpha_0 dr\right] \tag{3.2}$$

and with some simple operations:

$$z^2P(\lambda,z)=K\cdot\xi(\lambda,z)e^{-2\alpha_0 z}\quad\Rightarrow\quad\ln\left[z^2P(\lambda,z)\right]=K'+\ln\left[\xi(\lambda,z)\right]-2\alpha_0 z \tag{3.3}$$

In the constants K and K', all the terms independent from the altitude *z* are grouped.
When z is larger than some kilometres, we can take 1 for the overlap function: $\xi(\lambda,z)\to 1$. So the Eq. 3.3 can be written as:

$$\ln\left[z^2P(\lambda,z)\right]=K'-2\alpha_0 z \tag{3.4}$$

that is a linear relation of the range corrected signal (referred as RCS , hereinafter) as a function of range, where the slope is the extinction coefficient. By recording the signal with the lidar pointed along the horizontal path if the condition of horizontal layering is satisfied, every deviation of Eq. 3.3 from Eq. 3.4 is due do to the fact that $\xi(z) \neq 1$. Subtracting Eq. 3.4 from Eq. 3.3 $\xi(z)$ can be found as:

$$\xi(\lambda,z)=\exp\left[\ln\left(z^2P(\lambda,z)\right)-\ln\left(z^2P(\lambda,z)\right)\right] \tag{3.5}$$

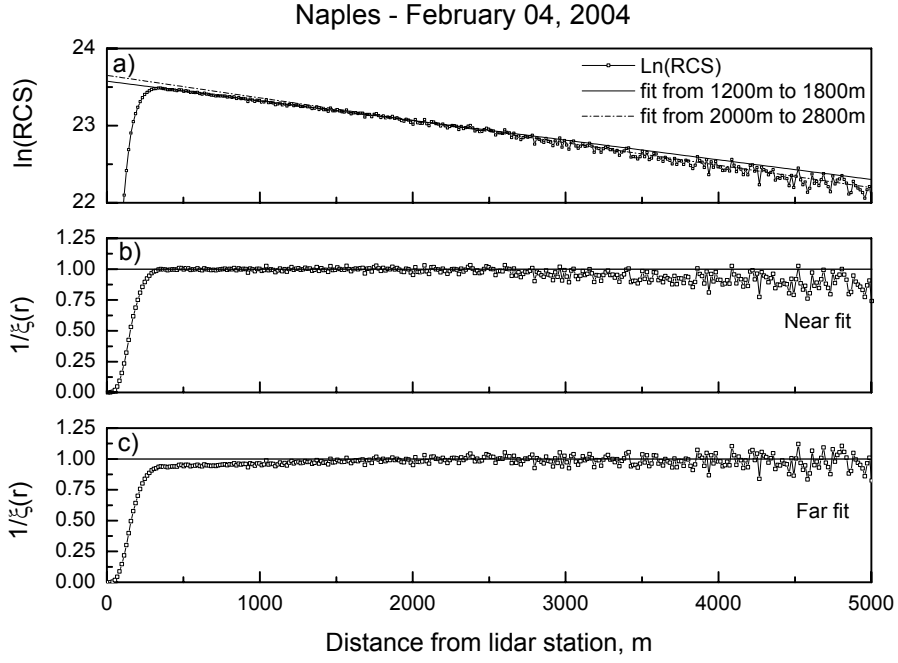

Fig. 3.6 a) Plot of logarithm of RCS is reported with linear regressions obtained fitting experimental data in two different ranges; b) and c) overlap function obtained fitting in the near range (1200-1800 m) and far range (2000-2800 m).

Measurements have showed that in far range RCS suffered of a changing in its slope do to a variation in the extinction coefficient. Such variation can be explained by an imperfect stratification of the atmosphere. Therefore, it is crucial a proper choice of the range for the linear regression (linear regression has be made over a range where the slope of the line given by Eq. 3.4 is supposed to be constant to try to determine the overlap function). If the selected range is too far the RCS can suffer for a change in α_0. Moreover, if the range is taken too close to the lidar, a problem with overlap could not be prevented, even if one could be sure about the hypothesis on atmospheric homogeneity. Fig. 3.6 shows the situation. Data shown have been acquired for the UV elastic channel on 4th February 2004 orienting the lidar horizontally. All performed horizontal measurements present this kind of feature.
In Fig. 3.7 some overlap function profiles obtained with the described method are plotted. An explanation of this feature can be given by considering the orographical complexity of the lidar site in Naples. Actually, Naples is located on an active volcanic field and old crater walls surround the lidar station. In general, the hill system prevents atmospheric horizontal layering leading to a bad evaluation of overlap function with such a method.

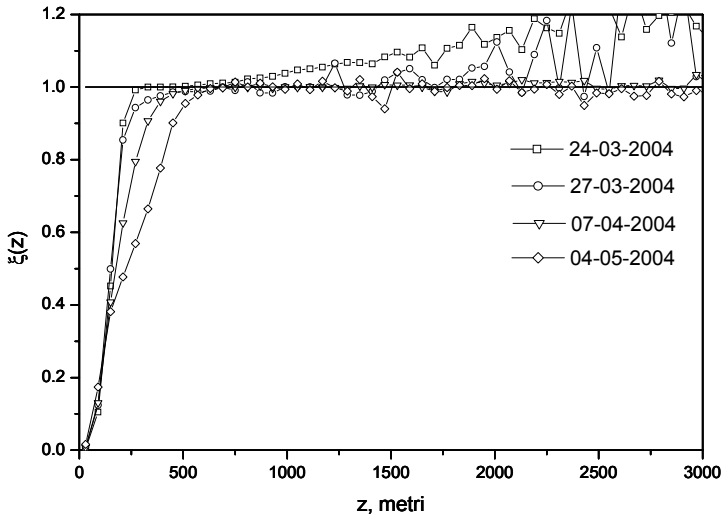

Fig. 3.7. Some examples of the overlap function profile obtained by the described method on different days are plotted. Differences are due to bad atmospheric conditions that prevent result repeatability.

An alternative method to retrieve the overlap function has been proposed by Wandinger [Wandinger, 2002]. This technique is based on the measurement of a pure molecular backscatter signal in addition to the elastic backscatter signal performed with an aerosol Raman lidar. The basic assumption is that the overlap profiles for both the elastic (sub-index L) and the Raman channels (sub-index R) are identical:

$$\xi(\lambda_L, z) = \xi(\lambda_R, z) \tag{3.6}$$

Thus, Eq. 3.2 can be re-written as:

$$P_L(z) = \frac{C_L}{z^2}\left[\beta_p(z) + \beta_m(z)\right]\xi_L(z)\,T_L^2(z) \tag{3.7}$$

for the elastic signal, and:

$$P_R(z) = \frac{C_R}{z^2} \beta_R(z) \xi_R(z) T_R(z) T_L(z) \tag{3.8}$$

for the Raman signal, where $T_L(z)$ is the transmittance at the laser wavelength, while $T_R(z)$ is the transmittance at Raman wavelength. C_L and C_R are the system-constants (independent from z) for the elastic and Raman channels, respectively.
If Eq. 3.6 holds true, the Raman method [Ansmann, 1992] allows to retrieve the aerosol backscattering profile without knowing the overlap function. On the other hand, the Klett [Klett, 1981] solution for the backscatter coefficient needs a right evaluation of the overlap profile. So, deviations between the Raman and Klett solutions provide an evaluation of the overlap function. Such deviation can be expressed as:

$$\frac{\beta_p^{Ram}(z) - \beta_p^{Klett}(z)}{\beta_p^{Ram}(z) + \beta_m(z)} \quad \propto \quad 1 - \xi_L(z) \tag{3.9}$$

which is the relative difference between the aerosol backscatter coefficients obtained with Raman and Klett method. An iterative process is then applied. At the first step (i=0) from the elastic uncorrected signal $\beta_{p,0}^{Klett}(z)$ is retrieved using a fixed extinction to backscatter ratio (called lidar ratio and referred as S, hereinafter; for more information see Chapter 2, Eq. 2.24), and from both elastic and Raman signals $\beta_p^{Ram}(z)$ is retrieved as well. That, $\xi_{L,0}(z)$ is determined as:

$$\Delta\xi_{L,0} = \frac{\beta_p^{Ram}(z) - \beta_{p,1}^{Klett}(z)}{\beta_p^{Ram}(z) + \beta_m(z)} \tag{3.10}$$

Previous expression can be used to correct the elastic signal as:

$$P_{L,i+1}(z) = P_{L,i}(z)\left[1 + \Delta\xi_{L,i}(z)\right] \tag{3.11}$$

If the process is repeated for some steps, $\beta_p^{Klett}(z)$ approaches $\beta_p^{Ram}(z)$. The iteration will be stopped when differences between the two values are negligible. To use this method it shall be stressed that the main hypothesis expressed by Eq. 3.6 must be verified. Moreover, a hypothesis on the lidar ratio is needed when $\beta_{p,i}^{Klett}(z)$ is computed. S is a function of height and it depends from the microphysical properties of the aerosol. In particular, because of the complexity of Naples orography and the proximity of aerosol sources (industrial and agricultures activities, sea and volcanoes), S can vary in a quite large range and a careful statistical evaluation of S have to be done for low heights where the overlap function has to be evaluated.
Moreover, if Eq. 3.6 is not verified, results can be worst. The validity of such hypothesis has been checked by introducing the same interference filter in both the elastic and Raman detection channels. If the overlap function for both channels is the same, they should register the same signal. Fig 3.8 shows the ratio between the recorded elastic signals of the two photomultipliers from near range.

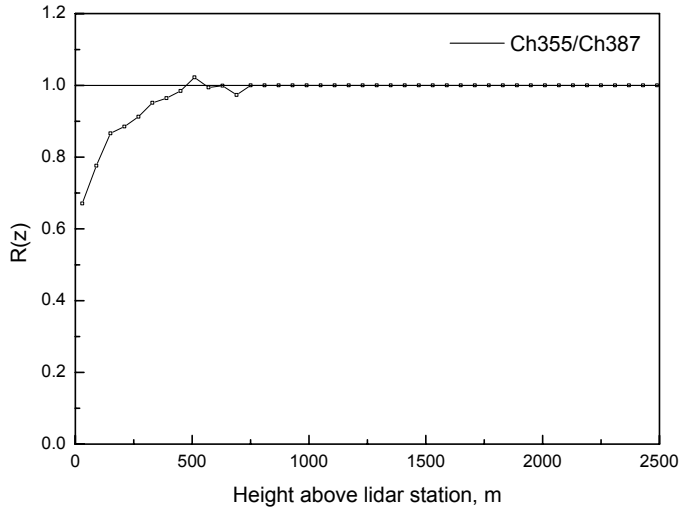

Fig. 3.8. Elastic signal ratio between Raman and elastic channels

It is clear that the two channels look to different atmospheric volumes; in particular the Raman channel seems to enter into the field of view of telescope before the elastic channel. From this measurement a corrective factor can be introduced for overlap function:

$$R(z) \equiv \frac{P_L(z)}{P_R(z)} = \frac{\xi_L(z)}{\xi_R(z)} \tag{3.12}$$

Actually the Eq. 3.12 is an evaluation of overlap functions ratio of the two channels and it has been used to correct the overlap profile of the nitrogen Raman channel knowing that one of the elastic channel. By this method the determined overlap allows to retrieve backscattering profile starting from 100 m, while the first point useful for extinction measurements is situated at 300 m above the lidar station.

3.4. Data Treatment

Before the application of the processing algorithm, some "operations" are applied to the raw data:

- Cloud screening
- Temporal average in order to increase the signal-to-noise ratio (referred as SNR, hereinafter). For climatological measurements (EARLINET regular measurements) the signals are integrated over 30 min.
- Background subtraction. The background for each detection channel is determined by the last 800 bins of the data, corresponding to very high altitudes and then subtracted from data.
- Pile-up correction
- Correction of the incomplete overlap
- Binning, in order to increase the SNR. Actually, this operation reduces the vertical resolution.

For the retrieval of the backscattering coefficient vertical profile, the Klett- Fernald inversion is used for daytime measurements, while the Raman method is applied for night-time measurements. In the first case LR has to be known in order to determine the backscatter coefficient. The choice of the LR is done in two different ways:

- If a “near-in-time” night-time measurement has been performed and the atmosphere can be considered uniform with a rather good approximation, the measured nigh-time value of LR is chosen.
- LR values from a three-year statistical analysis are used.

For special events as Saharan dust, forest fires, volcanic eruption etc., LR values from literature are used.
In both inversion schemes, the backscatter coefficient at a reference altitude has also to be known. To find an appropriate reference altitude and value, a Rayleigh signal is calculated from temperature and pressure profiles of a model and compared to the RCS signal If the slope of both, the calculated and the measured signal, agree over a sufficient range, it is assumed that negligible aerosols are present in this range, and thus the total backscatter coefficient is assumed to be equal to the molecular coefficient (for more details, see Chapter 2).

3.5. Dependence on the molecular signal

In this paragraph, we are interested to analyze the error introduced by the choice of the molecular density profile. Fig. 3.9 shows two different “standard” atmospheric profiles, indicated as “molecular 1” and “molecular 2”. “Molecular 1” is the standard molecular profiles used by EARLINET community, while “molecular 2” is the standard molecular profile used by CALIPSO. The deviation between the two profiles is a function of the height and is shown in Fig. 3.10. Below 12 km the difference between the two standard atmospheric molecular profiles is less than 5 %.
The deviation in the standard atmospheric profiles obviously propagates in the backscatter and in the extinction profiles. To quantify this effect a common lidar profile is analyzed with the Raman inversion scheme using the two different standard atmospheric profiles.
The results are shown in Fig. 3.11 and 3.12 for backscattering and extinction, respectively.
In the backscatter profile the deviation is of the same order of the deviation in the molecular profile (less than 5 % below 10 km), while in the extinction profile the deviation is almost 10 % below 10 km.

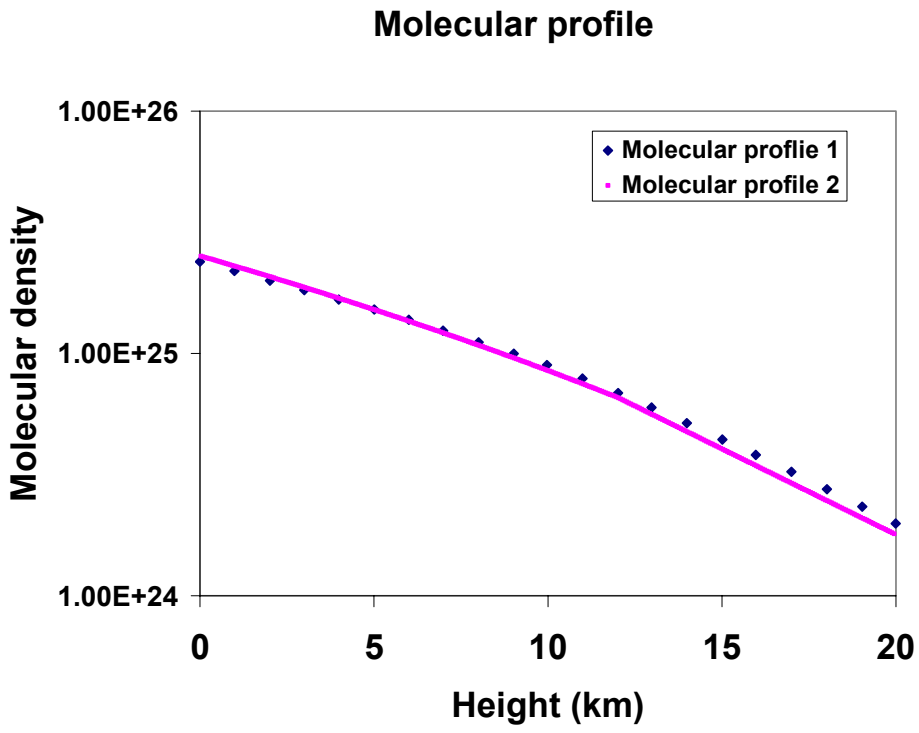

Fig. 3.9. Two standard molecular profiles. "Molecular 1" is the standard molecular profiles used by EARLINET community, while "molecular 2" is the standard molecular profile used by CALIPSO.

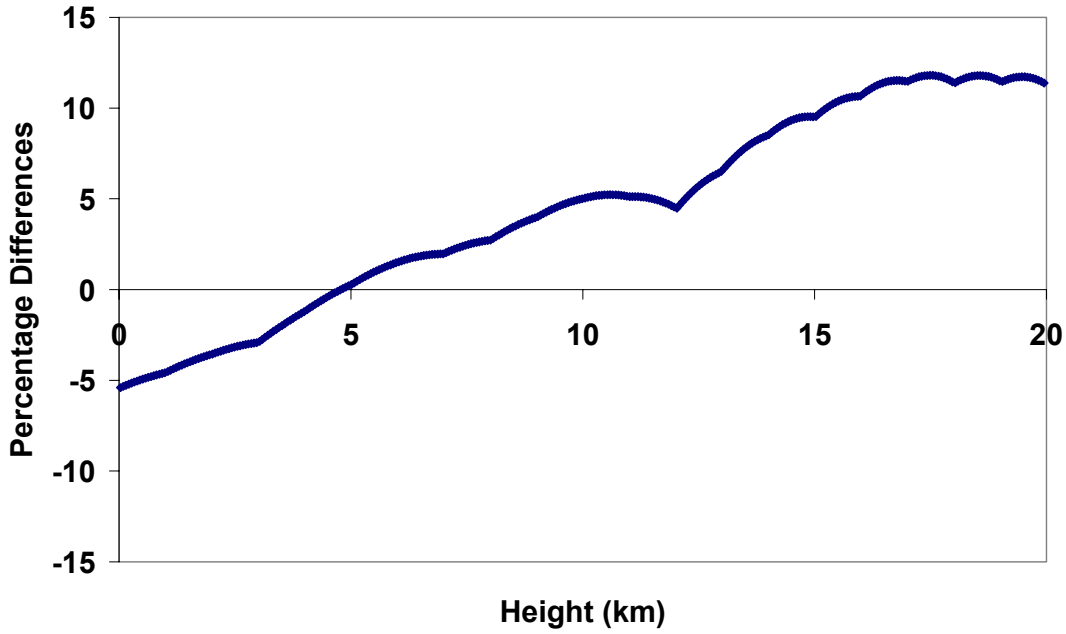

Fig. 3.10. Percentage differences between the two different molecular profiles. The percentage difference is constructed in this way: (Molecular 1 – Molecular 2)/Molecular 1 and then multiplied for 100.

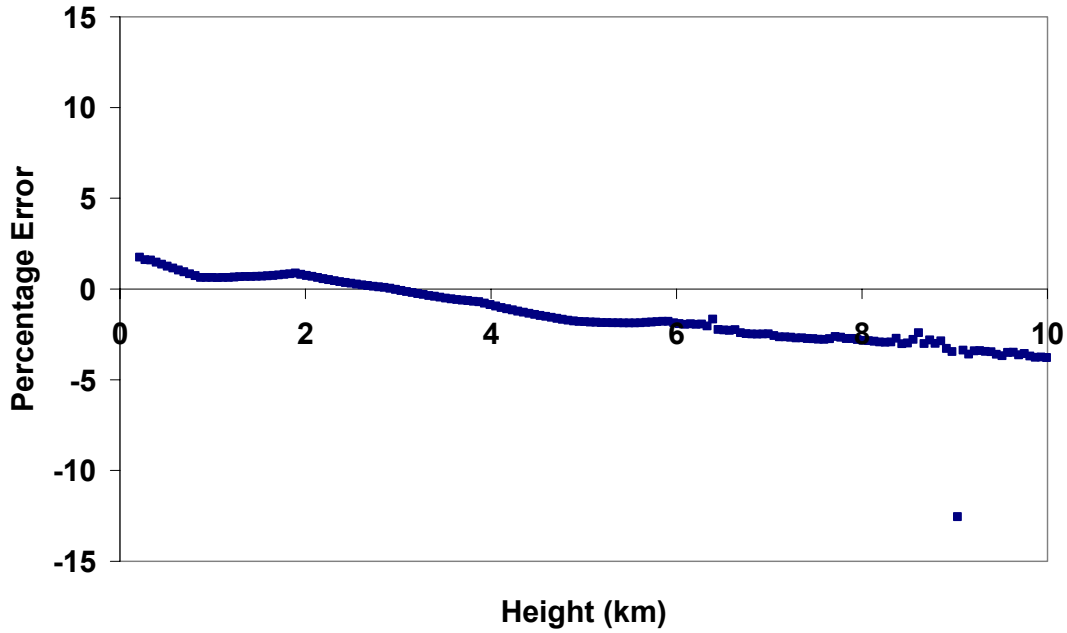

Fig. 3.11. Percentage error on the backscatter profiles using the two different molecular profiles. The percentage difference is constructed in this way: (Backscatter 1 – Backscatter 2)/Backscatter 1 and then multiplied for 100. Backscatter 1 and Backscatter 2 are the backscatter profiles calculated with the Molecular 1 and the Molecular 2 profiles, respectively.

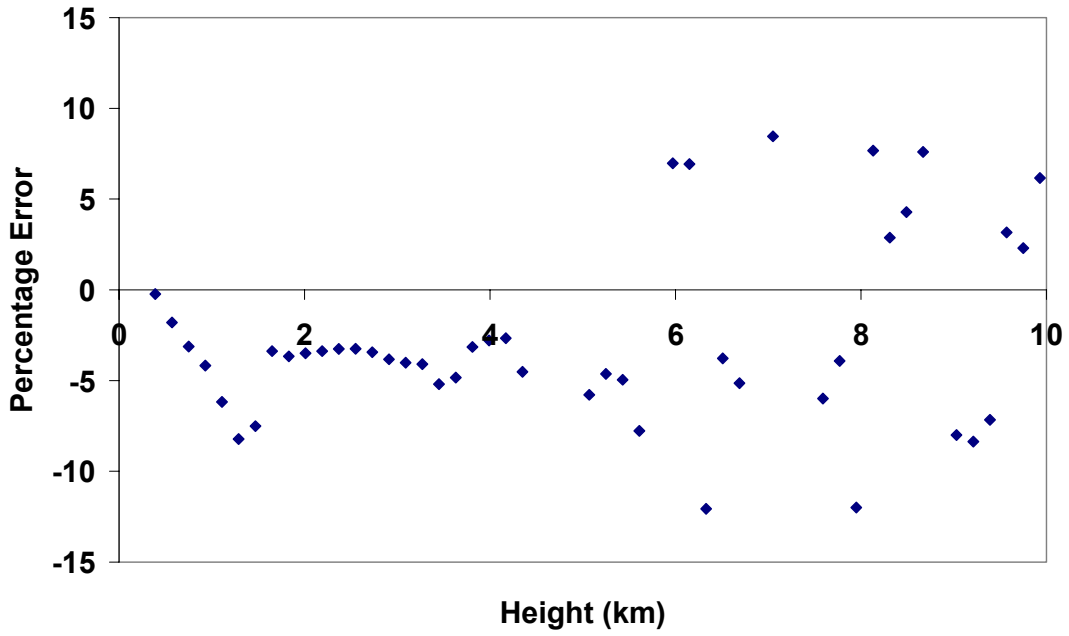

Fig. 3.12. Percentage error on the extinction profiles using the two different molecular profiles. The percentage difference is constructed in this way: (Extinction 1 – Extinction 2)/Extinction 1 and then multiplied for 100. Extinction 1 and Extinction 2 are the extinction profiles calculated with the Molecular 1 and the Molecular 2 profiles, respectively.

3.6. Error analysis

As with any experimental technique, lidar measurements are subject to a number of experimental uncertainties, arising both from the measurement (noise and instrumental error) and from the assumptions or uncertain values that enter into the data analysis. These uncertainties depend on a number of factors, including the laser wavelength and other lidar system parameters, the background radiation, the aerosol concentration, the accuracy, the resolution, and the proximity of the nearest molecular density measurement, the validity of lidar calibration procedures, and the uncertainty of the atmospheric transmission profile at the lidar profile. In general, the total measurement uncertainty depends on these factors in a complicated and often counter-intuitive way. Nevertheless, it is important that quantitative estimates of those uncertainties be derived, both as a means of assigning error bars to lidar derived data products, and as a tool in designing and estimating future lidar systems for improved measurements or different operating conditions.
Systematic errors can be induced by misalignment of either the transmitter or the receiver, inadequate value of the lidar ratio, calculation of the molecular backscatter coefficient and so on. The sources of uncertainties in the estimation of the aerosol backscattering and extinction coefficient are:

- The statistical error due to noise in the signal detection.
- The error introduced by operational procedures such as signal averaging during varying atmospheric extinction and scattering conditions.
- The error associated with the estimation of the molecular backscatter coefficient.
- The error associated with the estimation of the total backscatter coefficient at the reference distance.
- The systematic error associated with the estimation of the lidar ratio, about 20-30% [Godin 1987].

- The systematic error associated with the multiple scattering [Ansmann, 1992; Wandinger 1998; Whiteman 2000].

The sources of uncertainties in the estimate of the aerosol extinction coefficient are:

- The statistical error due to noise in the signal detection.
- The error introduced by operational procedures such as signal averaging during varying atmospheric extinction and scattering conditions.
- The error associated with the estimation of the molecular backscatter coefficient.
- The systematic error associated with the wavelength dependence parameter k [Ansmann, Wandinger et al. 1992; Whiteman 2000]
- The systematic error associated with the multiple-scattering [Ansmann, Wandinger et al. 1992; Wandinger 1998; Whiteman 2000], primarily in presence of clouds

For backscatter coefficient inversion (both Raman and Klett methods) the error on the choice of the reference value must be taken into account.
Because of different distribution of such error types above indicated it is quite difficult to apply an analytical method to evaluating the final errors on the retrieved optical parameters. Therefore, a Monte Carlo procedure has been used because all error sources with different distributions can be included in this method.
Briefly, the evaluation of analog signal errors is made through the evaluation of the standard deviation on the recorded 30 signal profiles (of 1 minute time). Actually, this operation takes into account possible atmospheric fluctuations; for instance, significant variations can be present on the top of the planetary boundary layer during the measurement record because of high turbulence.
For the error coming from the photon counting system, a normal distribution is assumed because of large number of collected photons for each acquisition channel. Defining $p_{k,j}(z_i)$ as the single shot signal at the height z_i, where k is the shot number (k=1,…, 1200 shot/min for the Nd:YAG lidar), j is the j minute number (j=1,…, 30 min, typically), and i is the channel number (i=1,…, 2000 for a dwell time of 10^{-7} sec). Then the total accumulated signal is:

$$P_{tot}(z_i) = \sum_j P_j(z_i) = \sum_j \sum_k p_{k,j}(z_i) \tag{3.13}$$

To retrieve aerosol optical properties, an "effective" lidar signal is calculated. It is defined as a 1 minute accumulated signal from which the background radiation signal has been subtracted (P_j - B_j).
The standard deviation of the total accumulated signal is:

$$\sigma_{1,i} = \sqrt{\sum_j \left[\left(P_j - B_j\right) - \frac{\sum_j \left(P_j - B_j\right)}{30} \right]^2} \tag{3.14}$$

where the background B_j is evaluated in the far range for each of the measured lidar profiles. The Eq. 3.14 for the standard deviation does not include the electrical noise, which is usually synchronized with the laser pulse. Experimentally, the contribution due to the electrical noise is determined by blocking the laser beam before to send it in the atmosphere and by recording the output of the photomultipliers. For the altitude range $[z_1, z_2]$ in which the background is evaluated

and the lidar signal is negligible, the standard deviation of the total accumulated signal can be expressed as:

$$\sigma_2 = \sqrt{\sum_{i=z_1}^{z_2}\left[P_{tot}(z_i) - \frac{\sum_{i=z_1}^{z_2} P_{tot}(z_i)}{z_2 - z_1}\right]^2} \tag{3.15}$$

Now, σ_2 includes both the contribution due to the statistic and the electrical noise. The first contribution (due to the statistic) can be evaluated as:

$$\sigma_3 = \sqrt{\frac{\sum_{i=z_1}^{z_2} P_{tot}(z_i)}{z_2 - z_1}} \tag{3.16}$$

The electrical noise and other instrumental errors are evaluated from high altitude signals (generally, above 20 km) where the signal is only due to the background radiation: any deviation from expected background registered signal is considered as instrumental error. Then, the instrumental error (σ_4) can be evaluated as difference between (3.15) and (3.16), because:

$$\sigma_2^{\,2} = \sigma_3^{\,2} + \sigma_4^2 \tag{3.17}$$

Finally, the error for the effective lidar signal is:

$$\sigma_i = \sqrt{\sigma_1^2 + \sigma_4^{\,2}} \tag{3.18}$$

To compute the errors on the aerosol optical parameters the error propagation should be applied. All the treated error sources are combined together in the Monte Carlo error procedure as follows:

- A number of simulated N_2 Raman signals are generated by extracting each data point from the statistical distribution of the experimental data, which takes in to account signal statistical error, instrumental error and overlap function error. Usually, a number of 50 signals is large enough to get stable results.
- From each of these lidar profiles, extinction and backscattering profiles are determined by applying the above described algorithm. When applying these algorithms the uncertainties on temperature are introduced and the same is done for the uncertainty in the choice of the reference point.

Concerning the backscattering coefficient evaluated with the Raman method, the error is evaluated analytically through the error propagation formula:

$$\sigma_i = \sqrt{\left(\frac{\sigma_{i,P_{\lambda_L}}}{P_{i,\lambda_L}}\right)^2 + \left(\frac{\sigma_{i,P_{\lambda_R}}}{P_{i,\lambda_R}}\right)^2 \left(\beta_{i,p} + \beta_{i,m}\right)} \qquad (3.19)$$

In addiction to the statistical error, systematic errors must also be considered. The contribution from the molecular extinction uncertainties amounts to < 0.01 km^{-1} if the ozone concentration deviates by no more than a factor of 3 from the standard ozone profile and the air density deviates by no more than 5% from the standard atmosphere; this corresponds to errors in the estimated value of temperature (T) and pressure (P) of $\Delta T < 10$ K $\Delta P < 1$ kPa [Ansmann, 1992].

3.7. References

Ansmann, A., M. Riebesell, et al., **Combined Raman Elastic-Backscatter Lidar for Vertical Profiling of Moisture, Aerosol Extinction, Backscatter, and Lidar Ratio**, Applied Physics B-Photophysics and Laser Chemistry **55**(1), 18-28, (1992).

Ansmann, A., M. Riebesell, et al., **Measurement of Atmospheric Aerosol Extinction Profiles with a Raman Lidar,** Optics Letters **15**(13), 746-748, (1990).

Ansmann, A., U. Wandinger, et al., **Independent Measurement of Extinction and Backscatter Profiles in Cirrus Clouds by Using a Combined Raman Elastic-Backscatter Lidar**, Applied Optics **31**(33): 7113-7131, (1992).

CALIPSO webpage, http://www-calipso.larc.nasa.gov/

EAQUATE webpage, http://badc.nerc.ac.uk/data/eaquate/

Klett, J. D., **Stable analytical inversion solution for processing lidar returns**, Applied Optics **20**, 211-220, (1981).

Klett, J. D., **Lidar inversion with variable backscatter/extinction ratios**, Applied Optics **24**(11), 1638-1643, (1985).

Measures, R. M., **Laser Remote Sensing. Fundamentals and Applications**, New-York, Krieger, (1992).

LAUNCH webpage, http://www.dwd.de/en/FundE/Observator/MOL/LAUNCH2.htm

LITE webpage, http://www-lite.larc.nasa.gov/

Pettifer, R. E. W., **Signal induced noise in lidar experiments**, J. Atmos. Terr. Phys. **37**: 669-673, (1975).

Russell, P. B., Swissler, T. J., and McCormick, M. P., **Methodology for error analysis and simulation of lidar aerosol measurements**, Applied Optics **18**(22), 3783-3797, (1979).

Sasano, Y., and Browell, E., V., **Light scattering characteristics of various aerosol types derived from multiple wavelength lidar observations**, Applied Optics **28**(9), 1670-1679, (1989).

Sasano, Y., Browell, E., V., and Ismail S., **Error caused by using a constant extinction/ backscattering ratio in the lidar solution**, Applied Optics **24**(22), 3929-3932, (1985).

Whiteman, D. N., S. H. Melfi, et al., **Raman Lidar System for the Measurement of Water-Vapour and Aerosols in the Earths Atmosphere**, Applied Optics **31**(16), 3068-3082, (1992).

Whiteman, D. N., **Application of statistical methods to the determination of slope in lidar data**, Applied Optics **38**(15), 3360-3369, (1999).

Introduction

Numerical models used for weather prediction are, in general, unable to describe aerosol and cloud microphysics and interaction processes that are crudely parameterized. This leads to significant errors in forecasting initialization of convection, as well as precipitation intensity and distribution.
A large improvement in the description of aerosol and cloud microphysics can be obtained only by measurements In particular, measurements on *local scale* are very important because they provide information, generally parameterized by model.
In this chapter, the Naples - Pontecagnano and the Launch (International **L**indenberg campaign for **A**ssessment of h**U**midity a**N**d **C**loud profiling systems and its impact on **H**igh-resolution modelling) campaigns are presented.
The first campaign (9-10 May 2005) was addressed to the investigation of the differences in the atmospheric parameters for urban and rural sites, with a special attention to the planetary boundary layer (referred as PBL, hereinafter) characterization.
The second campaign (29 August - 31 October 2005) was a long campaign, aimed to the intercomparison of experimental data and model forecast of humidity and cloud profiles at a local scale. In the framework of this campaign, a selected episode has been investigated and analyzed in details.

4.1 The Naples - Pontecagnano field campaign

The Naples – Pontecagnano field campaign was performed in 9-10 May 2005. A diurnal cycle of lidar observations was done in both sites, simultaneously, started from about 16:30 UT of 9th May and ended at about 16:00 UT of 10th May because of rain. The aim of this campaign was to investigate the PBL evolution and to underline the differences of aerosol vertical distribution in urban and rural sites [Frontoso et al., 2006].
The two sites (Naples and Pontecagnano) are located in Southern Italy (70 km apart) and have been chosen because they are different for orography and urbanization level.
Pontecagnano (40° 37' N, 14° 53´ E) is a flat and rural area. Tyrrhenian Sea is 3 Km far from the site-measurement, in the South-West direction. Some hills are located in the North direction. The neighbourhood are agricultural fields.
The city of Naples (40°50'N, 14°11'E) is an urban area characterized by very high aerosol content.
The city is open to the sea in the southern direction and hills on northern and eastern sides on the coast of the Tyrrhenian Sea surround it. A huge industrial area is located in the eastern side of the city. A hilly system surrounds the site of the Naples lidar system. The morphological features of the site and sea breezes regime strongly influence the aerosol distribution and pollutants concentration in the Planetary Boundary layer. [Barone et al., 2000].
In both areas, the development of the breezes and mountain-and-valley-induced winds has important effects in the dispersion of the pollutants emitted.
The orography and the closeness of the sea influence the local circulation phenomena related to diurnal changes in surface temperature and the PBL evolution and affect the aerosol vertical distribution. Moreover, PBL and land-surface processes have critical implications on air quality.
The instrumentation used in this campaign is described in the next sub-paragraph.

4.1.1 Experimental setup

For the description of the lidar instrument operating in Naples see Chapter 3. The only two differences between the current system and the system operating at the time of measurements are:

- the Nitrogen Raman channel at 532 nm was not present at the time of the campaign;
- the 532 nm wavelength was detected through a bi-static configuration of the receiver, thus preventing the lidar sounding at altitudes lower than 2 km .

In Pontecagnano, a portable elastic lidar system was operated by the CO.RI.S.T.A. Consortium (**CO**nsorzio **RI**cerca **S**istemi di **T**elesensori **A**vanzati) [Pica et al., 2003]. It is composed of a

Cassegrain telescope, a Nd:YAG laser and two acquisition channels. The laser source can work at two different wavelenghts, 532 nm and 355 nm, alternatively. The pulse energy is 500 μJ at 532 nm and 300 μJ at 355nm, with a repetition rate of 1 kHz. The telescope diameter is 20 cm with focal length of 1.4 m. The lidar field of view can be changed through a variable aperture from 1.4 to 2.9 mrad. Two detection channels are positioned behind the telescope primary mirror. Two different photomultipliers are used for low and high distance sounding, provided with analog and photon counting acquisition, respectively.
The lidar can perform 3D measurements by scanning the atmosphere along the azimuth and the zenith angles. Thanks to its limited size and its little weight (less than 50 kg), the system can be easily moved for *in situ* measurements.This apparatus has been used for first time during this campaign.

4.2 Planetary Boundary Layer characterization

The planetary boundary layer is the lowest layer of the atmosphere sensitive to the direct effect of the Earth's surface. It controls the flow of heat and momentum between the surface and the free atmosphere, thus playing a key role in atmospheric circulation. The PBL has a thickness quite variable in space and time (from a hundred metres to a few kilometres) and its behaviour is determined by the dynamical and thermal forcing at the surface, synoptic divergence and advection and submittal entrainment. In high-pressure land areas the boundary layer structure evolves during the day, with a well-defined diurnal cycle. A mixed layer is present during the day, while a stable boundary layer with an overlaying residual layer is usually found at night, when convective activity is suppressed. The PBL and land-surface processes have critical implications on air quality [Stull, 1988].
The characterization of the PBL is of theoretical and practical importance with respect to several fields such as weather forecasting, climate change modelling and prediction of pollutant concentration [Seibert et al., 2000]. Since meteorological fields are used as input to air quality models, it is well known that the treatment of the evolution and structure of the PBL in meteorological models has important implications for predicting and understanding the dynamics of ozone (O_3) and other photochemical pollutants [Zhang et al., 2001; Ku et al., 2001; Athanassiadis et al., 2002; Elleman et al., 2003].
Aerosol particles are generally trapped within the PBL and can be used as tracers for studying its vertical structure and time variability. Therefore, aerosol backscattering signals produced by lidar systems can be used to determine the height and the internal structure of the PBL [Seibert et al., 2000, Sicard et al., 2006]. Several methods have been applied to estimate PBL height in case of both stable and the residual layer from lidar signals [Melfi et al., 1985; Boers et al., 1988, Hooper et al,. 1986, Hayden et al., 1997, Flamant et al., 1997].
The coupling between the PBL and the land surface is widely recognized as a crucial component of regional, continental and global-scale numerical models [Patton et al., 2004]. In fact, in order to accurately predict climate and climate change it is therefore necessary to realistically calculate the land surface – atmosphere exchanges in global climate models [Molod et al., 2003]. These calculations are further complicated by the fact that the character of the land surface is highly variable, due, for example, to the variability of vegetation cover, the types of terrain, soil texture and wetness, the amount of cloud cover and precipitation, and the extent of urban areas. These heterogeneities will determine in part the impact on climate of land use changes such as deforestation, urbanization, and desertification. The scale of these heterogeneities may be smaller, and in some cases much more so, than the characteristic grid scale in most current general circulation models (GCMs) used in climate studies.
The complexity of phenomena occurring within the PBL and the influence of advective phenomena and local accumulation processes in many cases prevent unambiguous determination of the PBL height from lidar signals, especially when internal stratification of aerosol is present.

In the present analysis we adopted the method based on the first order derivative of Range Corrected Signal (RCS) [Hayden et al,. 1997, Flamant et al, 1997], this is also the method currently adopted within the EARLINET network [Bösenberg et al., 2001, Matthias et al., 2004].
Using aerosols as tracers, the lidar technique has been applied in order to follow the evolution of the PBL in Naples and in Pontecagnano during a complete diurnal cycle.
Fig. 4.1 shows the temporal evolution of the PBL height in both sites. This graph suggests the following considerations:

- The PBL height is systematically lower in urban than in rural sites of about one hundred meters [COST-715, 2001];
- The decrease of the PBL height in the nocturnal hours seems to be more regular for rural than for urban sites. In fact, the PBL structure is more complex over urban areas than rural ones, as it consists of canopy and roughness sub-layers not found within typical rural atmospheric surface layers.

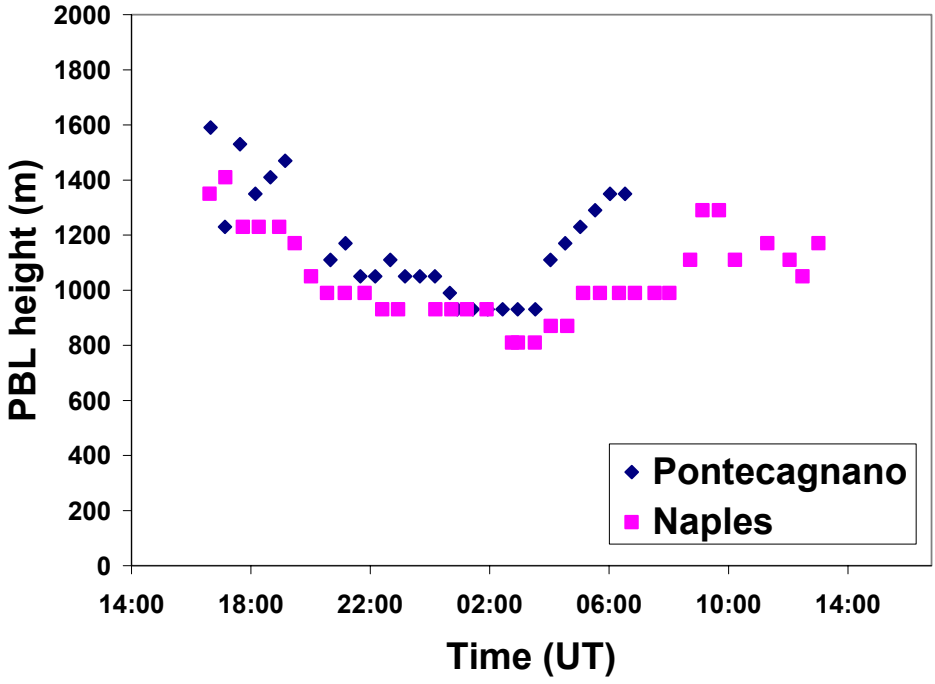

Fig. 4.1 PBL height temporal evolution in Naples (pink square) and in Pontecagnano (blue square).

Moreover, in both sites, also the ground temperature (referred as T_g, hereinafter) has been measured as a function of the time. The temporal evolution of these two parameters permits to calculate their correlation factor (referred as ρ, hereinafter) as a function of their relative temporal delay (referred as Δt). In particular, it is interesting to investigate how the PBL height (H) changes with respect to the ground temperature and if there are some influence of the soil usage. Fig. 4.2 shows the correlation factor ρ between H and T_g as a function of their temporal delay Δt for the two sites.

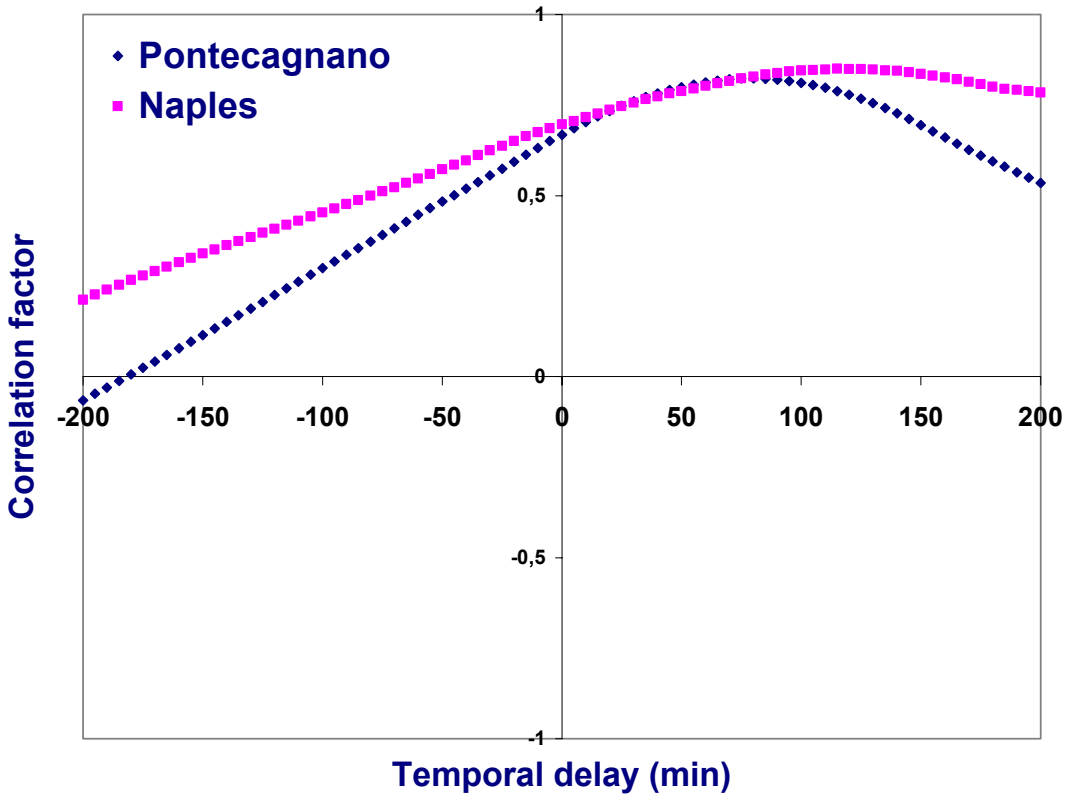

Fig. 4.2 Correlation factor between the PBL height and the ground temperature as a function of the temporal delay in Naples (pink squares) and in Pontecagnano (blue squares).

The correlation factor ρ has been calculated as:

$$\rho(H,T_g)=\frac{\sum\left(H-\overline{H}\right)\left(T_g-\overline{T_g}\right)}{\sqrt{\sum\left(H-\overline{H}\right)^2\sum\left(T_g-\overline{T_g}\right)^2}} \qquad (4.1)$$

where $\overline{H}$ and $\overline{T_g}$ are the averaged PBL height and the averaged ground temperature, respectively. Δt has been calculated as $t_H - t_T$, where t_H and t_T are the time which correspond the observation of H and T_g, respectively. The maximum value of ρ is almost similar for Naples and Pontecagnano (ρ_N = 0.85; ρ_P = 0.82) and correspond to a Δt of 115 minutes and 80 minutes for Naples and Pontecagnano, respectively. These results could be assimilated into regional and global models in order to improve land surface interactions via soil-vegetation atmosphere-transfer (SVAT) schemes.

4.3 Horizontal transport

Lidar measurements have been performed starting at 16:37 UTC of 9th May both in Naples and in Pontecagnano. Fig. 4.3 shows the temporal and spatial evolution of the backscatter profile (referred as β, hereinafter) in Pontecagnano (at λ=532 nm) and in Naples (at λ=355 nm) during a period of about 24 hours.

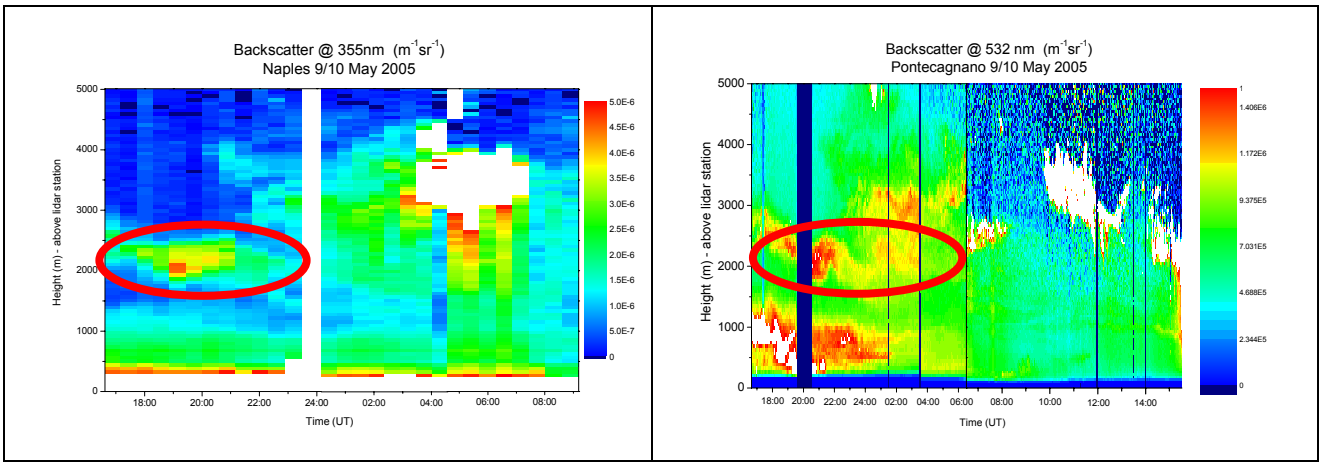

Fig. 4.3 Temporal and spatial evolution of the backscatter coefficient at 532 nm in Pontecagnano (on the left) and at 355 nm in Naples (on the right). The red circle indicates a layer observed in both sites.

Vertical profiles of the backscatter coefficient have been obtained in Naples by applying the Raman algorithm [Ansmann et al., 1992] while in Pontecagnano the Klett-Fernald [Klett, 1991] algorithm is applied because only the elastic signal was available.
In both sites, since the beginning of measurements an aerosol layer (referred as L_A, hereinafter) above the PBL between 1500 and 3000 m is observed (see the red circles in Fig. 4.3).
Fig. 4.4 shows the height of the centre of mass of L_A as a function of the time in Naples and in Pontecagnano. A similar behaviour is observed in Naples and in Pontecagnano with a shift in time of about 90 minutes. This shift is in a rather good agreement with the wind speed (55 km/h) and direction (West – North/West) at that height, as measured by radiosonde at Pratica di Mare (at about 200 km from Naples).

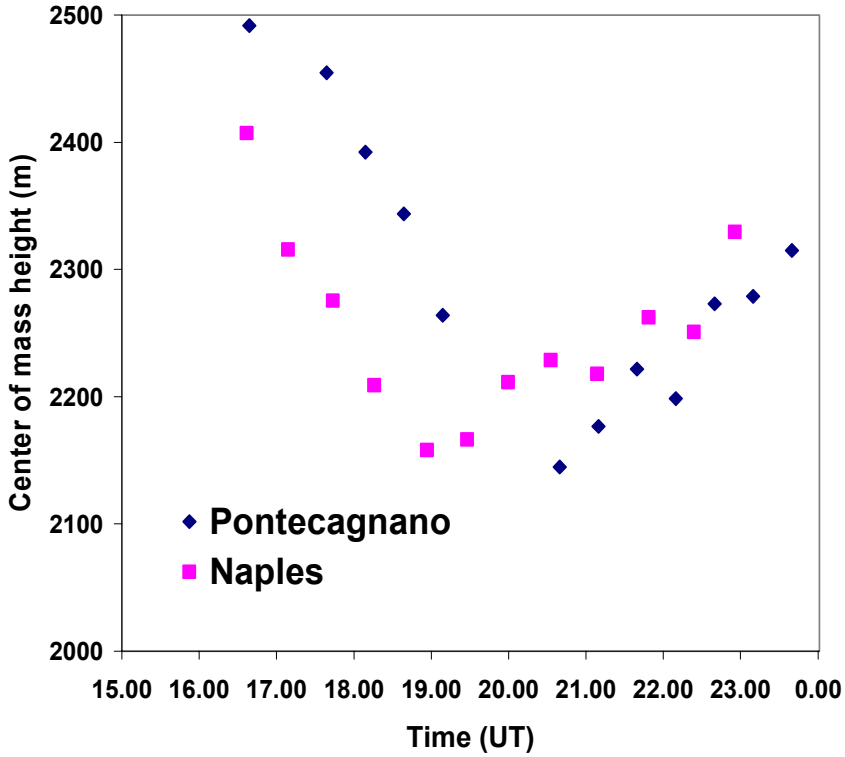

Fig. 4.4 Temporal evolution of the height of the center of mass of the layer in Naples (pink squares) and in Pontecagnano (blue squares).

In order to identify the potential source regions of L_A, analytical backtrajectories have been calculated. The atmospheric trajectories model FLEXTRA [FLEXTRA website] has been used. Fig. 4.5 shows the backtrajectories of L_A which indicate that the origin of L_A is Atlantic.

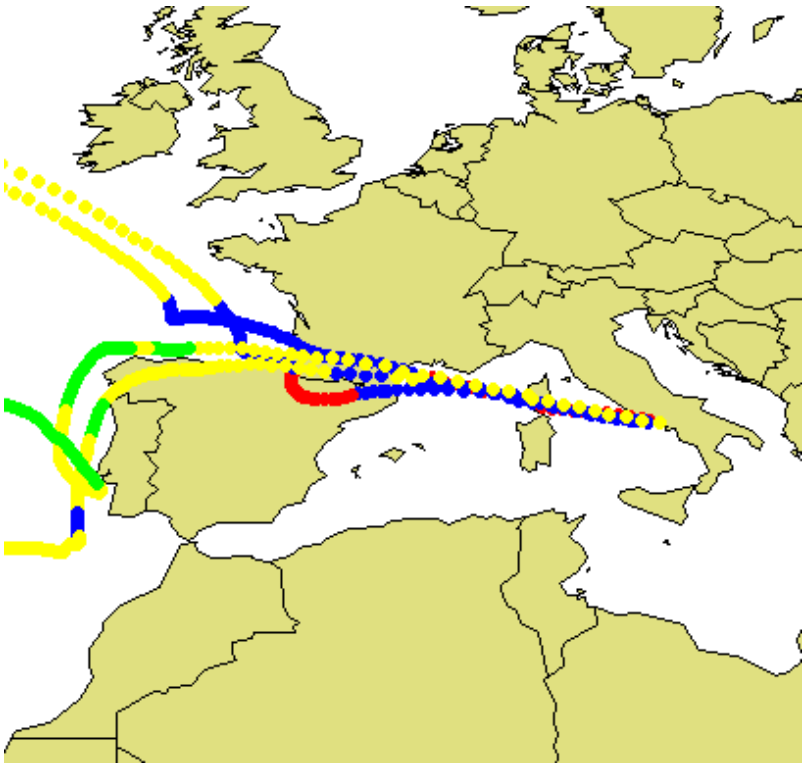

Fig. 4.5 Backtrajectories calculated by FLEXTRA model. These backtrajectories are related to 18:00 UT of 9th May and the different colours are related to different heights. In particular, the colour red means air masses comes from 839.1 and 1930.6 m; the colour blue from 1930.6 and 3115.9 m; the colour yellow from 3115.9 and 4218.1 m; the colour green from 4218.1 and 5977.4 m.

4.4 The Launch campaign

Within the frame of the European Research Action COST-720, "Integrated Ground-based Remote-Sensing Stations for Atmospheric Profiling", and in connection with the WMO GEWEX Working Group on Cloud and Aerosol Profiling "GEWEX CAP" the Richard Aßmann Observatory of the German Meteorological Service DWD, in Lindenberg (Germany) had organized the Launch campaign (International **L**indenberg campaign for **A**ssessment of h**U**midity a**N**d **C**loud profiling systems and its impact on **H**igh-resolution modelling), run from August 29 until October 31 2005. This campaign has been designed to accomplish four major scientific objectives:

- Assessment of new or improved humidity, temperature, and wind profiling systems (Water vapour Lidar systems, Doppler wind Lidar vs Wind Profile Radar (WPR), inter-comparison of different types of Meteorologist Weather Processor (MWP) systems, Fourier Transform InfraRed (FTIR) spectrometer, High-range ceilometer);
- Assessment of various algorithms, combining different techniques for profiling of cloud parameters (integrated profiling);
- Provision of a data set, designed for validation and comparisons between measurements and numerical weather prediction (NWP) output;
- Provision of a data set by using 3D-/4D-VAR data assimilation for high-resolution WV (water vapour)-profiling systems in regional NWP modelling.

In the framework of Launch campaign, several measurements have been performed by the Naples lidar station, according with the IOP (**I**ntensive **O**perational **P**eriod) schedule. The IOP 4 episode (1-3 October 2005) has been selected and investigated [Frontoso, 2007] with a special attention to the variability of water vapour mixing ratio vertical distribution to better understand the associated circulation in the coastal waters of the Gulf of Naples (Tyrrhenian Sea).

This case was characterized by the presence of a cold air intrusion from NNE (North – North East) – Cyclogenesis over the Tyrrhenian Sea started on the late afternoon of 30th September and moving south-eastward. The cold and dry tongue was entering from north in the eastern side of the center of Italy, and was moving quickly south-eastward. The cold air intrusion was driven by a deep surface low located over Greece associated to an upper level cut-off low, as Fig. 4.6 shows. The deep low is advecting cold and dry air from north, as the low rh (relative humidity) tongue crossing the centre Italy indicates, at 18:00 UTC 1st October.
The case was associated with a tropopause folding event and the subsequent beginning of perturbed weather conditions that leaded to the development of clouds and heavy precipitations. Tropopause folds are the dominant and most efficient mechanism of stratosphere-troposphere exchange (STE) in the middle latitudes.

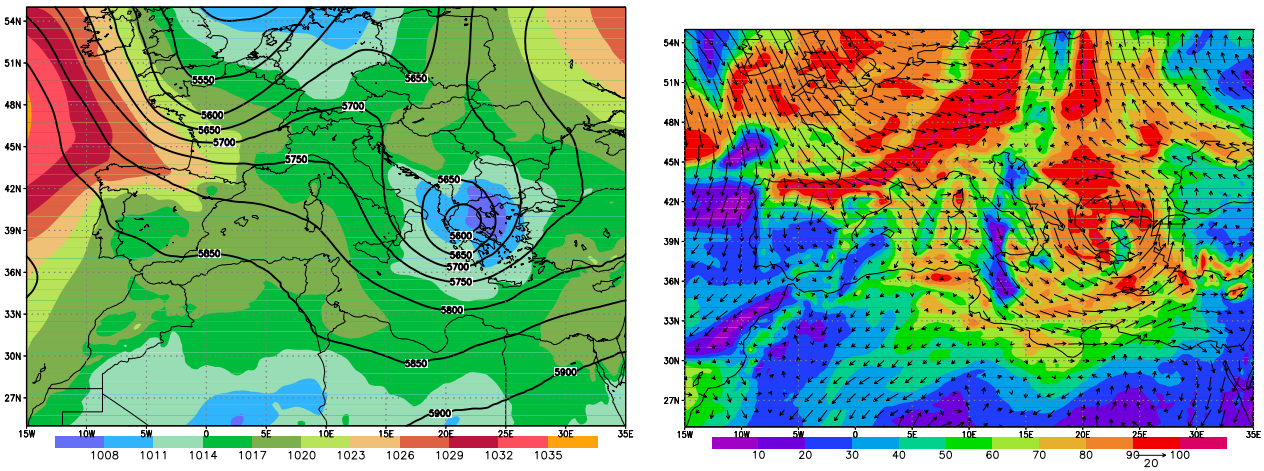

Fig. 4.6 The geopotential map at sea level and at 500 hPa on the 1st October at 18:00 UTC (on the left); the relative humidity and the wind map at 850 hPa on the 1st October at 18:00 UTC (on the right). The figures are based on the ECMWF data analyses at 0.25°.

4.5 MM5 model

A simulation is performed using MM5 (version 3) model from PSU/NCAR [Grell et al., 1994; Dudhia et al., 1993] for this study. The model data used derive from an operative run performed by CETEMPS [CETEMPS website], University of l'Aquila, of the MM5 model (version 3), developed by the Pennsylvania State University and National Center for Atmospheric Research. The MM5 is a non-hydrostatic, terrain-following sigma-coordinate model, designed to simulate or predict mesoscale and regional-scale atmospheric circulation. The model has multiple-nesting capabilities to enhance the resolution over the area of interest: the configuration is chosen to improve the forecast over central Italy using 3 domains two way-nested. The mother domain has a grid size of 27 km and it is centred over the Mediterranean region.
A schematic diagram of the MM5 model structure is shown in Fig. 4.7. Terrestrial and isobaric meteorological data are horizontally interpolated (programs TERRAIN and REGRID) from a latitude-longitude mesh to a variable high-resolution domain on either a Mercator, Lambert conformal, or polar stereographic projection. Since the interpolation does not provide mesoscale detail, the interpolated data may be enhanced (program RAWINS or little_r) with observations from the standard network of surface and rawinsonde stations using either a successive-scan Cressman technique or multiquadric scheme. Program INTERPF performs the vertical interpolation from pressure levels to the sigma coordinate system of MM5. Sigma surfaces near the ground closely follow the terrain, and the higher-level sigma surfaces tend to approximate isobaric surfaces.

Since MM5 is a regional model, it requires an initial condition as well as lateral boundary condition to run. To produce lateral boundary condition for a model run, one needs gridded data to cover the entire time period that the model is integrating.
The grid resolution of domain 2 is 9 km, and the one of domain 3 is 3 km. The model configuration is basically the one used at CETEMPS: the MRF planetary boundary layer parameterization [Troen et al., 1996] is used; an explicit moisture scheme for all domains is associated to the cumulus convection parameterization [Kain et al., 1993] for D1 and D2 only. In addition, 29 unequally spaced vertical sigma levels (1.00, 0.999, 0.995, 0.99, 0.98, 0.97, 0.96, 0.95, 0.94, 0.93, 0.92, 0.9, 0.85, 0.80, 0.75, 0.70, 0.65, 0.60, 0.55, 0.50, 0.45, 0.40, 0.35, 0.30, 0.25, 0.20, 0.15, 0.10, 0.05 and 0.00) are used.
The MM5 is initialized with analysis from the European Center for Medium-range Weather Forecast (ECMWF).

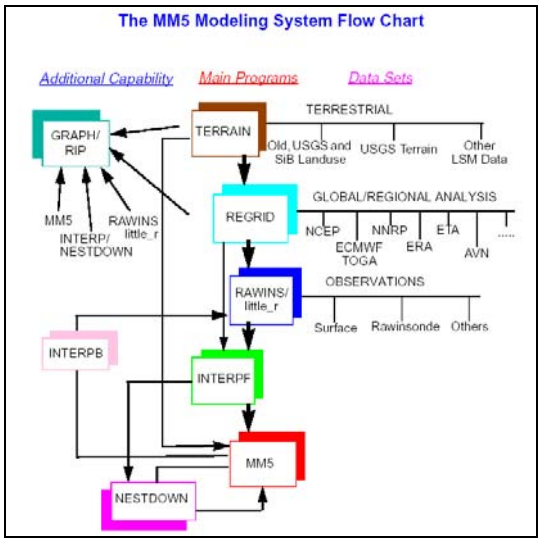

Fig. 4.7 Schematic diagram of the MM5 model (from http://www.mmm.ucar.edu/mm5/)

4.6 Water vapour characterization

Water vapour is involved in an important climate feedback loop. As the temperature of the Earth's surface and the atmosphere increases, the atmosphere is able to hold more water vapour. The additional water vapour absorbs energy that would otherwise escape to space and so causes further warming. The basic picture is then complicated by important interactions between water vapour, clouds, atmospheric motion, and radiation from both the Sun and the Earth. In fact, though the basic operation of the hydrological cycle is well known, there are some important aspects of the role of water vapour as a greenhouse gas that are not well understood, mainly because we lack the necessary observations to test theoretical models. Monitoring long-term changes in water vapour, which are closely linked to climate variations and trends, is needed to both predict and detect changes. Experimental observations are therefore extremely important in order to improve the understanding of water vapour in the climate systems.
At present there are still some theoretical issues to solve. For example:

- Improved understanding of the role of water vapour in influencing the radiation budget of the Earth;
- Improved understanding of the processes determining the distribution of water vapour and its changes over time, including cloud processes and water vapour transport.
- Improvements in the treatments of processes involving water vapour in climate models;
- Improvements in the methods of testing the validity of climate models, particularly their simulation of atmospheric water vapour and related aspects of the hydrological cycle.

It is generally agreed that improved knowledge of the role of water vapour in the climate system hinges largely on closing observational gaps that currently exist.
The remote sensing Raman lidar is a well-established technique for measuring the water vapour and has the great advantage to provide high-quality data with high vertical and temporal resolution. Therefore, the availability of Lidar data will allow for verifying how well the mesoscale models reproduce water vapour content, one of the most important ingredients for the precipitation forecast. Moreover, the model validation would allow to use the model output as first approximation of climatological data in locations where instruments are not present.
The water vapour field is typically characterized by a large space and time variability, in particular in the PBL where local source and sinks of water vapour are located. Water vapour can also influence precipitation occurrences and aerosol properties and cloud formation. Within these general features, the water vapour variability changes day by day depending on the particular meteorological conditions. The water vapour mixing ratio is defined as the ratio of the mass of water vapour divided by the mass of dry air in a given volume (for more information, see Chapter 2, Eq. 2.30)

During IOP 4, measurements started at 17:07 UT of the 1st of October and ended at the 04:41 UT of the 2nd of October because of the rain.

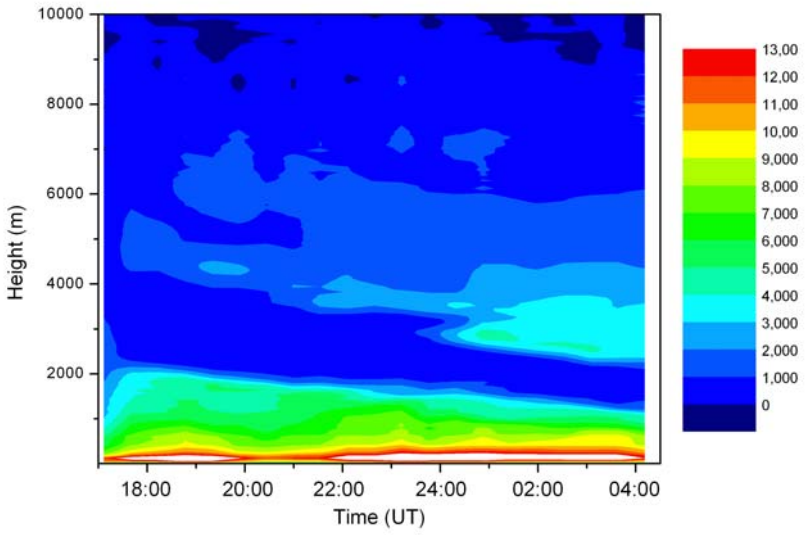

Fig. 4.8 Temporal evolution of water vapour mixing ratio vertical profile measured at Naples lidar station during IOP 4 (1-2 October 2005). The temporal resolution is 30 minutes.

Fig. 4.8 shows the temporal evolution of the water vapour mixing ratio vertical profile measured by the CNISM-Naples lidar station during IOP4. The water vapour field appeared to be characterized by rather a temporal homogeneity until 00:00 UT and a fast spatial variability with no significantly vertical mixing. The cold air intrusion is clearly visible by the blue signature between 2000 and 4000 m where the mixing ratio water vapour assumes values lower than 2g/kg.

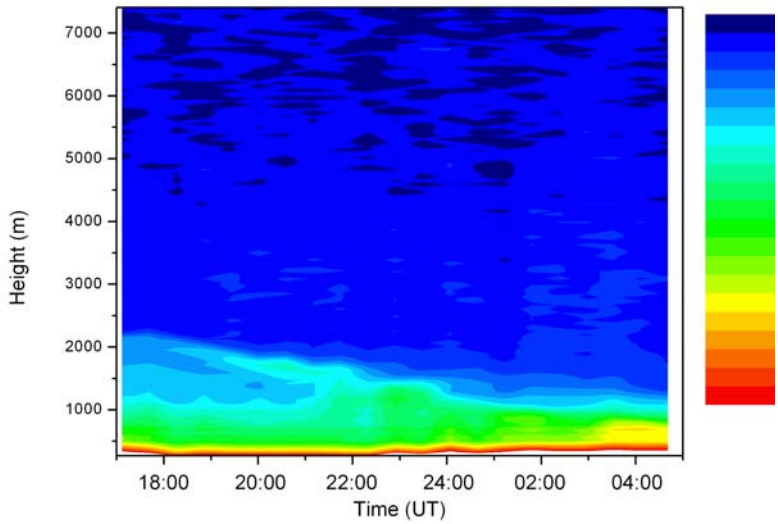

Fig. 4.9 Temporal evolution of the backscatter coefficient vertical profile at 355 nm measured at Naples lidar station during IOP 4 (1-2 October 2005). The temporal resolution is 30 minutes.

Also backscatter profiles at 355 nm have been retrieved by lidar measurements. Fig. 4.9 shows the temporal and the spatial evolution of the backscatter coefficient at 355 nm retrieved by Raman lidar measurements. The presence of the cold air intrusion is clearly evident also in the backscatter coefficient. In particular, since 18:00 UTC, the cold air intrusion cleans up the aerosol above 2000 m; in fact the value of the backscatter coefficient is less than 3×10^{-7} $m^{-1}sr^{-1}$. Figs. 4.8 and 4.9 show a strong correlation before 00:00 UTC until the development of a pure water layer between 2500 and 4000 m that is not associated to aerosol content.

Lidar water vapour profiles have been also compared with forecasts from the MM5 mesoscale model. Comparisons in terms of water vapour mixing ratio reveal the capability of the model to forecast the deep penetration in the troposphere of the dry intruded layer.

Fig. 4.10 shows the comparison between modelled and measured mixing ratio water vapour profiles based on one-hour water vapour profiles. Lidar profiles have been interpolated at the same heights of the model output. The use of water vapour profiles to trace air intrusion allowed to clearly identify a water-layer descending down until to about 3 km.

The agreement between modelled and experimental data is rather good; all the modelled and the lidar profiles are able to capture the sharp decrease of the water vapour mixing ratio at about 2000 m and the water-layer between 3000 and 8000 m. The disagreement below 1000 m is due to the limited ability of the model to reproduce phenomena in the local spatial scale and to the imperfect knowledge of the overlap function of the lidar system. However, the difference between the modelled and the measured profiles can be quantified as about 4 g/kg below 1000 m and 0.5 g/kg above 1000 m.

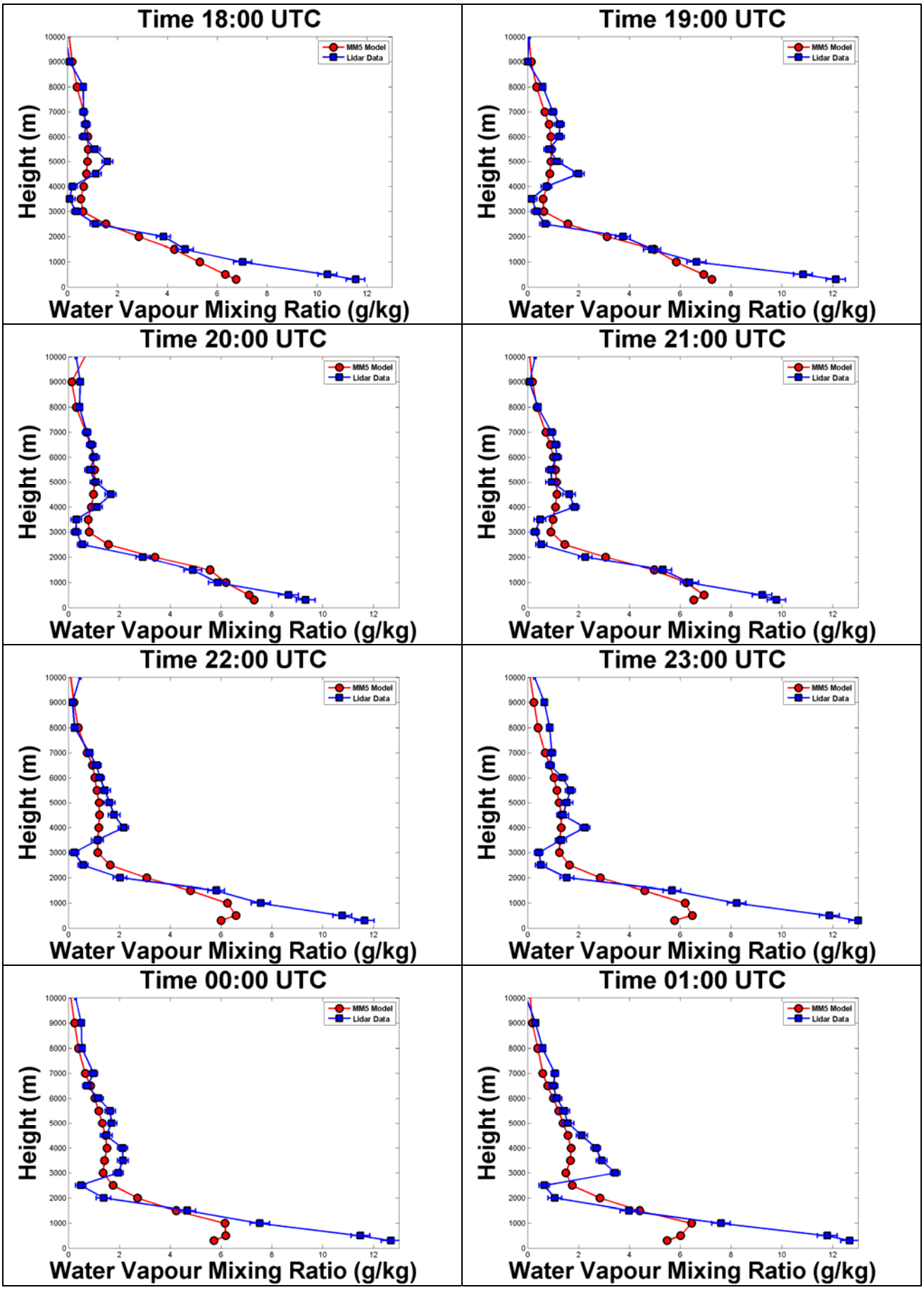
Time 18:00 UTC
Time 19:00 UTC
Time 20:00 UTC
Time 21:00 UTC
Time 22:00 UTC
Time 23:00 UTC
Time 00:00 UTC
Time 01:00 UTC
MM5 Model
Lidar Data
Height (m)
Water Vapour Mixing Ratio (g/kg)

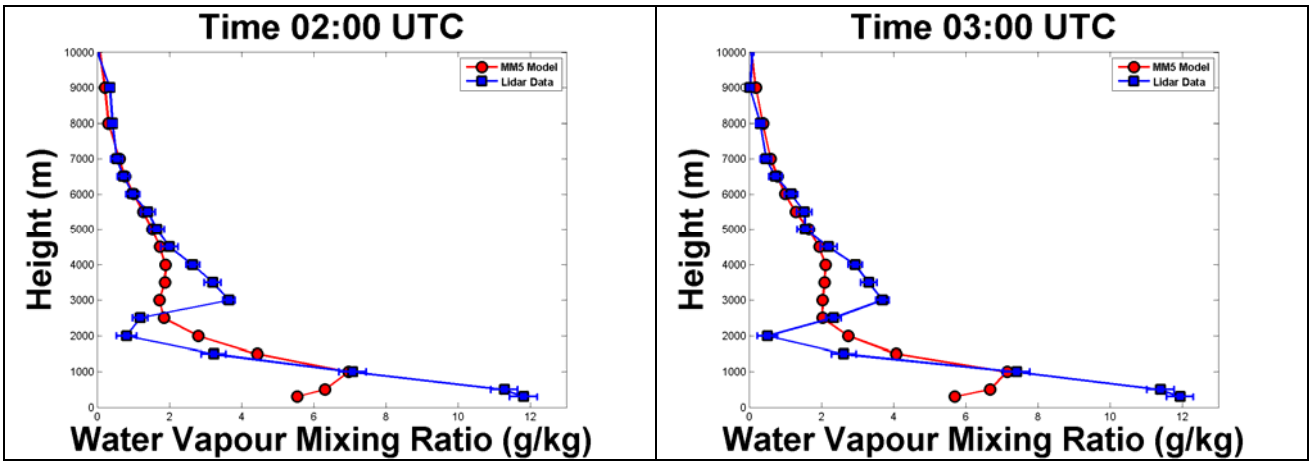

Fig. 4.10 Modelled (red circles) and measured (blue squares) water vapour mixing ratio vertical profiles between 18:00 UTC and 03:00 UTC of the days 01-02 October 2005. The time resolution is one hour.

An estimation of the correlation factor (ρ) between the modelled and the measured water vapour mixing ratio vertical profiles for each hourly profile has been performed. Fig. 4.11 shows the correlation factor as function of the time: ρ is rather high (between 0.9 and 0.8) and slightly decreases with time; this effect might be related to the prediction skills of the model which decreases when departing from initial conditions.

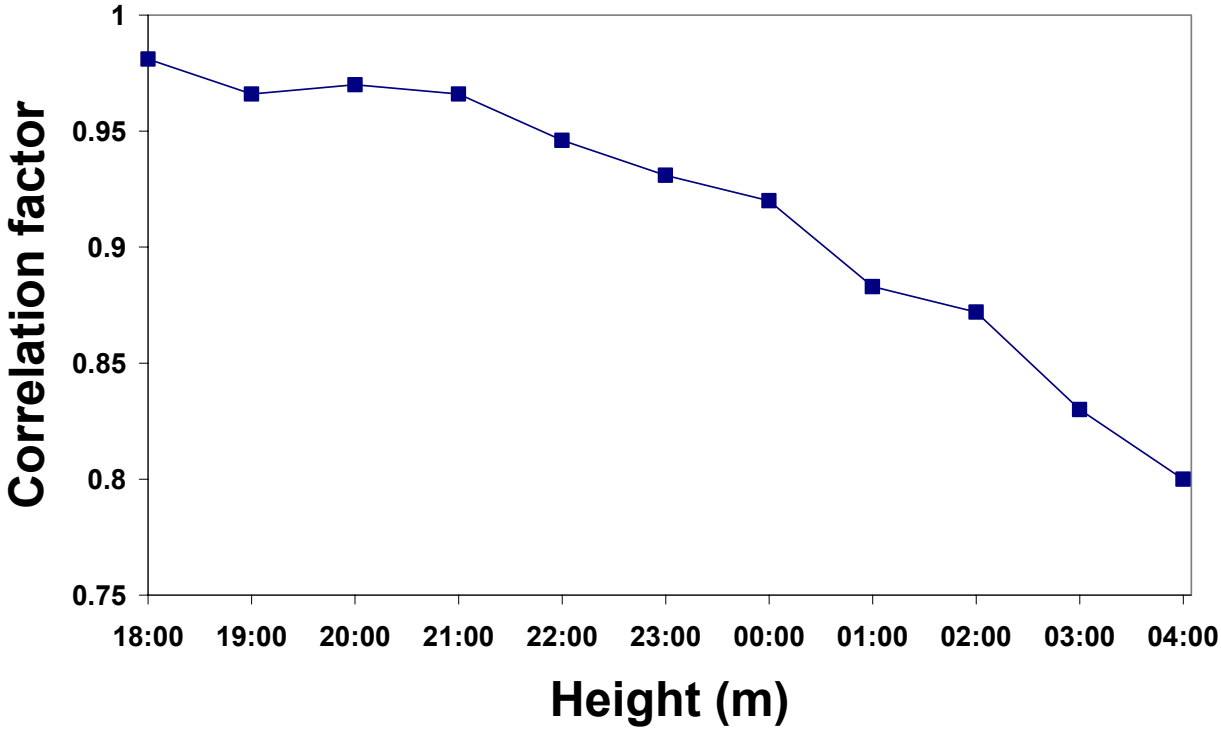

Fig. 4.11 The correlation factor between the modelled and the measured water vapour mixing ratio vertical profiles as a function of the time.

Being located near the sea, the city of Naples is characterized by the land and the sea breeze phenomena. During the IOP 4 the land and sea breeze phenomena are clearly evident by looking at the time evolution of the wind direction measured by sondes at Naples lidar station, shown in Fig.

4.12 In particular, during the late night and the early morning the wind direction is about 50° clockwise from the North and comes from the land (land breeze), while during the day the wind direction is about 200° clockwise from the North and comes from the sea (sea breeze).
Fig. 4.12 also reveals the comparison between the modelled and measured wind direction; the agreement between experimental data and the MM5 model output is very good.

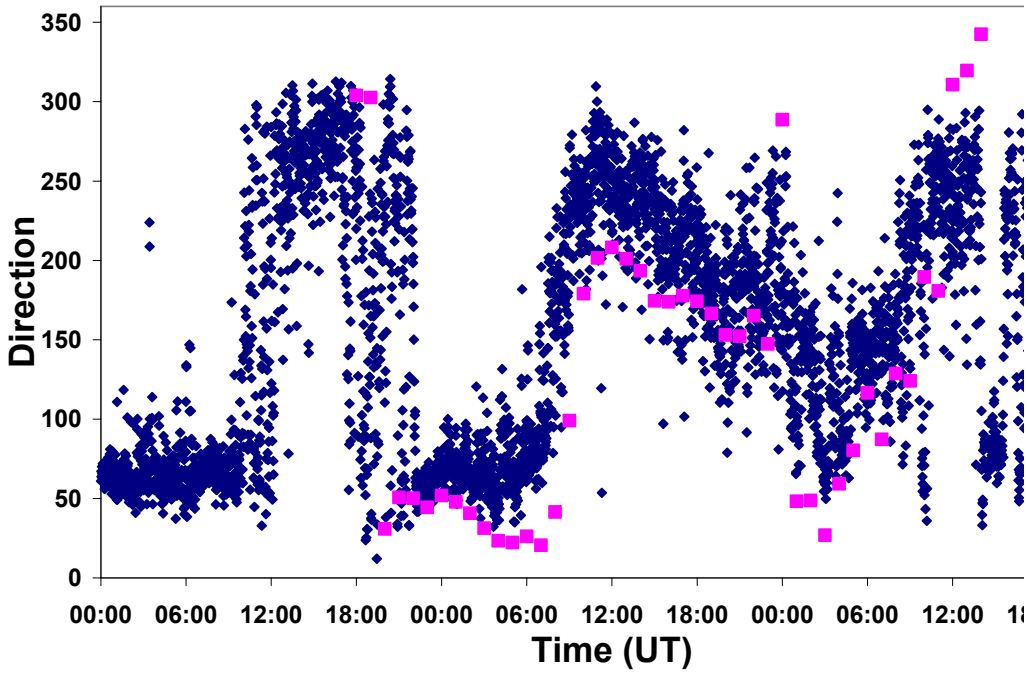

Fig. 4.12 The temporal evolution of the wind direction measured by sondes at the Naples station (blue squares) and retrieved by the MM5 model (pink squares).

4.7 Conclusion

Two field campaigns have been performed and the measurements have been analyzed in order to study atmospheric physical parameters on local scale. Measurements on local scale are very important because they give detailed information, generally parameterized by models.
Using aerosol as tracers, it is possible to determine the temporal evolution of the PBL height. In the framework of the Naples - Pontecagnano campaign (urban and rural sites, respectively), the correlation between the PBL height and the ground temperature as function of their temporal delay has been investigated.
In the framework of the Launch campaign, the water vapour distribution in the area of Naples has been investigated. Though a rather good agreement between observation and model simulation is found, measurements give more detailed information thanks to their high spatial and temporal resolution.
Moreover, in addiction to the fact that measurements give more detailed information than models, measurements can help in improving models and also can be assimilated into them.

4.9 References

Ansmann A., U. Wandinger, **Combined Raman Elastic Backscatter LIDAR for vertical profiling of moisture, aerosol extinction, backscatter and lidar ratio**, Appl. Phys.B, 55, 18-28, (1992).

Ansmann A, Riebesell M, Weitkamp C., **Measurement of atmospheric aerosol extinction profiles with a Raman lidar**, *Opt. Lett.* **15**, 746-748, (1990).

Ansmann A, Wandinger U, Riebesell M, Wietkamp C, Michaelis W., **Independent measurements of extinction and backscatter profiles in cirrus clouds by using a combined Raman elastic-backscatter LIDAR,** *Appl. Opt*. **31** (33), (1992).

Barone, G, D'Ambra P, Di Serafino D, Giunta G, Murli A, Riccio A., **Application of a parallel photochemical air quality model to Campania region (Southern Italy),** *Environmental Modeling & Software* **15**, 503-511, (2000).

Cahen et al., **Lidar monitoring of the water vapour cycle in the atmosphere**, Journal of Applied Meteorology, vol. 21 pp. 1506-1515, (1982).

CETEMPS, http://cetemps.aquila.infn.it.

COST-715, 2001, **Surface energy balance in urban areas**, Extended abstracts of an Expert Meeting, WG-2 COST Action 715, Antwerp, Belgium, 12 April 2000.

Dudhia, **A non hydrostatic version of the Penn State – NCAR Mesoscale Model: Validation test and simulation of an Atlantic cyclone and cold front,** Mon. Wea. Rev., vol. 121, 1493-1513, (1993).

England et al., **Atmospheric water vapour measurements: Comparison of microwave radiometry and lidar**, J. Geophys. Res., (D1), pp. 899-916, (1997).

Fernald FG., **Analysis of atmospheric lidar observations: Some comments**, *Appl. Opt*., **23**: 652-653, (1984).

Flamant C, Pelon J, Flamant PH, Durand P., **Lidar determination of the entrainment zone thickness at the top of the unstable marine atmospheric boundary layer**, *Boundary-Layer Meteorol*. **83**: 247-284, (1997).

FLEXTRA website, http://zardoz.nilu.no/~andreas/flextra+flexpart.html

Frontoso et al., **Study of Planetary Layer evolution in urban/rural sites in Southern Italy**, *poster presentation*, Heidelberg, Germany, June 27-30, (2006).

Frontoso M. G. et al.: **Water vapour mixing ratio distribution in the area of Naples by Raman lidar measurements and a high resolution model**, Proceedings SPIE Europe Remote Sensing 2007 (*in press*).

Grell et al., **Description of the Fifth-Generation Penn State/NCAR Mesoscale Model (MM5)**, NCAR Tech. Note NCAR/TN-3981STR, National Center for Atmospheric Research, Boulder, CO, 138 pp., (1994).

Hooper WP, Eloranta EW., **Lidar measurements of wind in the planetary boundary layer: the method, accuracy and results from joint measurements with radiosonde and Kytoon**, *J. Climate Appl. Meteorol.* **25:** 990-1001, (1986).

Kain, J.S. and J.M. Fritsch, **Convective parameterization for mesoscale models: The Kain-Fritsch scheme. The representation of cumulus convection in numerical models**, Meteor. Monogr., No. 24, Amer. Meteor. Soc., 165-170, (1993).

Kaufmann YJ, Tanre D, Boucher O., **A satellite view of aerosols in the climate system**, *Nature*, **419**, 215–223, (2002).

Klett JD., **Stable analytical inversion solution for processing lidar returns**, *Appl. Opt*., **20,** 211-220, (1981).

Matthias V, Freudenthaler V, Amodeo A, Balin I, Balis D, Bösenberg J, Chaikovsky A, Chourdakis G, Comeron A, Delaval A, De Tomasi F, Eixmann R, Hågård A, Komguem L, Kreipl S, Matthey R, Rizi V, Rodriguez JA, Wandinger U, Wang X., **Aerosol lidar intercomparison in the framework of the EARLINET project. 1. Instruments**, *Appl. Opt.,* **43:** 961-976, (2004).

Melfi SH, Spinhirne JD, Chou SH, Palm SP., **Lidar observation of the vertically organized convection in the planetary boundary layer over the ocean**, *J. Climate Appl. Meteorol*. **24,** 806-821, (1985).

Melfi, S.H., D. Turner, K. Evans, D. Whiteman, G. Schwemmer, and R. Ferrare, **Upper Tropospheric Water Vapour: A Field Campaign of Two Raman Lidars, Airborne Hygrometers, and Radiosondes**, Proceedings of the 19th International Laser Radar Conference, Annapolis, Maryland, June 6-10, (1998).

Pica G., A. Boselli, F. Castaldo, R. Fusco, S. Mattei, M. R. Santovito X. Wang, **New prototype of very compact LIDAR for atmospheric particulate monitoring**, on proceedings of 23° Symposium EARSeL (European Association of Remote Sensing Laboratories), Gent (Belgium), 37, (2003).

Ramanathan V, Crutzen PJ, Kiehl JT, Rosenfeld D., **Atmosphere-Aerosols, climate, and the hydrological cycle**, *Science*, **294**(5549), 2119–2124, (2001).

Seibert P, Beyrich F, Gryning SE, Joffre S, Rasmussen A, Tercier P., **Review and Intercomparison of Operational Methods for the Determination of the Mixing Height**, *Atmos. Environ*. **34:** 1001-1020, (2000).

Sicard M, Pérez C, Rocadembosch F, Baldasano JM, Garcìa-Vizcaino D., **Mixed layer determination in the Barcelona coastal area from regular lidar measurements: methods, results and limitations**, *Boundary Layer Meteorology* **119** (1), 135-157, (2006).

Stull RB., **An Introduction to Boundary Layer Meteorology**, p. 684, ISBN: 9027727694, (1988).

Troen I. and Marth L., **A simple model of atmospheric boundary layer: sensivity to surface evaporation**, Bonn. Layer Mereor. 37, pp. 129–148, (1986).

Vaughan et al., **Humidity measurements in the free troposphere using Raman backscatter**, Q. J. R. Meteorol. Soc., vol. 114, pp. 1471–1484, (1998).

Whiteman et al., **Raman lidar system for the measurement of water vapour and aerosol in the Earth's atmosphere**, Applied Optics 31(16), 3068-3082, (1992).

Introduction

Global mineral dust emissions are estimated 100-500 millions of tons per year, of which the largest part is attributed to deserts. The Sahara is the major source on Earth of mineral dust (60-200 millions of tons per year). The Saharan Dust (referred as SD, hereinafter), mainly constituted of oxides (SiO_2, Al_2O_3, FeO, Fe_2O_3, CaO, and others) and carbonates ($CaCO_3$, $MgCO_3$), can be lifted by convection over hot desertic areas, and can thus reach very high altitudes; from there it can be transported worldwide by winds, covering distances of thousands of kilometers.

The African continent, especially its northern part (that is Tunisia, Algeria and Libya) is one of the main sources of dust. The bulk of the dust is transported westward into the Atlantic Ocean and southward [Barkan et al., 2004]. However, a non-negligible part, estimated to 80-120 Tg per year, is transported northward across the Mediterranean into southern and even central Europe [Prodi and Fea, 1979; Bonelli and Marcazzan, 1996; Collaud Coen et al., 2003].

In the Mediterranean region, Saharan dust represents the major source of nutrients for phytoplankton and other aquatic organisms.

There is a marked difference between the vertical structure of the elevated dust layers over the Atlantic and over the Mediterranean. While the plumes over the Atlantic are quite similar from outbreak to outbreak, the structure of the plumes over the Mediterranean is erratic and changes from case to case [Koren et al., 2003].

In order to study the SD phenomenon and its long-range transport over the Mediterranean basin, synergy between observations and model is required. In this chapter, aerosol extinction vertical profiles during SD episodes measured by two EARLINET lidar systems (Naples and Barcelona) during 2001-2002 are compared to profiles forecasted by the **D**ust **RE**gional **A**tmospheric **M**odel (DREAM).

35 SD cases were successfully captured in Barcelona (41° 23’ N, 2° 07’ E, 115 m asl, Spain) with a 1064 nm backscatter lidar and 45 in Naples (40°50’N, 14°11’E, 118 m asl , Italy) with a 351 nm Raman lidar during 2001-2002. The objective of the present study is twofold: (1) to evaluate the skills of the model to forecast the dust vertical distribution in the Mediterranean region and (2) to derive and interpret the 2-year dust climatology concerning the SD vertical distribution.

The dependence of the SD episodes dynamics on the driving synoptic pattern has been also investigated [Frontoso et al., 2007]. Composite patterns of backtrajectories, wind fields, temperature and geopotential maps are analyzed for all the measured SD cases.

Furthermore, the seasonal variation of the desert dust aerosol loading above the western and central Mediterranean has been studied.

5.1. The Saharan Dust phenomenon

Several studies indicate that aerosol radiative forcing over the Mediterranean region is among the highest in the world [IPCC, 2001]. Indeed, Giorgi [Giorgi, 2006] suggests that the Mediterranean emerges as one the primary climate change Hot-Spots.

Dust aerosols also modify cloud microphysical properties [Kaufman et al., 2002; Prospero et al., 2002, Rosenfeld, 2000; Pruppacher and Klett, 1997; Sassen et al., 2003], the thermal and dynamical atmospheric structure through absorption and reflection of short and longwave radiation [Perez et al., 2006a] and can affect the atmospheric convection [Brooks and Legrand, 2000]. Dust deposition influences the biochemical cycles of both aquatic [Kremling and Streau, 1993] and terrestrial ecosystems [Reichholf, 1986] and, in the regions neighbouring deserts, it represents a risk for human health and air transport activities. In contrast to the greenhouse gases, which affect only the long-wave radiation, dust particle modify both long and short wave radiation components. [Andreae, 1997].

Another important effect of the dust cycle is the triggering of various biochemical reactions between dust ingredients and the Environmental. After depositing over the ocean surface, desert dust containing active iron and phosphorus can cause algal blooms over the surface ocean water [Dulac et al., 1996]. In such processes, dust modifies biochemistry of the ocean water [Kremling

and Streau, 1993], changes features of the terrestrial ecosystems [Reichholf, 1996] and neutralizes acid rains [Hedin and Likens, 1996].
In the last five years, many studies have been focused on understanding different phases of the dust cycle over the Mediterranean and Europe, basing on satellite imaging [Alpert and Ganor, 2001; Israelevich et al., 2002], in situ measurements of deposition, concentration, optical depth [Rodriguez et al., 2001; Israelevich et al., 2003] and lidar observations [Gobbi et al., 2000; Muller et al., 2003; Balis et al., 2004; Papayannis et al., 2005]. As observations indicate, there is a large seasonal variability of the dust cycle that is strongly correlated with the global atmospheric circulation [Moulin et al., 1997].
However, at present, there is a large uncertainty in the globally averaged forcing due to the aerosol indirect effect [Houghton, 2001], which is estimated to be between 0 and -2 Wm^{-2}. Despite the recent notable advances in dust studies, this uncertainty is related mainly to the poor understanding of cloud microphysics together with the fact that aerosols have very inhomogeneous distributions in the atmosphere significantly changing with time. The unsatisfactory description of the dust cycle is mainly due to the lack of enough dense and regular measurements, but also to the incomplete understanding of dust processes such as production, transport, physical and chemical evolution, optical properties and removal processes [Sokolik et al., 2001].
The residence time of aerosols in the atmosphere (in particular of mineral dusts) is of only a few days, therefore their distribution is highly variable both in space and time [Prospero et al., 1981; Mattis et al., 2002; Ansmann et al., 2003]. This is the reason why remote sensing of desert aerosols has increasingly developed as the best technique to catch individual events and to integrate them into regional or global pictures of the aerosol transport. Systematic measurements of the vertical dust distribution are necessary for climatology studies and dust model validation activities. Indeed, several regional models for the simulation and the prediction of the atmospheric dust cycle have been developed in the last years [Nickovic and Dobricic, 1996; Kallos et al., 1997; Ozsoy et al., 2001; Nickovic et al., 2001]. These models are essential to complement the observations and predict the impact of dust over the Mediterranean and Europe.

5.2. The Lidar systems

5.2.1 The Barcelona Lidar system

The aerosol backscatter lidar system of the Universitat Politècnica de Catalunya (UPC) (Barcelona, Spain, 41° 23', 2° 07', 115 m asl) was based on a Nd:YAG laser emitting pulses of 6-ns duration and 160 mJ energy at 1064 nm [Rocandenbosch et al., 2002]. The pulse rate frequency was 20 Hz, the vertical resolution was 7.5 m and the maximum altitude range was 20 km.
The lidar vertical profiles in Barcelona were inverted by using Klett method (for more details, see Chapter 2) at 1064 nm. The assumption of an a priori extinction-to-backscatter ratio (hereinafter referred as lidar ratio, LR) value can introduce errors that may exceed 20-30% [Sasano et al., 1985] especially in cases with high aerosol optical depth. A constant LR of 60 sr was used to invert the Barcelona lidar profiles. This value seems to be the most appropriate after long range transport to western and northern Europe [Mattis et al., 2002; Muller et al., 2003; Ansmann et al., 2003].

5.2.1 The Naples Lidar system

The Raman lidar system of the CNISM Research Unit operating in Naples (Naples, Italy, 40°50', 14°11', 118 m asl) was based on XeF excimer laser emitting pulses of 50 mJ energy at 351 nm, with a duration of 20 ns and a pulse repetition frequency of 50 Hz. Nitrogen Raman measurements were also performed at 387 nm. The raw range resolution was 15 m and the maximum altitude range was 20 km. In order to optimize signal-to-noise ratio the retrieved backscatter and extinction profiles are spatially integrated over 60 m and 180 m, respectively.
For night-time measurements, the lidar vertical profiles in Naples were inverted using the Raman method (for more details, see Chapter 2 and 3) at 351 nm, without any assumption on lidar ratio.

5.3. The DREAM model

The **D**ust **RE**gional **A**tmospheric **M**odel (DREAM) [Nickovic et al., 2001; Pérez et al., 2006] was designed to simulate and/or to predict the atmospheric life cycle of the eroded desert dust; it was developed as a pluggable component of the NCEP/ETA. It solves the Euler-type partial differential non-linear equation for dust mass continuity which is inserted on-line as one of the governing equations in the atmospheric NCEP/ETA atmospheric model.

The concentration equation simulates all major processes of the atmospheric dust cycle, such as production, diffusion, advection and removal, as shown in Fig. 5.1. During the integration, the calculation of the surface dust injection fluxes is made over the model points declared as deserts. Once injected into the air, dust aerosol is driven by the atmospheric model variables: by turbulent parameters in the early stage of the process when dust is lifted from the ground to the upper levels; by winds in the later phases of the process when dust travels away from the sources; finally by thermodynamic processes and rainfall and land cover features which provide wet and dry deposition of dust over the Earth surface.

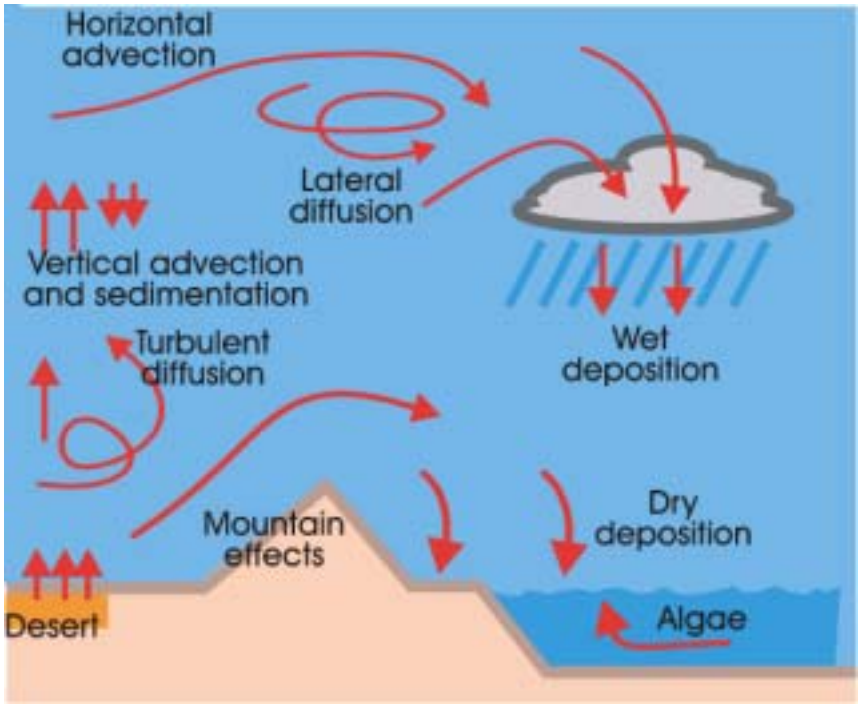

Fig. 5.1. Schematic picture of all the major processes of the dust cycle.

One of the key components of the dust model is the treatment of the sourcing terms in the concentration continuity equation. Failure to adequately simulate/predict the production phase of the dust cycle leads to wrong representation of all other dust processes in the model. Therefore, special attention is made to properly parameterize dust production phase. Wind erosion of the soil in DREAM parameterization scheme is controlled mainly by the following factors: type of soil, type of vegetation cover, soil moisture content, and surface atmospheric turbulence. The major input data used to distinct the dust productive soils from the others are a global data set on land cover.

In DREAM, concentration is used as a surface condition. The released surface concentration of mobilized particles and the corresponding surface vertical flux depends on the structure and state of the soil and the turbulent regime of the lower atmosphere. The vertical flux of dust is also a function of friction velocity and soil moisture.

Its main components are:

- Dust production scheme with introduced viscous sub-layer [Shao, 1993; Janjic, 1994].
- Particle size distribution effects.

- Soil wetness effects on dust production [Fecan, 1999].
- Dry [Georgi, 1986] and wet deposition.
- Horizontal and vertical advection, turbulent and lateral diffusion [Janjic, 1994; Janjic, 1996; Janjic, 1997] represented as for other scalars in the ETA model.

Operational forecasts are performed considering four particle size classes (clay, small silt, large silt and sand) with particle size radii of 0.73, 6.1, 18 and 38 μm, respectively. For long-range transport, only the first two dust classes are relevant for the analysis since their life time is larger than 12 hours. During the EARLINET project, DREAM was used as one of the forecasting models to issue early warning of Saharan dust transport over Europe from 24 to 36 hours in advance (http://www.bsc.es/projects/earthscience/DREAM/).
Since satisfactory three-dimensional dust concentration distribution observations are not yet available to be assimilated, the initial state of dust concentration in the model is defined by the 24-hour forecast from the previous-day model run. The domain of simulation covers northern Africa, the Mediterranean Sea, and southern Europe.

5.4. Comparison model & lidar data

The first step of this work was the validation of the DREAM model with lidar data in Barcelona and Naples. Intensive checking with observations is an important task for every forecast model. The used dataset is based on all the Saharan dust lidar observations made during 2001-2002 in both cities. Cloud screening was manually applied to all lidar profiles in order to avoid contamination by clouds. 12-UTC daily profiles of mass concentration were simulated with the DREAM model for both cities.
In order to perform the validation, the mass concentration C ($\mu g/m^3$) available from the model has been converted into the extinction coefficient α (m^{-1}) available from lidar measurements.
For small particles, a constant specific extinction cross section (the ratio of the extinction coefficient to the aerosol mass concentration), σ^*_λ, has been assumed to obtain the modelled extinction coefficient [Charlson et al., 1992]:

$$\alpha(\lambda) = \sigma^*_\lambda \cdot C \tag{5.1}$$

The modelled aerosol optical depth (referred as AOD, hereinafter), τ (λ), can be written as a function of the column mass loading M, as:

$$\tau(\lambda) = \sigma^*_\lambda \cdot M \tag{5.2}$$

where σ^*_λ has been estimated by calculating a linear regression of the observed AOD values as a function of the columnar dust loading (calculated from the total volume concentration and assuming a dust density of 2.6 g/cm^3 , [Nickovic et al., 2001]). A more complete description of the method can be found in the paper by Pérez and co-workers [Pérez et al., 2006]. In order to apply this method, the AERONET (**AE**rosol **RO**botic **NET**work) sun-photometers data [Holben et al., 1998] from El Arenosillo (37º06' N, 6º42' W, 40 m asl, Spain) and Rome (41º50' N, 12º38' E, 130 m asl, Italy) stations during the period 2001-2002 have been used for Barcelona and Naples, respectively.
A specific extinction cross section value of $\sigma^*_{1064} = 0.28 \pm 0.04$ m^2/g and $\sigma^*_{351} = 0.58 \pm 0.09$ m^2/g has been found for Barcelona and Naples, respectively.
Due to the fact that the two lidar stations operate at different wavelengths, the spectral dependence of the AOD must bee taken into account; this dependence can be expressed as:

$$\frac{AOD(\lambda_1)}{AOD(\lambda_2)} = \left(\frac{\lambda_1}{\lambda_2}\right)^{-\gamma} \tag{5.3}$$

where γ is the Angstrom exponent (referred as AE, hereinafter) which describes the spectral dependence of the AOD [Ångström, 1964; Hamonou et al., 1999]. AE has been determined by a linear regression of AERONET data of AOD at different wavelengths, by making linear Eq. 5.3.
An example of the comparison between the modelled and the measured extinction vertical profile is shown in Fig. 5.2.
Fig. 5.2 (a) shows the dust extinction vertical distribution retrieved by the model (blue squares) and by lidar data (pink squares) for the SD episode of 18th January 2001 in Naples. Fig. 5.2 (b) shows the dust extinction vertical distribution retrieved by the model (blue squares) and by lidar data (pink squares) for the SD episode of 25th June 2001 in Barcelona.
The vertical resolution of the model is variable and decreases with the height. It is based on ETA coordinates (87, 276, 495, 746, 1027, 1341, 1687, 2067, 2482, 2933, 3421, 3949, 4520, 5135, 5798, 6514, 7286, 8120, 9024, 10007, 11079, 12257, 13562 and 15023 m). The vertical resolution of lidar data is 180 m for Naples and 7.5 m for Barcelona.
The agreement between model and lidar data is good, starting from 1000 m in Naples and 2000 m in Barcelona; this is due to the presence of the anthropogenic pollution which is not simulated by the model. The agreement is good even if the modelled and the measured profiles don't match exactly in time. In fact, the lidar measurement of the SD episode of 18th January 2001 in Naples started at 16:44 UTC and stopped at 17:14 UTC and the lidar measurement of the SD episode of 25th June 2001 in Barcelona started at 13:50 UTC and stopped at 14:20 UTC. Model profiles are simulated at 12 UTC in both cases.

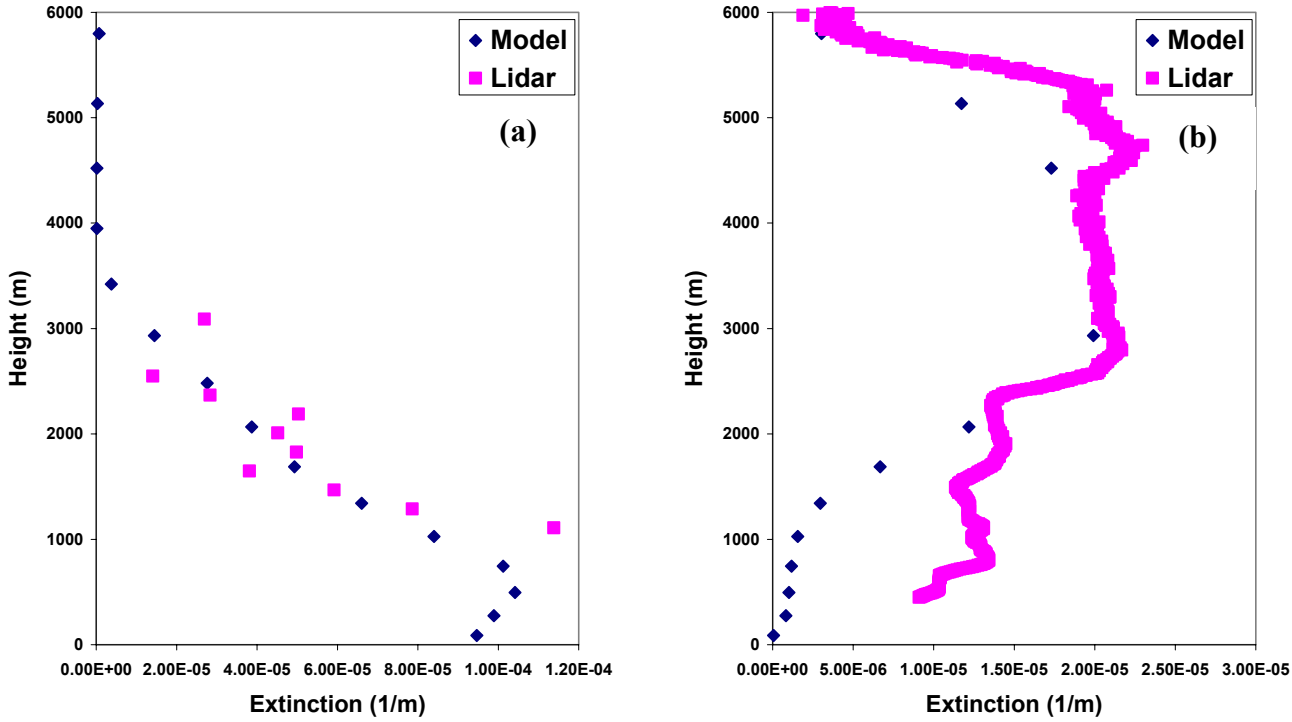

Fig. 5.2 Dust extinction vertical profiles from DREAM model (blue squares) and from Naples lidar data (pink squares) for the SD episode of 18 January 2001 in Naples (a); Dust extinction vertical profiles from DREAM model (blue squares) and from Naples lidar data (pink squares) for the SD episode of 25 June 2001 in Barcelona (b).

Fig. 5.3 shows the comparison between the modelled and the measured annual averaged dust extinction vertical distribution in Barcelona (Fig. 5.3a) and in Naples (Fig. 5.3b). The agreement between model output and lidar observations is good above 2000 m and demonstrates the ability of the model to predict the annual dust cycle in Barcelona (representative of the western Mediterranean) and in Naples (representative of the central Mediterranean). The disagreement found below 2000 m is probably due to the contribution of local and/or anthropogenic aerosol.

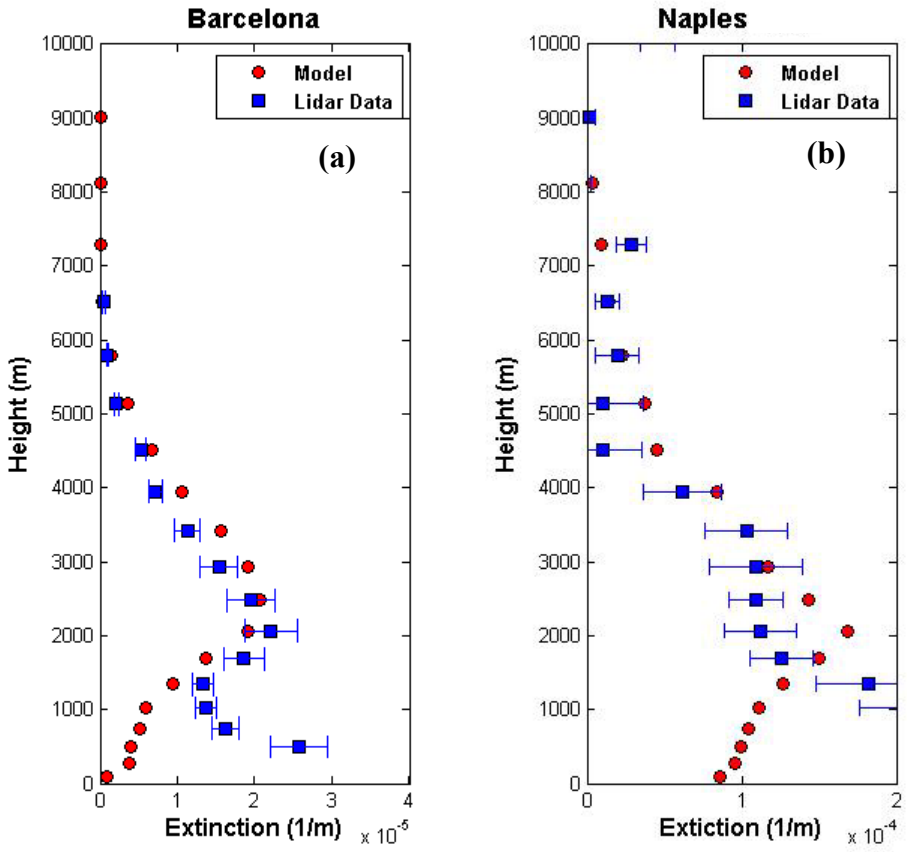

Fig. 5.3 Annual average dust extinction vertical profile from DREAM model (red circles) and from lidar data (blue squares) in Barcelona (a) and in Naples (b). Extinction has been retrieved at 1064 nm wavelength in Barcelona and at 351 nm in Naples.

These results highlight the ability of the model to forecast the desert dust plume by long-term model simulations regardless of the geographic site within the Mediterranean region and thus to bridge the gaps in the experimental observations and to intercompare the dust vertical distribution over the western and central Mediterranean.

5.5. Synoptic patterns

The SD transport over the Mediterranean area takes places each time the appropriate meteorological conditions arise. Therefore, the understanding of the synoptic situation may help to improve the dust packages in atmospheric models. The understanding and describing of the synoptic situation can help in predicting dust generation, with application to a wide range of topics like traffic safety, agriculture, marine biology, health problems, etc. In addition, a better understanding of the synoptics associated with deep dust intrusion may help the forecasters to improve their predictions.
The identification of the major synoptic configurations of SD transport episodes over the western and central Mediterranean basin has been performed. Therefore, all the observed SD episodes

during 2001-2002 in Barcelona and Naples have been classified according to the meteorological and synoptic situation and grouped into pattern types basing on common synoptic signatures. For each station, four synoptic patterns have been identified, but more than 80% of SD episode occurred during three synoptic patterns (**DA-ACNAfr, DP** and **DWCM**), which are described in detail in the following sub-paragraphs.
In order to identify these patterns, many data have been collected following the synoptic fields: wind speed, geopotential and temperature at 950, 900, 800, 700, 600, and 500 hPa and sea level pressure. Also satellite and backtrajectory maps have been taken into account. The accuracy of the analytical trajectories also depends on synoptic conditions; higher wind speeds are generally associated to lower trajectory errors. Sometimes, mesoscale effects may not be captured by the analyses from which the trajectories are calculated, nevertheless they represent a useful tool to identify and analyse situations where these mesoscale effects develop [Rodriguez et al 2002; Jorba et al., 2004]

5.5.1 The DA-ACNAfr pattern

The majority of SD events occur during a combination of a **D**epression system located in the **A**tlantic (approximately in the range 10°W-10°E, 30°N-35°N) and an **A**nti**C**yclonic system located in **N**orth **Afr**ica (approximately in the range 20°W-10°W, 40°N-50°N). This pattern will be referred as **DA-ACNAfr**, hereinafter.
The **DA-ACNAfr** pattern is common for the western and the central Mediterranean (about 50% of all the SD episodes in the western Mediterranean and 60% in the central Mediterranean) and is generally characterized by rather stable weather conditions.
An overview of this typical synoptic situation is illustrated in Figs. 5.4 and 5.5
Fig. 5.4 shows the surface level and the geopotential at 700 hPa level maps by READY (**R**eal-time **E**nvironmental **A**pplications and **D**isplay s**Y**stem) provided by NOAA. The 700 hPa level has been chosen because the average transportation of the dust takes place generally between 600–800 hPa [Carlson and Prospero, 1972; Prospero, 1996; Alpert et al., 2004; Westphal et al., 1987].

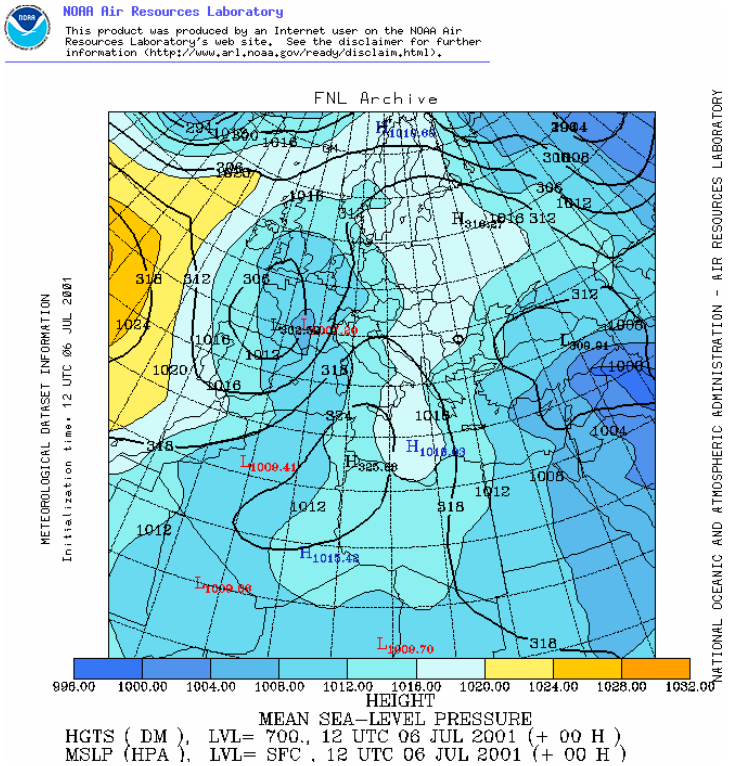

Fig. 5.4 Geopotential at 700 hPa and surface maps from READY – NOAA. This picture corresponds to DA-ACNAfr pattern.

Fig. 5.5 shows the satellite observation by MeteoSat (Fig. 5.5a) and the backtrajectory (Fig.5.5b) maps provided by the German Weather Service. The results of the analytical backtrajectories support the information from the geopotential map. The different colour-lines indicate backtrajectories starting at different heights.

(a) **(b)**

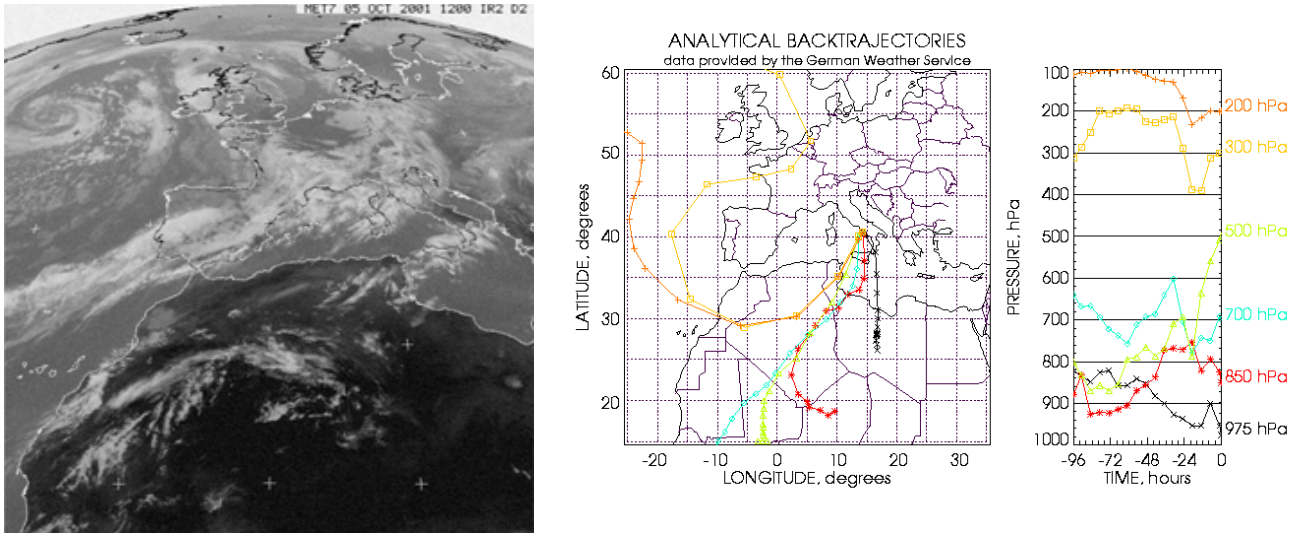

Fig. 5.5 Satellite observation by MeteoSat (a), analytical backtrajectories provided by the German Weather Service (b). The starting point for the backtrajectories is Naples (40°50', 14°11'). These pictures correspond to DA-ACNAfr pattern.

Fig. 5.6 shows the averaged vertical distribution of the SD concentration over the western and the central Mediterranean forecasted by DREAM model. The averaged vertical corresponds to SD episodes occurring during **DA-ACNAfr** pattern. As Fig. 5.6 shows, the shape of the dust plume is the same and also the peak of the dust plume is at the same height (3000 m). Moreover, there is more dust in central Mediterranean.

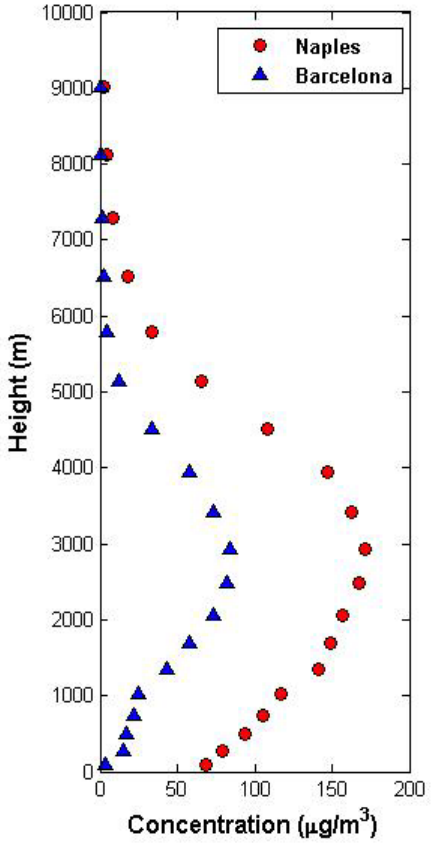

Fig. 5.6 The averaged vertical distribution of the SD concentration over the western and central Mediterranean forecasted by DREAM model.

5.5.2 The DP pattern

Another typical synoptic situation in which SD events occur is a **D**epression system located mainly in **P**ortugal or in the Balearic Islands. This pattern will be referred as **DP**, hereinafter. The **DP** pattern is typical for the western Mediterranean and is generally characterized by unstable weather conditions, strong wind variability, clouds and rain.

An overview of this typical synoptic situation is illustrated in Figs. 5.7 and 5.8.

Fig. 5.7 shows the surface level and the geopotential at 700 hPa level maps by READY (**R**eal-time **E**nvironmental **A**pplications and **D**isplay s**Y**stem) - NOAA. Fig. 5.8 shows the satellite observation by MeteoSat (Fig. 5.8a) and the backtrajectories (Fig. 5.8b) maps provided by the German Weather Service.

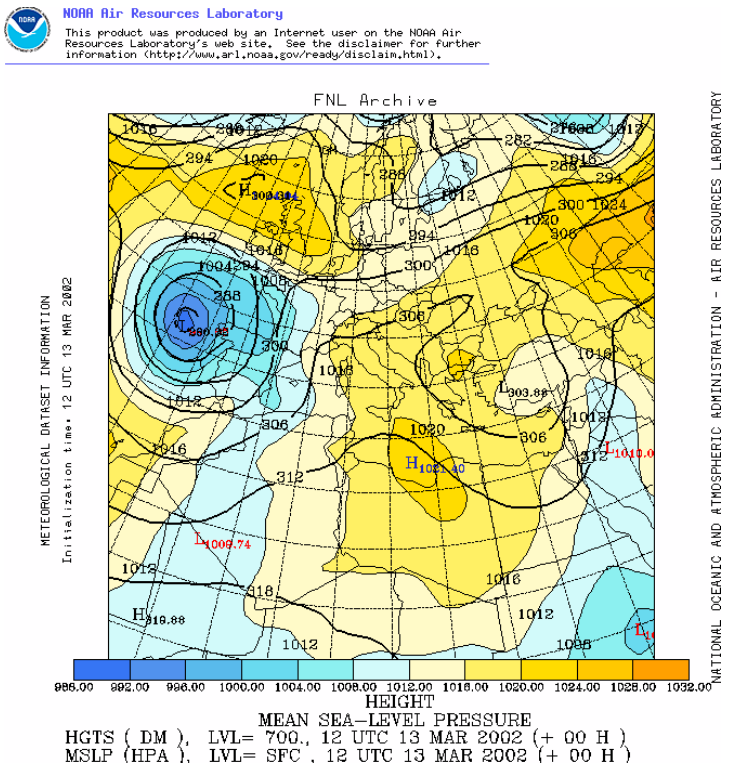

Fig. 5.7 Geopotential at 700 hPa and surface maps from READY – NOAA. This picture corresponds to DP pattern.

(a) **(b)**

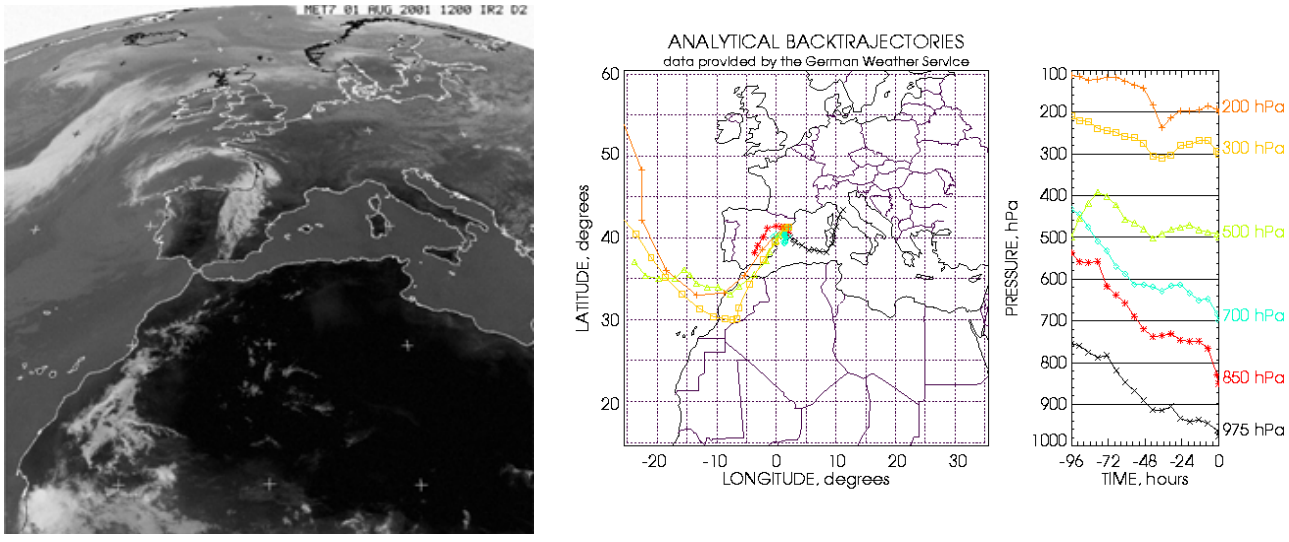

Fig. 5.8 Satellite observation by MeteoSat (a), analytical backtrajectories provided by the German Weather Service (b). The starting point for the backtrajectories is Barcelona (41° 23', 2° 07'). These pictures correspond to DP pattern.

5.5.3 The DWCM pattern

Another typical synoptic situation in which SD events occur is a **D**epression system mainly located in **W**estern or **C**entral **M**editerranean. This pattern will be referred as **DWCM**, hereinafter. The

DWCM pattern is typical for the central Mediterranean and has similar characteristics to the **DP** pattern. In fact, it can be considered as an "evolution" of the **DP** pattern, relatively to the intensity and the location of the low pressure system.
An overview of this typical synoptic situation is illustrated in Figs. 5.9 and 5.10
Fig. 5.9 shows the surface level and the geopotential at 700 hPa level maps by READY (**R**eal-time **E**nvironmental **A**pplications and **D**isplay s**Y**stem) - NOAA. Fig. 5.10 shows the satellite observation by MeteoSat (Fig. 5.10a) and the backtrajectories (Fig. 5.10b) maps provided by the German Weather Service.

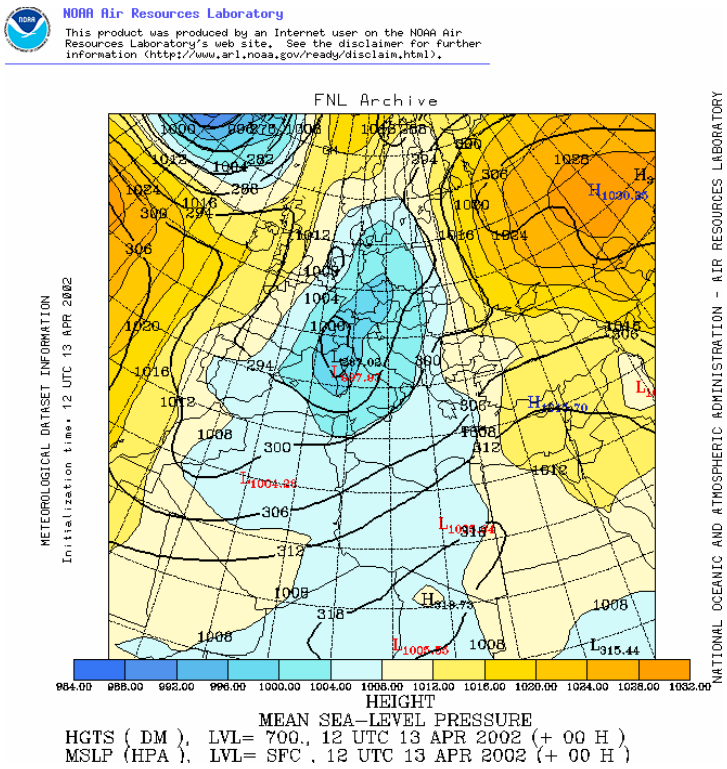

Fig. 5.9 Geopotential at 700 hPa and surface maps from READY – NOAA. This picture corresponds to DWCM pattern.

(a) **(b)**

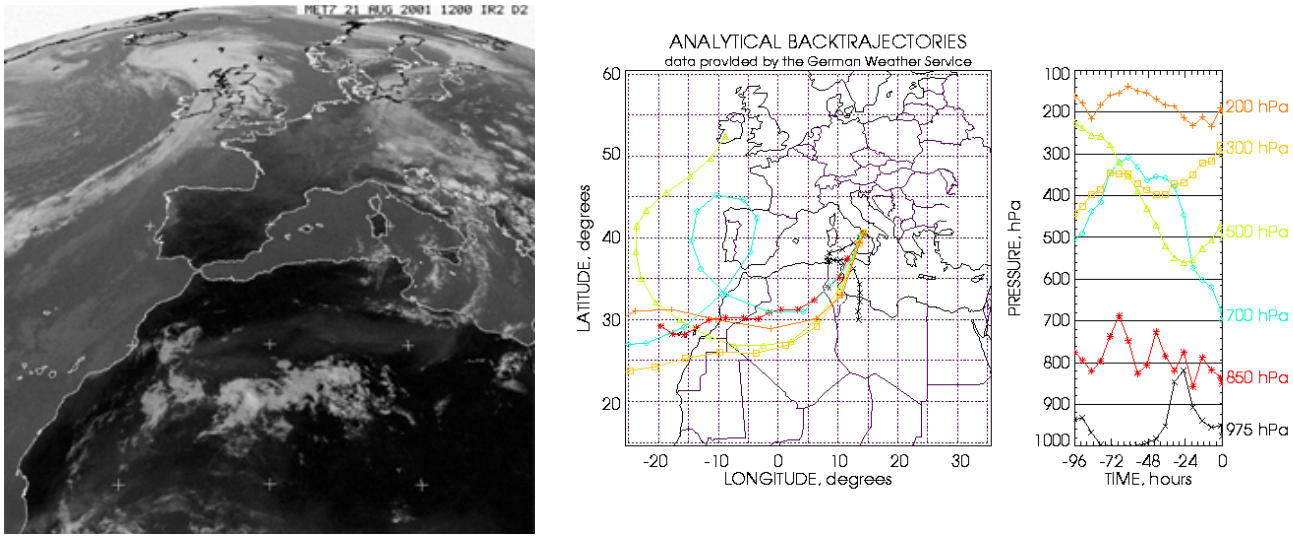

Fig. 5.10 Satellite observation by MeteoSat (a), analytical backtrajectories provided by the German Weather Service (b). The starting point for the backtrajectories is Naples (40°50', 14°11'). This picture corresponds to DWCM pattern.

Fig. 5.11 shows the averaged vertical distribution of the SD concentration over the western and the central Mediterranean forecasted by DREAM model. The averaged vertical corresponds to SD episodes occurring during **DP** and **DWCM** patterns, respectively. As Fig. 5.11 shows, the shape of the dust plume is different and also the peak of the dust plume is at different height (2500 m for central Mediterranean and 3500 m for the western Mediterranean). Therefore, the altitude of the dust plume is higher in the western that in the central Mediterranean. This happens because of different geographical factors, such as the presence of the Atlas Mountains (Morocco) relatively close to South Spain which partially stop the dust transport at low height.
Furthermore, there is more dust in central Mediterranean

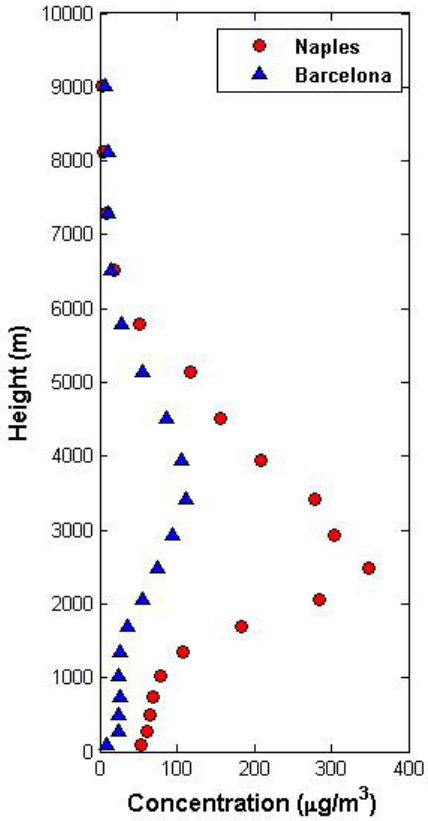

Fig. 5.11 The averaged vertical distribution of the SD concentration over the western and central Mediterranean forecasted by DREAM model.

5.6 Seasonal dust variability in the western and central Mediterranean

An average seasonal analysis plays an important rule in order to determine a wide assessment of aerosol characteristics and dynamics, highlighting trends and differences in the aerosol extinction vertical distribution over the Mediterranean region.

A comprehensive investigation of the seasonal variability of SD properties over the western and central Mediterranean has been performed.

Data have been collected into four groups: spring (**M**arch-**A**pril-**M**ay 2001-2002, referred as **MAM** hereinafter), summer (**J**une-**J**uly-**A**ugust 2001-2002, referred as **JJA** hereinafter), autumn (**S**eptember-**O**ctober-**N**ovember 2001-2002, referred as **SON** hereinafter) and winter (**D**ecember-**J**anuary-**F**ebruary 2002-2003, referred as **DJF** hereinafter).

Fig. 5.12 shows the seasonal variability of the SD concentration over the western and the central Mediterranean. The peak of SD concentration both for the western and the central Mediterranean is in spring (more than 60% and 70% of the annual concentration for western and central Mediterranean, respectively), the lowest dust activity in winter. Furthermore, the major difference in SD concentration between the western and the central Mediterranean is observed in spring, when a significant fraction of dust moves toward eastern Mediterranean due to the Sharav cyclone. In summer and autumn, the dust concentration is approximately the same, but there are differences in the vertical distribution. In fact, in autumn the height of dust plume is at higher height in the western than in central Mediterranean.

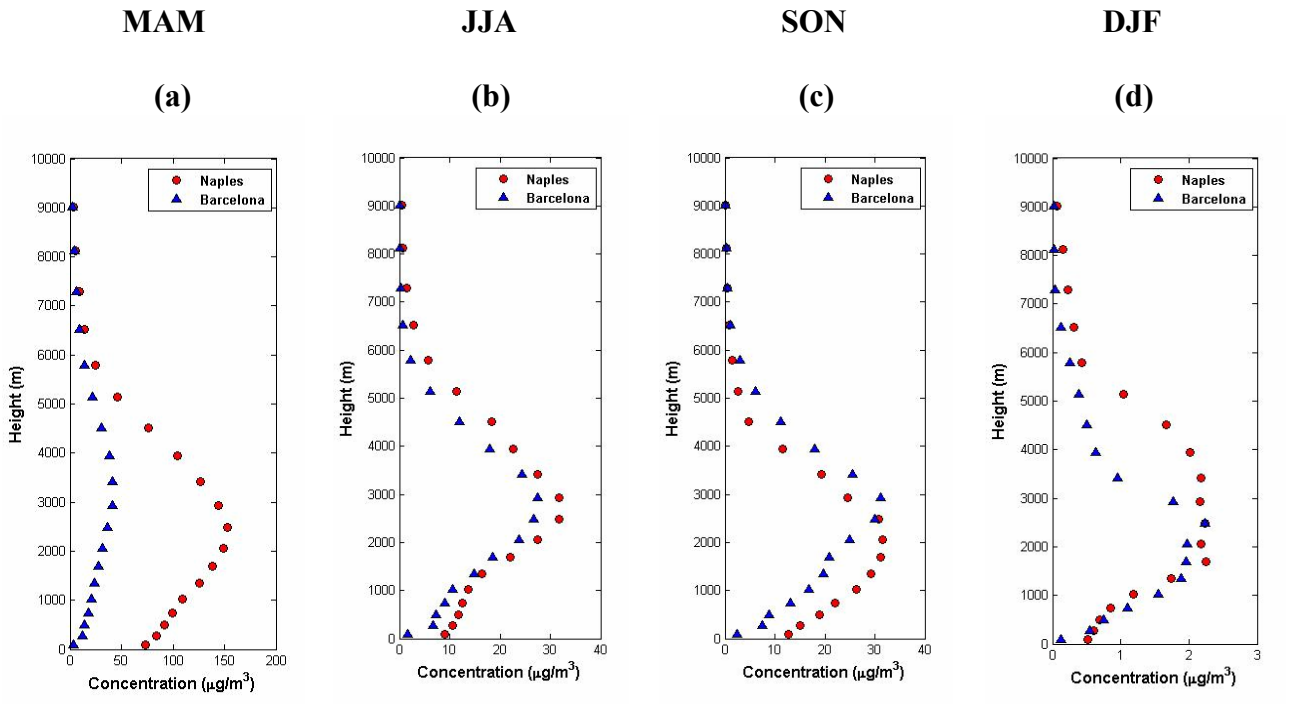

Fig. 5.12 Seasonal averaged dust concentration over the western (blue triangle) and central Mediterranean (red circles) during spring (a), summer (b), autumn (c) and winter (d), forecasted by DREAM model.

Fig. 5.13 shows the maps of the AOD at 550 nm over the western and central Mediterranean. The four-plots reveal the strong seasonal cycle of the AOD over the Mediterranean region. A clear seasonal pattern with maximum AOD values (> 0.35 in the central Mediterranean and > 0.15 in the western Mediterranean) in spring and minimum AOD values (< 0.025) in winter is observed. In this season the minimum incidence of long range SD transport is registered. This is in agreement with the seasonal and latitudinal pattern of precipitation (the most efficient removal of atmospheric aerosol) in the Mediterranean region [Mariotti et al., 2002]. In fact, the higher AOD registered in spring is also a consequence of a minimum aerosol scavenging by precipitation. Conversely, the higher precipitation rate registered over the Mediterranean in winter (particularly at latitudes 40° N) tends to reduce the mean residence time of aerosols in the atmosphere, and thus the mean AOD.
In autumn and summer low-moderate values of the AOD are observed.

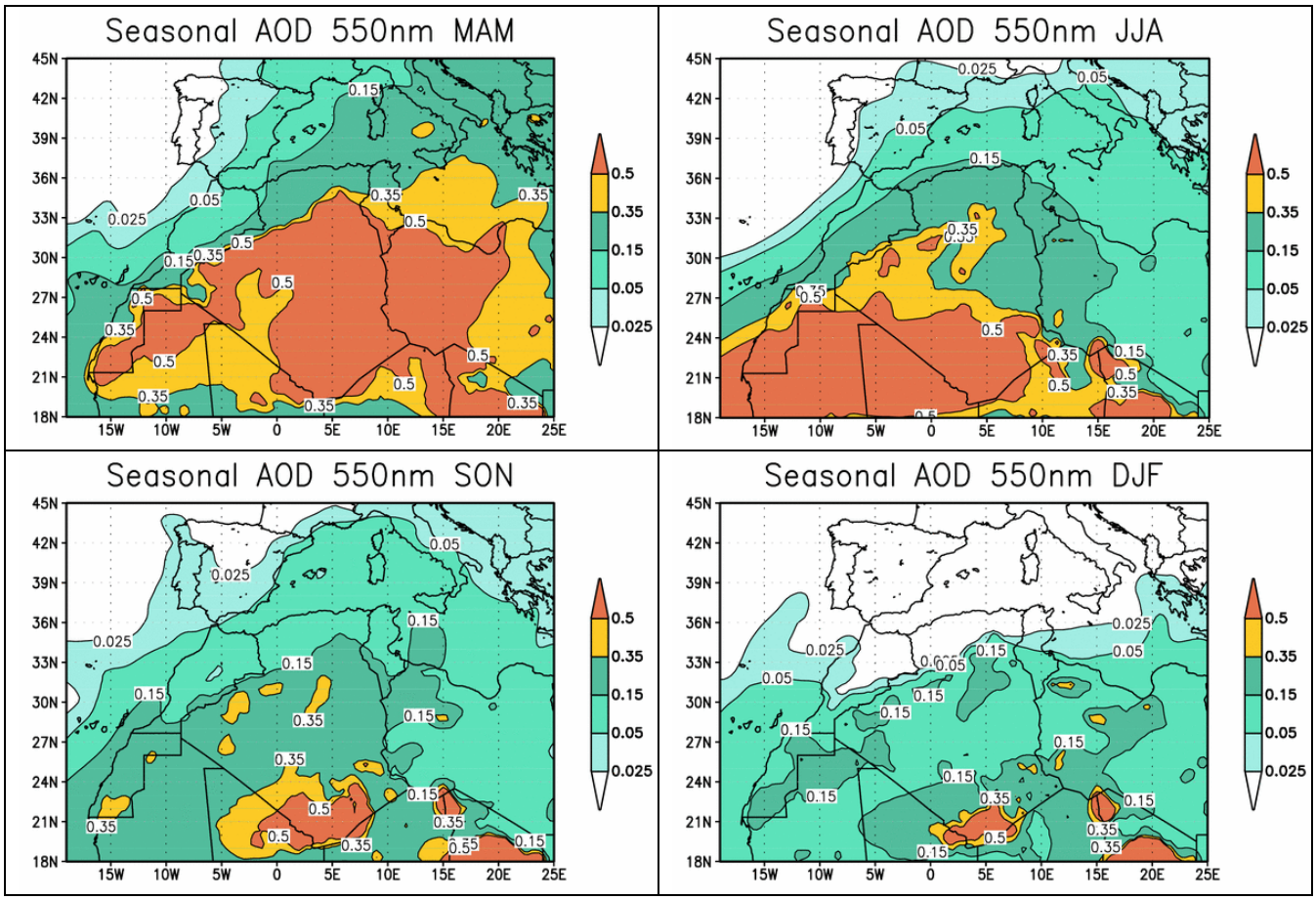

Fig. 5.13. The seasonal variation of AOD at 550 nm over the western and central Mediterranean forecasted by DREAM model.

Figs. 5.14 and 5.15 show the maps of the seasonal variation of the extinction vertical profiles at 550 nm in the western (lon = 2.12) and central (lon = 14.18) Mediterranean, respectively. It confirms all the information present in Fig. 6.3 and 6.4: the major differences between the western and the central Mediterranean are observed in spring; in summer and in autumn both in western and in central Mediterranean the dust intrusion is not strong and in winter the extinction value at 550 nm is lower than 1.0e-5 m^{-1}.

Figs. 5.14 and 5.15 also show that, during summer and autumn, the dust emission sources between 24 N and 27 N seems to contribute only to the dust transport over the western Mediterranean. Moreover, otherwise to other seasons, in spring the dust arrives over the Mediterranean basin at higher altitude with respect to the sources and this could be related to different dust transport dynamics occurring in spring.

In both western and central Mediterranean, the highest extinction value is observed in spring and is associated to dust extending up to altitudes of 5 km.

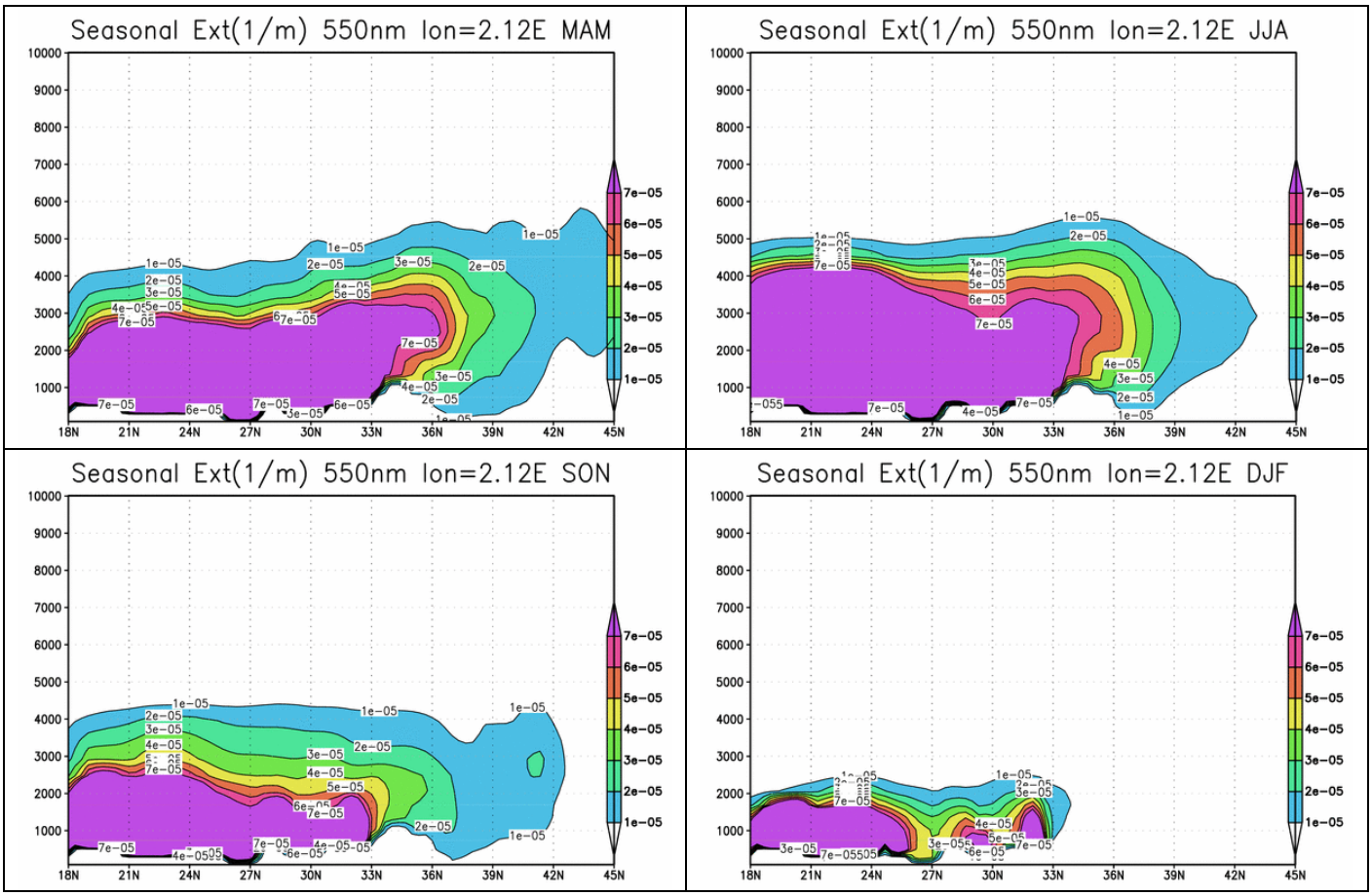

Fig. 5.14 The seasonal variation of extinction at 550 nm in the western Mediterranean (lon = 2.12) forecasted by DREAM model.

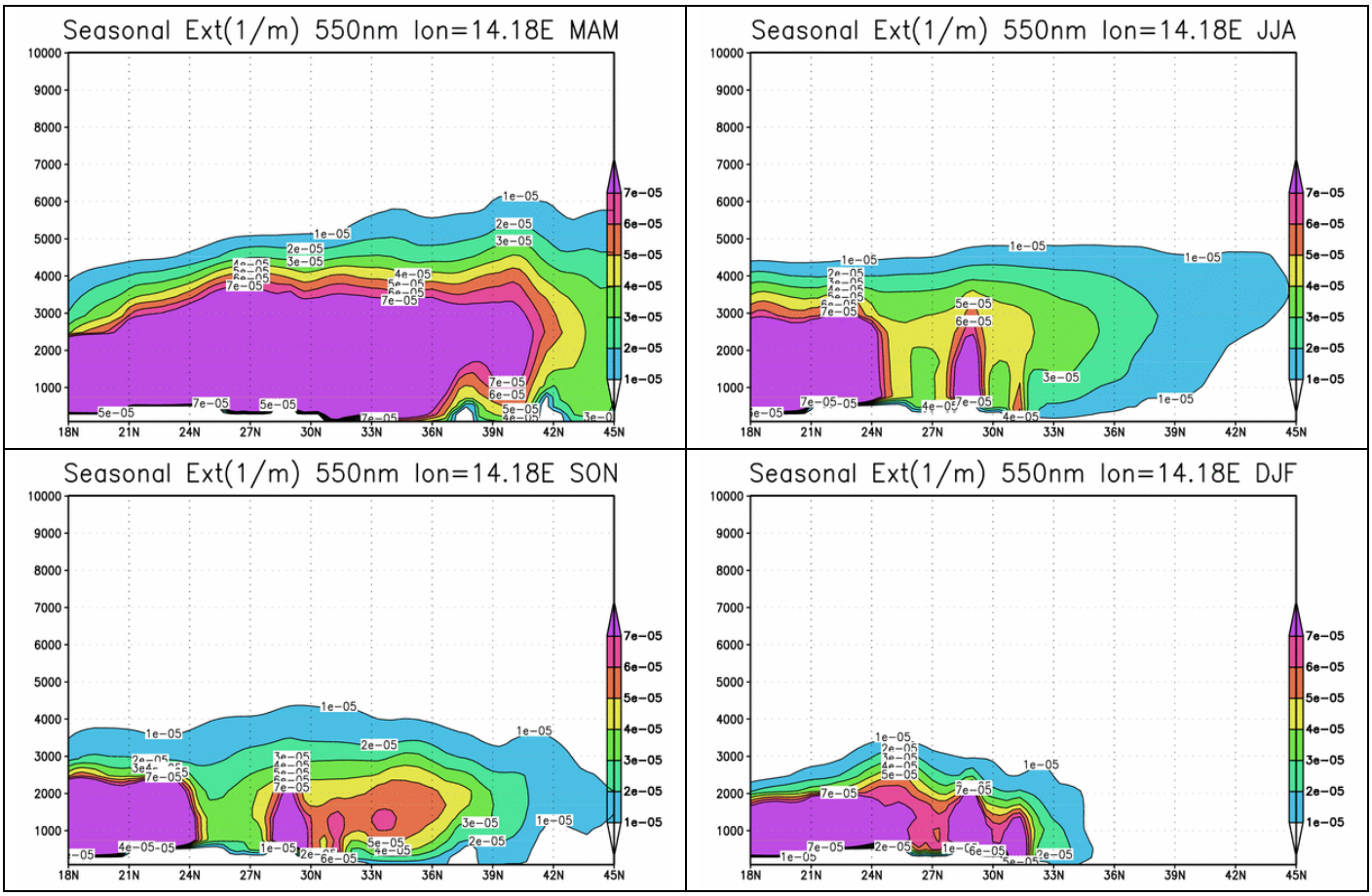

Fig. 5.15 The seasonal variation of extinction at 550 nm in the central Mediterranean (lon = 14.18) forecasted by DREAM model.

5.7 Conclusion

This chapter presents a comprehensive analysis of the aerosol vertical distribution over the western and central Mediterranean area during SD episodes, by the synergy between model and lidar data.

The aerosol extinction vertical distribution simulated by DREAM has showed a rather good agreement with the lidar profiles both in Barcelona and in Naples. Comparisons of individual profiles are rather difficult because of the different spatial and temporal resolution of lidars and model, nevertheless the agreement improves when average on large scale (seasonal and/or annual) is considered. At low height, the deviations between model and lidar data are reasonably due to the local and/or anthropogenic aerosols that contribute significantly to the measured aerosol extinction. Collecting much complementary information as geopotential, surface temperature and wind fields, backtrajectories and satellite observations, the synoptic situation associated with SD episodes over the western and central Mediterranean can be understood.

The DREAM model has also demonstrated to be able to reproduce the main seasonal features of the SD vertical distribution over the western and central Mediterranean. The major difference in SD concentration between the western and the central Mediterranean is in spring; in fact, during this season most of SD moved toward eastern Mediterranean, due to the Sharav cyclone. In summer and autumn, the SD concentration is approximately the same, but in autumn the dust plume is at higher height in western than in central Mediterranean

5.8 References

Alpert and Ganor, **Sahara mineral dust measurements from TOMS: Comparison to surface observations over the Middle East for the extreme dust storm**, Journal of Geophysical Research, Volume 106, Issue D16, p. 18275-18286, (2001).

Angstrom, **The parameters of atmospheric turbidity**, Tellus 16, 64-75, (1964).

Ansmann, A., et al., **Long-range transport of Saharan dust to northern Europe: The 11 – 16 October 2001 outbreak observed with EARLINET**, J. Geophys. Res., 108(D24), 4783, doi:10.1029/2003JD003757, (2003).

Balis et al., **Optical properties of Saharan dust layers as detected by a Raman lidar at Thessaloniki, Greece**, Geophys. Res. Lett., 31, L13104, doi:10.1029/2004GL019881, (2004).

Barkan J., Alpert P., Kutiel H., Kishcha P., **Synoptics of dust transportation days from Africa toward Italy and central Europe**, J. Geophys. Res, VOL. 110, doi:10.1029/2004JD005222, (2005).

Bockmann et al., **Aerosol Lidar intercomparison in the framework of the EARLINET project: 2. Aerosol backscatter algorithms**, Appl. Opt., 43, 977–989, (2004).

Bonelli et al., **Elemental composition and air trajectories of African dust transported in northern Italy, The Impact of Desert Dust Across the Mediterranean**, edited by Guerzoni, S. and Chester, R., Kluwer Academic Publishers, Dordrecht, pp. 275–283, (1996).

Bosenberg et al., **EARLINET: A European Aerosol Research Lidar Network**, Rep. 348, MPI Rep. 337, 191 pp., Max-Planck-Inst. fur Meteorol., Hamburg, (2003).

Brooks N. and M. Legrand**, Dust variability over northern Africa and rainfall in the Sahel,** in Linking Climate Change to Land Surface Change, edited by S. J. McLaren and D. Kniveton, pp. 1-25, Springer, New York, (2000).

Charlson RJ, Schwartz SE, Hales JM, Cess RD, Coakley JA, Hansen JE, Hoffman DJ., **Climate forcing by anthropogenic aerosols**, Science 255, 423-430, (1992).

Collaud Coen et al., **Saharan dust events at the Jungfraujoch: Detection by wavelength dependence of the single scattering albedo and analysis of events during the years 2001 and 2002**, Atmos. Chem. Phys. Discuss., vol.3, pp. 5547-5594, (2003).

Fernald et al., **Determination of Aerosol Height Distributions by Lidar**, Journal of Applied Meteorology", **11**, pp.482-489, (1972).

Frontoso M.G. et al.: **The vertical distribution of Saharan dust over the western and central Mediterranean through dust modeling and lidar observations**, Proceedings IGARSS 2007 (*in press*).

Georgi, F., **A Particle Dry-Deposition Parameterization for Use in Tracer Transport Models**, J. Geoph. Res., 91, 9794-9806, (1986).

Gobbi et al., **Altitude resolved properties of a Saharan dust event over the Mediterranean**, Atmos. Environ., 34, 5119–5127, (2000).

Hamonou E., Chazette P., Papayannis A., Balis D., Marenco F., Santacesaria V., Ancellet G., **Ground-based measurements of Saharan dust optical properties in the frame of the European MEDUSE Project**, Journal of Aerosol Science, Vol. 28, Suppl. 1, pp. 695-696(2), (1997).

Holben et al., **AERONET—A federated instrument network and data archive for aerosol characterization**, Remote Sens. Environ., 66, 1 –16.

Houghton J.T. et al., **Climate Change 2001: The Scientific Basis**, (Cambridge U. Press, 2001).

IPPC - Intergovernmental Panel on Climate Change, **Climate Change 2001: The Scientific Basis**, edited by J. T. Houghton et al., Cambridge Univ. Press, New York, (2001).

Kallos et al., **The regional weather forecasting system SKIRON: An overview, in Proceedings of the Symposium on Regional Weather Prediction on Parallel Computer Environments**, edited by G. Kallos, V. Kotroni, and K. Lagouvardos, pp. 109– 122, Univ. of Athens, Athens, Greece, (1997).

Kaufman et al., **A satellite view of aerosols in the climate system**, Nature, 419, 215–223, (2002).

Klett, **Lidar inversion with variable backscatter/extinction ratios**, Appl. Opt. **24**, 1638-1643, (1985).

Kremling, K., and P. Streau, **Saharan dust influenced trace element fluxes in deep North Atlantic subtropical waters**, Deep Sea Res., Part I, 40, 1155–1168, (1993).

Mariotti, A., Struglia, M. V., Zeng, N., and Lau, K.-M., **The hydrological cycle in the Mediterranean region and implications for the water budget of the Mediterranean Sea**, J. Climate., 15, 1674–1690, (2002).

Matthias et al., **Aerosol Lidar intercomparison in the framework of EARLINET project: 1. Instruments**, Appl. Opt., 43, 961– 976, (2004).

Mattis et al., **Dual wavelength Raman lidar observations of the extinction-to-backscatter ratio of Saharan dust**, Geophys. Res. Lett., 29(9), 1306, doi:10.1029/2002GL014721, (2002).

Muller et al., **Saharan dust over a central European EARLINET-AERONET site: Combined observations with Raman lidar and Sun photometer**, J. Geophys. Res., 108(D12), 4345, doi:10.1029/2002JD002918, (2003).

Nickovic et al., **A model for long-range transport of desert dust**, Mon. Weather Rev., 124, 2537–2544, (1996).

Nickovic et al., **Model for prediction of desert dust cycle in the atmosphere**, J. Geophys. Res., 106, 18,113– 18,129, (2001).

Ozsoy et al., **A hemispheric dust storm affecting the Atlantic and Mediterranean (April 1994): Analyses, modelling, ground-based measurements and satellite observations**, J. Geophys. Res., 106, 18,439–18,460, (2001).

Papayannis et al., **Measurements of Saharan dust aerosols over the eastern Mediterranean using elastic backscatter-Raman lidar, spectro-photometric and satellite observations in the frame of the EARLINET project**, Atmos. Chem. Phys., 5(8), 2065– 2079, (2005).

Pappalardo et al., **Aerosol lidar ratio measurements in the framework of EARLINET**, Geophysical Research Abstracts, Vol. 7, 08329, (2005).

Perez et al., **A long Saharan dust event over the western Mediterranean: Lidar, Sun photometer observations**, and regional dust modelling, J. Geophys. Res., 111, D15214, doi:10.1029/2005JD006579, (2006).

Prodi and Fea, **A case of transport and deposition of Saharan dust over the Italian peninsula and southern Europe**, Journal of Geophysical Research, 84, pp. 6951-6960, (1979).

Prospero et al., **Atmospheric transport of soil dust from Africa to South America**, Nature, 289, 570–572, (1981).

Prospero et al., **Environmental characterization of global sources of atmospheric Environmental characterization of global sources of atmospheric (TOMS) absorbing aerosol product**, Rev. Geophys., 40(1), 1002, doi:10.1029/2000RG000095, (2002).

Pruppacher and Klett, **Microphysics of clouds and precipitation**, Kluwer Academic Publishers, (1997).

Reichholf, J. H., **Is Saharan dust a major source of nutrients for the Amazonian forest**, Suud. Neotrop. Fauna Environ., 21, 251– 255, (1986).

Rocadenbosch et al., **The UPC scanning Raman lidar: an engineering overview,** in Proceedings of 21st International Laser Radar Conference, Defence R& D – Valcartier, Val-Bélair, pp. 69-70, (2002).

Rodrıguez et al., **Saharan dust contribution to PM10 and TSP levels in Southern and Eastern Spain**, Atmos. Environ., 35(14), 2433– 2447, (2001).

Rosenfeld et al., **Desert dust suppressing precipitation: A possible desertification feedback loop**, Proc. Natl. Acad. Sci. U.S.A., 98, 5975–5980, (2001).

Sasano et al., **Error caused by using a constant extinction/backscattering ratio in the lidar solution**, Appl. Opt., 24, 3929–3932, (1985).

Sassen et al., **Saharan dust storms and indirect aerosol effects on clouds: CRYSTAL-FACE results**, Geophysical Research Letters, 30, No. 12, 1633, doi:10.1029/2003GL017371, (2003).

Sokolik et al., **Introduction to special section: Outstanding problems in quantifying the radiative impacts of mineral dust**, J. Geophys. Res., 106, 18,015– 18,027, (2001).

Introduction

Because of tropospheric aerosols are highly variable in space and time due to variable sources and short atmospheric residence times [Kiehl, 1996], also their effects are highly variable. Due to their variability and the current limited capabilities to monitor aerosols, basic questions remain about the global distribution and composition of aerosols. Model estimates of the radiative forcing from aerosols are highly uncertain, largely because current capabilities to observe aerosol from space are insufficient to constrain key assumptions in these models. In particular, the largest sources of uncertainty in estimating longwave radiative fluxes at the Earth's surface and within the atmosphere are connected with current difficulties in determining the vertical distribution and overlap of multilayer clouds and their icewater path. Because of the short time scales and nonlinear relationships typical of cloud processes, nearly simultaneous observations of atmospheric state, aerosol and cloud optical properties, and radiative fluxes are necessary to test the ability of cloud models to reproduce the physics of cloud-radiation feedbacks.

As demonstrated by LITE (**L**idar **I**n-space **T**echnology **E**xperiment) [Winker, 1996] and ICESat/GLAS (**I**ce, **C**loud and land **E**levation **Sat**ellite/**G**eoscience **L**aser **A**ltimeter **S**ystem) [Spinhirne, 2005] missions, satellite lidars have a significant ability to profile multi-layer aerosol and cloud structures.

The CALIPSO (**C**loud **A**erosol **L**idar and **I**nfrared **P**athfinder **S**atellite **O**bservations) project started in April 2006; it is a collaborative effort to evaluate direct and indirect aerosol radiative forcing, to measure longwave surface and atmospheric surface fluxes, and to estimate clouds irradiative effects on the climate system [Winker, 2003]. The CALIPSO satellite flies in formation with the EOS Aqua and CloudSat satellites and the other satellites of the Aqua constellation, and provides comprehensive observations of cloud vertical structure on a *global scale*. The CALIPSO satellite carries the first satellite-borne polarization lidar instrument, CALIOP (Cloud-Aerosol Lidar with Orthogonal Polarization), which provides highly vertical-resolved aerosol profiles on the global scale.

During its three-year mission, CALIPSO will acquire a global suite of measurements. The acquisition of simultaneous and coincident observations allows numerous synergies to be realized by combining CALIPSO observations with complementary observations from ground and other platforms.

The CALIPSO validation plan is a central issue to test the confidence level of the satellite data products and thus assure a high quality dataset.

Direct comparison of ground-based and spaceborne aerosol lidar products is a difficult task for several reasons.

Because of CALIOP is an elastic lidar, it cannot provide direct measurement of both extinction and backscatter profile. This means that special care has to be used in the lidar ratio choice. Furthermore, retrieving the spatial and optical properties of clouds and aerosols from the CALIOP data will be confronted by a number of difficulties that are not faced in the analysis of ground-based data. Among these, there are: i) the very large distance from the target; ii) the high speed at which the satellite traverses the ground track; iii) the ensuing low signal-to-noise ratio that result from the mass and power restrictions imposed on space-based platforms.

Correlative measurements are performed by several instruments, which provide data relevant to CALIPSO products validation.

In this chapter, after the description of the CALIPSO project, the CALIOP lidar and the EARLINET strategy for CALIPSO validation program, the novel algorithm CESC (**C**ounter-propagating **E**lastic **S**ignals **C**ombination) [Wang, 2007] is described. By the application of this algorithm, it is possible to retrieve the aerosol backscattering and extinction vertical profiles from simultaneously detected ground and space elastic lidar signals, without any *a priori* hypothesis on aerosol particles properties. This technique can be applied at any wavelength whenever two "counter looking" lidars are available and the atmosphere can be considered horizontally

homogeneous in a spatial scale of the order of the distance between the two lidar beams. The results of many simulations and the application to a real case are also presented.

6.1. The NASA-CALIPSO project

The Cloud Aerosol Lidar and Infrared Pathfinder Satellite Observations (CALIPSO) mission is a collaborative effort between NASA Langley Research Center, the French Centre National d'Etudes Spatiales (CNES), Hampton University, the Institut Pierre Simon Laplace, and the Ball Aerospace and Technologies Corporation.

CALIPSO fly at an altitude of 705 km and an inclination of 98^{o}, in formation with the EOS Aqua satellite as part of the Aqua constellation. The Aqua constellation is a group of 5 satellites which fly in loose formation to allow investigation of the Earth system by synergistically combining data from multiple platforms.

The primary objective of the CALIPSO 3-year mission is to provide the observations necessary to improve our understanding of the effects of clouds and aerosols on the climate system. In particular, the main scientific goals are to evaluate direct and indirect aerosol radiative forcing, to measure long-wave surface and atmospheric surface fluxes and to estimate clouds radiative effects. These topics are presently the largest uncertainties in our ability to predict future climate change. To this purpose CALIPSO payload is furnished with three coaxial nadir-viewing instruments: a two-wavelength polarization-sensitive backscatter lidar (CALIOP i.e. **C**loud-**A**erosol **LI**dar with **O**rthogonal **P**olarization, for more information see paragraph 6.2) operating at 532 nm and 1064 nm, a Wide Field Camera (WFC) operating in the 670 nm region, and a three channels Imaging Infrared Radiometer (IIR) operating in thermal region at 8.7 μm, 10.5 μm and 12.0 μm for the retrieval of cirrus particle size. These instruments are designed to operate autonomously and continuously, although the WFC acquires science data only under daylight conditions [Winker, 2003]. The payload also includes several support systems: a Payload Controller (PLC) and an X-band transmitter subsystem. The payload controller performs control and data handling functions for all three instruments as well as for the X-band transmitter, which is used to downlink instrument science and housekeeping data.

Fig. 6.1 shows the physical layout of the CALIPSO satellite payload and Table 1 shows the key-instrument characteristics.

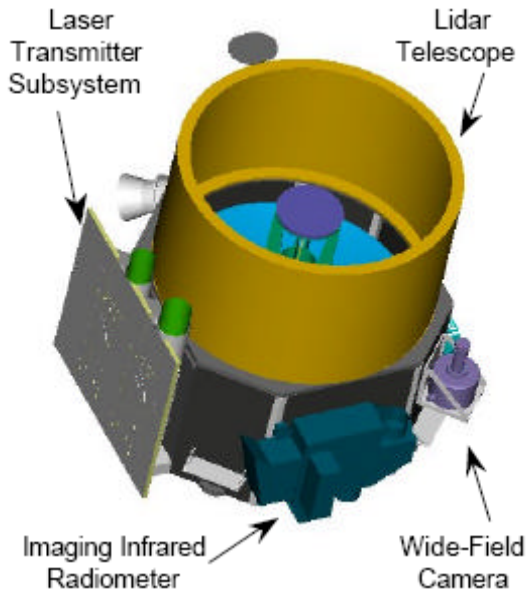

Fig. 6.1. Schematic drawing of the CALIPSO satellite instrumentation. From Winker, 2003.

Table 1. Characteristics of the CALIPSO lidar, infrared imager, and wide-field camera.

LIDAR

Laser	2 ND:YAG @ 110 mJ
Wavelength	532 nm, 1064 nm
Repetition Rate	20.16 Hz
Receiver telescope	1.0 m diameter
Polarization	532 $\parallel$ and $\perp$
Ground foot print	70 m

Wide Field Camera

Wavelength	645 nm
Spectral Width	50 nm
IFOV	125 m
Swath	60 km

Imaging Infrared Radiometer

Wavelength (spectral resolution)	8.65 (0.9) μm , 10.60 (0.6) μm, 12.05 (1.0) μm
IFOV	1 km
Swath	64 km

Direct comparison of ground-based and spaceborne aerosol lidar products is a difficult task for several reasons:

- Different atmospheric attenuation has to be taken into account.
- Raman measurements are not available for satellite lidars.
- Vertical and horizontal resolution can be rather different.
- Horizontally inhomogeneous aerosol conditions may lead to significant differences in the aerosol profiles obtained from ground and space.
- Being the interesting altitude range from ground up to 30-40 km, ground based systems must handle a very high dynamic range of the signals.

The CALIPSO validation plan is a central issue to test the confidence level of the satellite data products and thus assure a high quality dataset. Important to the CALIPSO validation program are the Q*uid Pro Quo* (QPQ) activities [Quid Pro Quo, website] in cooperation with existing measurement sites. These sites are able to provide data relevant to CALIPSO validation at times when the ground-track of the CALIPSO satellite is within a specified coincident distance, or the air masses are shown to be similar. Several instrument networks and individual sites have been identified by the *QPQ* team as potentially suitable for the validation of CALIPSO data products. The networks include: the **AE**rosol **RO**botic **NET**work (AERONET), **A**sian **D**ust **NET**work (AD-NET), **A**tmospheric **R**adiation **M**easurement (ARM) program, **C**limate **M**onitoring and **D**iagnostics **L**aboratory (CMDL), **E**uropean **A**erosol **R**esearch **LI**dar **NET**work (EARLINET), **M**icro **P**ulse

Lidar **NET**work (MPLNET), **N**etwork for the **D**etection of **S**tratospheric **C**hange (NDSC), **R**egional **E**ast **A**tmospheric **L**idar **M**esonet (REALM), **Sur**face **Rad**iation (SurfRad) budget network, **US D**epartment of **A**griculture (USDA) and the **M**ulti-**F**ilter **R**otating **S**hadowband **R**adiometer (MFRSR) network. These networks are considered because of their measurements from instruments suitable for CALIPSO validation including: lidars, cloud radars, sunphotometers, MFRSRs, infrared radiometers, nephelometers, and absorption photometers [Kovacs, 2002].

The validation of CALIPSO data products via intercomparisons with independent measurements is essential to the production of a high quality dataset. Data products from CALIPSO are validated through comparisons with correlative in situ and remote sensing measurements.

Direct comparison implies that the correlative measurements view the same atmospheric features (e.g., same cloud or aerosol layers) as observed by all instruments. In the best of circumstances, the instruments would share the same field of view and measurements occur simultaneously. For ground-based systems, matching measurements with satellite observations can be exceedingly difficult because of the brief window of opportunity during a satellite overpass, and especially for spaceborne lidars or radars with a very narrow field of view. Fortunately, aerosol air masses have correlation scales of 50-100 km and lifetimes of several hours or more. For clouds, the length scales can be significantly smaller (a few kilometers to tens of kilometers) and lifetimes are as short as a few minutes. These length and time scales, thus, provide guidelines on matching requirements needed between sensor systems for aerosol and cloud features. Trajectory analysis may also be employed to improve matching conditions for observations that have large spatial and temporal separations.

An alternative approach to direct comparisons could be to consider an ensemble of observations collected over a long period or a variety of conditions. This approach would be especially appealing for geophysical phenomena that have very restrictive matching requirements such as for cumulus clouds.

Fig. 6.2 shows a map of the groundtrack for the 16-day repeating orbit of CALIPSO. The number of coincident observations during 16 days of orbits for each validation site generally increases with latitude. However, effective validation of aerosol and cloud parameters should be globally distributed to allow validation of these parameters for a variety of aerosol and cloud types.

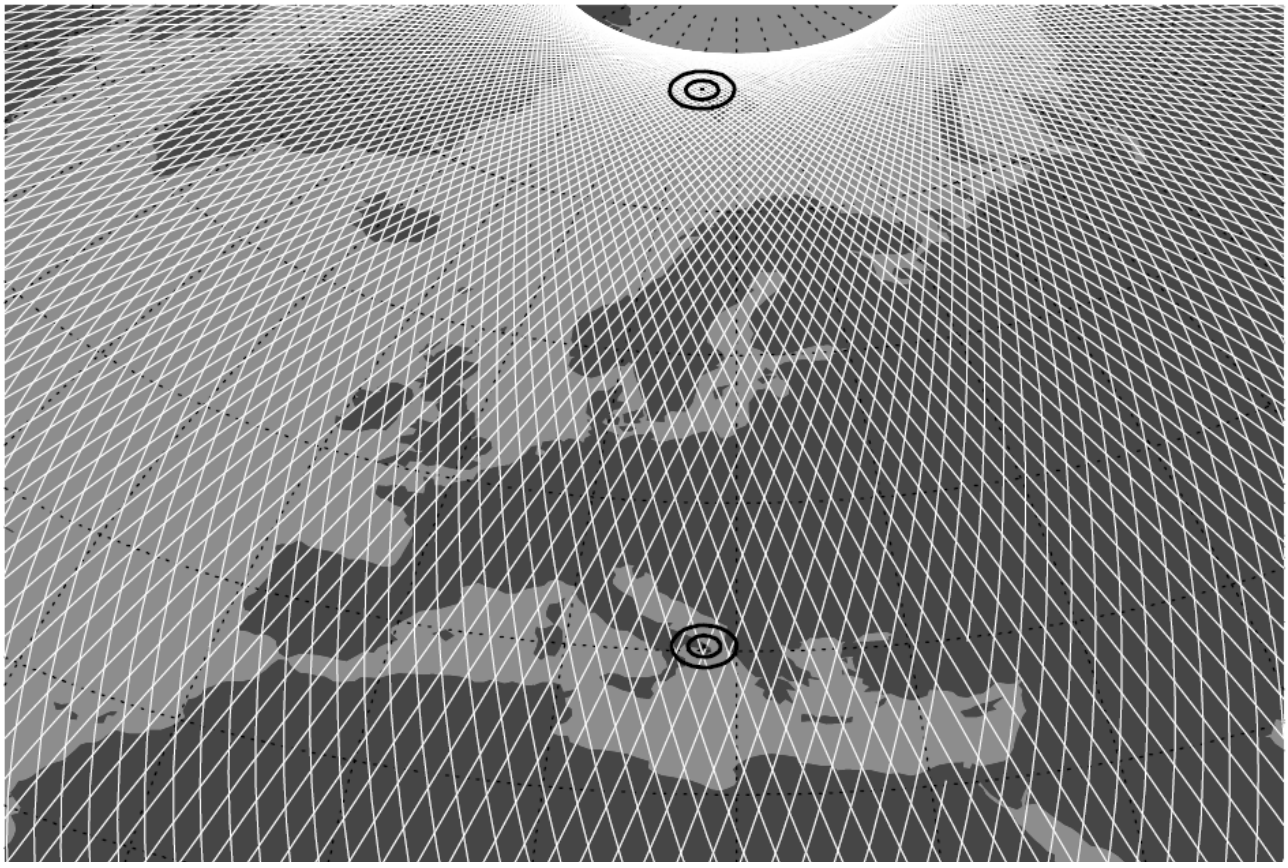

Fig. 6.2. CALIPSO 16-day repeating orbit ground tracks with circles around sites indicating 80 and 160 km distances. From Kovacs, 2002.

Combined with MODIS (**M**oderate **R**esolution **I**maging **S**pectroradiometer) and CERES (**C**louds and the **E**arth's **R**adiant **E**nergy **S**ystem) on the Aqua satellite, CALIPSO will allow observationally-derived estimates of direct aerosol forcing on regional and global scales. Furthermore, the most fruitful exploitation of CALIPSO aerosol data will involve model assimilation. Chemical transport models are now capable of generating realistic aerosol distribution from source inventories of the major aerosol species [Collins, 2001]. It has been found that model performance can be improved by assimilating observations of aerosol optical depth derived from passive satellites. Assimilation of observations provides useful constraints on the model, mitigating errors due to source, sinks, and transport processes within the model. Models currently perform poorly in predicting the vertical distribution of aerosol, and global lidar observations will provide constraints with which to test and improve model parameterizations. Correct prediction of the aerosol vertical profile is particularly important because the aerosol residence time, and thus the radiative impact, increases significantly when the aerosol is lofted above the boundary layer.
Model assimilation can also potentially be used as a sophisticated interpolation scheme to take the sparse observations from nadir-pointing lidar, and create a time-dependent, 3-D representation of the global aerosol field.

6.2. CALIOP

The **C**loud-**A**erosol **LI**dar with **O**rthogonal **P**olarization (CALIOP) is the primary instrument on the CALIPSO satellite. The design of CALIOP is shown schematically in Fig. 6.3.

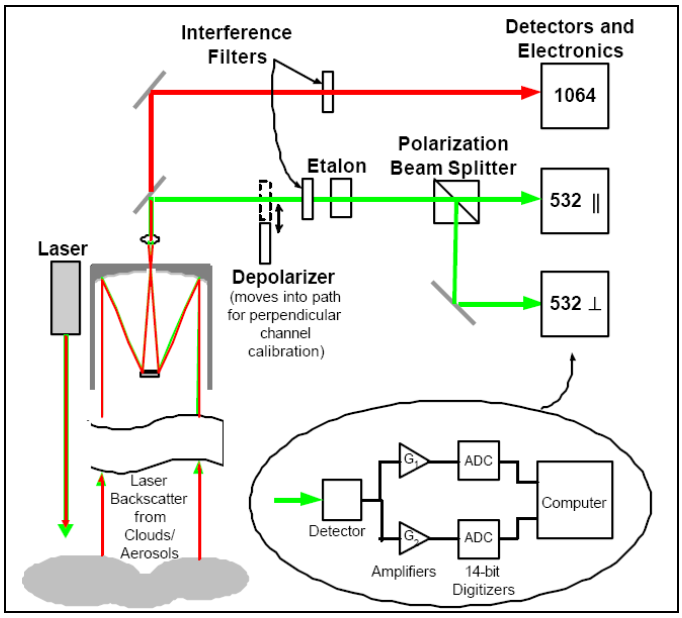

Fig. 6.3. Optical schematic of CALIOP. From Winker, 2003

A diode-pumped Nd:YAG laser produces linearly-polarized light pulses at 1064 nm and 532 nm at a repetition rate of 20.16 Hz. The laser is Q-switched to provide a pulse length of about 20 ns. Beam expanders reduce the angular divergence of the laser beam to produce a beam diameter of 90 m at the Earth's surface. The atmospheric return is collected by a 1-meter telescope which feeds a three-channel receiver measuring the backscattered intensity at 1064 nm and the two orthogonal polarization components at 532 nm (parallel and perpendicular to the polarization plane of the transmitted beam). The receiver sub-system consists of the telescope, relay optics, detectors, preamps, and line drivers mounted on a stable optical bench. A mechanism located in the collimated portion of the beam contains a shutter and a depolarizer used in calibrating the 532 nm perpendicular channel. A narrowband etalon is used in the 532 nm channel to reduce the solar background illumination.

A dielectric interference filter provides sufficient solar rejection for the 1064 nm channel. An active beamsteering system is used to ensure alignment between the transmitter and the receiver. Photomultiplier tubes (PMTs) are used for the 532 nm detectors as they provide large linear dynamic range, very low dark noise, and reasonable quantum efficiency. An avalanche photodiode (APD) is used at 1064 nm as PMT detectors have poor quantum efficiency at that wavelength. The APD has good dynamic range and quantum efficiency but the dark noise is much larger than for the PMTs. Thus, the 532 nm channels are more sensitive. CALIOP is required to accurately measure signal returns from the aerosol-free region between 30 km and 35 km as well as the strongest cloud returns. For this reason, all detectors are used in analog mode, although the electronic gains of the 532 nm channels are large enough to allow detection of single photoelectron events. The signal processing electronics have been designed so the linear dynamic range covers the full range of molecular, aerosol, and cloud backscattering encountered in the atmosphere, which covers about six orders of magnitude.

Table 2. Key CALIOP lidar parameters

Characteristic	Value
Laser:	diode-pumped Nd:YAG
pulse energy	110 mJ: 532 nm
	110 mJ: 1064 nm
pulse rate	20.2 Hz
polarization purity	> 99% (532 nm)
cooling	passive
boresight range	+/- 1 degree
beam divergence	100 μrad
Receiver:	
telescope diameter	1 meter
FOV	
detector/passband:	130 μrad
532 nm	
1064 nm	PMT/ 35 pm
	APD/ 400 pm
Spatial resolution:	
lower troposphere	333 m horiz, 30 m vert
upper troposphere	1 km horiz, 60 m vert
stratosphere	5 km horiz, 180 m vert

The fundamental sampling resolution of the lidar is 30 m vertical and 333 m horizontal. The lidar is calibrated by normalizing the return signal in between 30 km and 35 km.
Since CALIOP is an elastic lidar, it cannot provide direct measurements of both extinction and backscatter profile. It needs hypothesis on the functional dependence between the extinction and backscatter coefficient, which does not allow an independent estimation of the considered quantity.
The CALIOP Scene Classification Algorithm estimates layer-mean lidar ratios with the transmittance method [Vaughan, 2004] in case of lofted layers or selects the lidar ratio (LR) among the values for six predefined aerosol types for layers.
Otherwise to simple backscatter lidars as CALIOP, High Spectral Resolution Lidars (HSRL) and Raman Lidars do not need the critical assumption of the LR. With both techniques α and β can be derived directly and independently from each other. Thus, the EARLINET Raman lidars are an adequate tool to perform ground truth observations during CALIPSO overpasses. Direct intercomparisons between backscatter and extinction profiles measured by EARLINET Raman lidars and by CALIPSO can be used to validate and to improve the CALIOP Scene Classification.

6.3. The EARLINET strategy for CALIPSO

EARLINET represents an excellent tool to validate CALIPSO lidar data on a continental scale and acts as a single partner in the CALIPSO validation activities.
The instrumentation of the currently 25 EARLINET stations is as follows:

- Three of the stations continuously operate fully automated lidars. They are simple backscatter lidars.
- Sixteen of the EARLINET stations operate Raman lidars which allow for the independent retrieval of profiles of the particle extinction and backscatter coefficients. The particle extinction-to-backscatter (lidar ratio) contains information on particle size and particle light absorption and thus allows a rough separation among different aerosol types.
- Eight multi-wavelength Raman lidar stations belong to EARLINET. Those lidars allow for the retrieval of three backscatter coefficients at 355, 532, and 1064 nm wavelength plus two

extinction coefficients and lidar ratios at 355 and 532 nm. The wavelength dependence of the backscatter and extinction coefficients and of the lidar ratios allow for a more detailed differentiation of aerosol types. In the framework of EARLINET inversion algorithms were developed to obtain microphysical aerosol properties like effective radius, volume and surface area concentration, and real and imaginary part of the complex refractive index from multi-wavelength Raman lidar information. Backscatter coefficients at three wavelengths plus extinction coefficients at two wavelengths are the minimum required input data for such inversion schemes.

A suitable, three-stage strategy for correlative measurements has been implemented within EARLINET for the CALIPSO project. Following this strategy about 7 stations would perform measurements simultaneously with the CALIPSO overpasses over Europe. The EARLINET measurement strategy is as follows:

- **Case 1** (Mandatory). Each EARLINET station is one validation point for CALIPSO and performs measurements as close as possible in time and space to the CALIPSO overflights (see Fig. 6.4, left). According to CALIPSO validation plans, measurements made within 2 h and 40 km of the satellite overpass are preferred, but within 4 h and 80 km are acceptable.
- **Case 2** (Suggested). Beyond those simple comparisons at individual points, our network provides the unique opportunity to perform studies on the spatial and temporal variability of the aerosol field over Europe. EARLINET performs additional correlative observations at the lidar station which is closest to the actually overpassed site (see Fig. 6.4, center). Those correlative network observations produce also the data base for studies on the representativeness of the CALIPSO observations. Further they provide, together with the CALIPSO data, comprehensive data sets for detailed process studies.
- **Case 3** (Suggested). The third stage of correlative observations is designed to study the variability of microphysical aerosol properties over Europe and to support the CALIPSO aerosol type identification procedures. If a multi-wavelength Raman lidar station is overpassed then also the next closest 3+2 station performs a measurement (see Fig. 6.4, right).

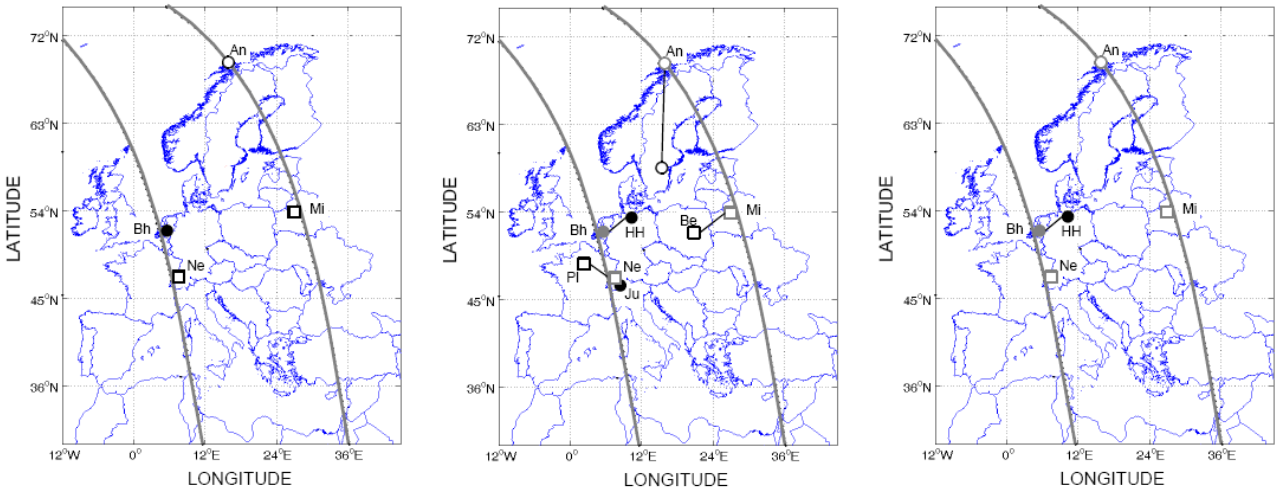

Fig. 6.4. Illustration of EARLINET measurement strategy for correlative observations during CALIPSO overpasses. The symbols indicate the different types of lidar sites, see Figure 1. The bold lines show the ground track of the satellite. Left: all stations which have to perform a case-1 observation. Center: case-1 stations (gray symbols) and the respective case-2 stations (black symbols) are connected by thin lines. Right: same as center, but for case-3 observations.

In this way, EARLINET performed more than 1000 correlative observations for CALIPSO during the first one year (June 2006 - June 2007) [Mattis, 2007].
Further the EARLINET Raman lidars, especially the multi-wavelength Raman lidars allow for the retrieval of an aerosol model which describes aerosol-type dependent lidar ratios which were derived only from vertically resolved lidar observations under ambient conditions. This is in contrast to the actually aerosol model of the CALIOP retrievals where the different aerosol types and its corresponding lidar ratios were mainly defined from column-integrated Sun photometer observations or from in-situ measurements.

At Naples EARLINET station correlative measurements have been performed starting from the beginning of June 2006. For the first year (June 2006 - June 2007), 95 measurement runs have been performed in coincidence with the CALIPSO overpasses; 45 measurements correspond to overpasses for which the distance from the lidar location and the CALIPSO footprint is lower that 50 km. During night-time measurement runs Elastic and Raman scattering from N_2 molecules are recorded as well the signal corresponding to the Raman scattering on H_2O molecule. Instead, only elastic signals at 355 nm and 532 nm are recorded during day-time measurements.

6.4. The CESC algorithm

Being CALIOP a backscatter lidar, it cannot provide direct measurements of backscatter and extinction profiles. A second equation is required to invert the lidar signal. This additional information can be obtained when a second lidar system is added, pointing in the opposite direction with respect to the first. From the returns of the two lidar systems both the spatial extinction and backscatter coefficients can be retrieved. This method, introduced by Kunz [Kunz, 1987], has been integrated, discussed in details and applied by the Naples lidar group. Other examples can be also found in Cuesta [Cuesta, 2004] and in Stachlewska [Stachlewska, 2005].
The **C**ounter-propagating **E**lastic **S**ignals **C**ombination (CESC) algorithm can be applied when two "counter looking" lidars, a ground-based and a spaceborne lidar, measure the same atmosphere column which is stable during the measurement time. An additional hypothesis is related to the assumption that the influence of the multiple scattering is negligible on both signals.
The main hypothesis for its application is that horizontal uniformity of atmosphere shall be kept for the overpass time. Beside, from the retrieved backscattering profile the overlap function of the ground-based lidar can be determined.
The CESC algorithm is now described in detail.
We indicate with $RCS_s(z)$ and $RCS_g(z)$ the range corrected total elastic backscatter signal at the same wavelength as available from spaceborne and ground-based lidar respectively. If the above mentioned hypotheses are verified, the two signals can be written as follows:

$$RCS_s(z) = k \cdot \beta(z) \cdot \exp(-2\tau_{zc}) \tag{6.1}$$

$$RCS_g(z) = k' \cdot A(z) \cdot \beta(z) \cdot \exp(-2\tau_{0z}) \tag{6.2}$$

where z is the altitude along the vertical axis (z = 0 is the ground level), k , k' include all instrumental constants of the two lidars, $\beta(z)$ is the total backscattering and $A(z)$ the overlap function of the ground-based lidar, respectively. Indicating with $\alpha(z)$ the total extinction coefficient at the altitude z, the terms $\tau_{zc} = \int_z^{z_c} \alpha(\zeta) d\zeta$ and $\tau_{0z} = \int_0^z \alpha(\zeta) d\zeta$ represent the optical depth in the range from z to the altitude z_c of spaceborne lidar and from the ground level to z, respectively.

Taking into account that z_c is of the order of several hundreds km and the altitude range in which the validation occurs is not greater than 50 km above ground, a unitary overlap function is considered.
In the case of the ground-based lidar, the overlap function is strongly variable at low altitude but it asymptotically converges to a unitary solution as a function of *z*. For this reason, the following considerations are limited to altitudes where *A(z)* can be considered approximately constant or known by other ways.
Therefore, the product of the two signals can be written as:

$$P(z) = RCS_s(z) \cdot RCS_g(z) = k'' \cdot \beta^2 \cdot (z) \cdot \exp\left[-2(\tau_{zc} + \tau_{0z})\right] \tag{6.3}$$

where $k'' = k \cdot k'$ is a constant.
Indicating with τ_{0c} the optical depth from the ground level to z_c ($\tau_{0z} + \tau_{zc} = \tau_{0c}$), the backscattering coefficient can be derived as:

$$\beta(z) = \sqrt{\frac{P(z)}{K}} \tag{6.4}$$

where P(z) is the product of the two signals.
In Eq. 6.3 the quantity $\exp(-2\tau_{0c})$ has been included in the constant K, which can be determined by considering an altitude level z* at which the total backscattering β(*z**) is known. If the altitude z* is chosen within an aerosol free region the total backscattering coefficient is determined from a pure molecular atmospheric model $\beta(z^*) = \beta_m(z^*)$, and the backscattering at *z* is obtained as:

$$\beta(z) = \beta_m(z^*) \cdot \sqrt{\frac{P(z)}{P(z^*)}} \,. \tag{6.5}$$

Thus the particle backscattering $\beta_p(z)$ is given by:

$$\beta_p(z) = \beta(z) - \beta_m(z). \tag{6.6}$$

In Eq. 6.5 *P(z*)* is evaluated by fitting *P*(*z*) to $\beta_m(z)$ in the aerosol free range around z*. In this way the uncertainty in the retrieval can be kept as low as 2-5 % even if the z* value is chosen at a high altitude where the signal from ground-based lidar is weak.
Let us consider the ratio of Eqs. 6.1 and 6.2:

$$R(z) = \frac{RCS_s(z)}{RCS_g(z)} = \frac{k}{k'} \cdot \exp\left[-2(\tau_{zc} - \tau_{0z})\right] = \frac{k}{k'} \cdot \exp(-2\tau_{0c}) \cdot \exp(4\tau_{0z}) \tag{6.7}$$

Thus, the optical depth between two levels z_1 and z_2 is given by:

$$\tau(z_2 - z_1) = \frac{1}{4}\left[\ln R(z_2) - \ln R(z_1)\right] \tag{6.8}$$

and the particle extinction coefficient $\alpha_p(z)$ is evaluated by differentiating Eq. 6.7 with respect to z and subtracting the molecule extinction $\alpha_m(z)$:

$$\alpha_p(z) = \frac{1}{4}\frac{d}{dz}\left[\ln R(z)\right] - \alpha_m(z) \tag{6.9}$$

6.5. Simulation

Both ground-based and spaceborne lidar signals have been simulated in order to test the algorithm.
Air density and the Rayleigh scattering coefficient are simulated from a standard atmospheric model (U.S. Standard Atmosphere) fitted to standard temperature and pressure values (20°C, 1 bar) at ground level. Below 1.5 km of altitude, a typical planetary boundary layer (referred as PBL, hereinafter) aerosol (β = 1-5×10^{-6} sr^{-1} m^{-1}) with LR = 70-80 sr [Cattrall, 2005] was simulated. From 3 to 5.5 km two aerosol layers, separated by 0.5 km, are included in order to simulate lofted layers of Saharan desert mineral dust (LR = 40 sr) [Mona, 2006] and to verify the spatial resolution of the algorithm. A cirrus cloud (β = 8×10^{-6} sr^{-1} m^{-1}, LR = 30 sr) [Chen, 2002] is also simulated in the 9-10 km altitude range. In the simulated signals, only the statistic error is considered. The laser energy is chosen in order that the simulated lidar signals have a comparable signal-to-noise ratio with real signals integrated on 10 minutes for ground-based and 10 seconds for spaceborne lidars, respectively, having as reference the CALIPSO lidar. In fact, it can be reasonably assumed that during 10 minutes the atmosphere is stable and that it is homogeneous along about 60 km of the CALIPSO ground-track covered in 10 seconds. In the simulation a vertical resolution of 60 m is considered for both ground-based and spaceborne lidars.
Laser wavelength of 532 nm was used in the simulation even though the algorithm is wavelength independent. Here, only single Rayleigh and Mie scattering from pure molecules and aerosol, or clouds, are considered. In the retrieval of both backscattering and extinction profiles no data filtering is applied. The numerical derivative in Eq. 6.9 is obtained through the application of a linear fit on 5 data points up to 2 km and on 9 data points above this altitude. This corresponds to a vertical resolution of the extinction profile of about 200 m and 350 m up to 2 km and above this altitude, respectively.
Simulated RCS from ground-based and spaceborne lidars are shown in Fig. 6.5(a). Due to the very high dynamic range of the RCS_g with respect to RCS_s (hereinafter, referred as ABS from the CALIPSO data product's name), the signal-to-noise ratio of ground-based lidar RCS_g varies very much from low to high altitude while spaceborne lidar ABS fluctuations remain of the same order. This is related to the fact that it is very difficult to improve the RCS signal-to-noise ratio by increasing the laser energy avoiding signal saturation in the near range.
In Fig. 6.5(b) the backscatter coefficient profile retrieved from Eq. 6.6 by considering a reference height z* in the range 10-12 km is shown; it perfectly overlaps the exact solution.
Also the extinction coefficient profile from Eq. 6.9 [reported in Fig. 6.5(c)], agrees quite well with the solution, even if it has more uncertainties and worse spatial resolution. The averaged LR for both aerosol and cloud layer agree with the solution quite well with a standard deviation ranging from 10% for PBL aerosol to 15% for cirrus cloud.

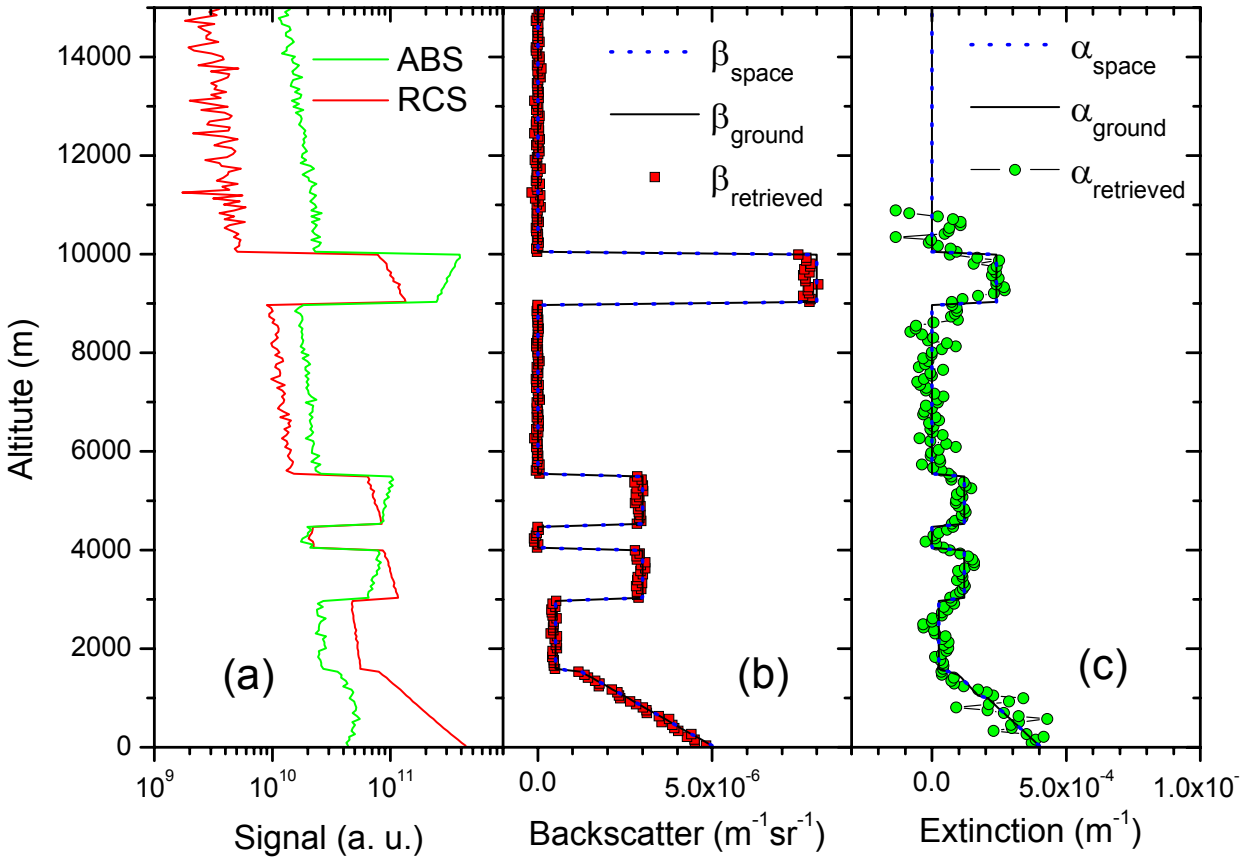

Fig. 6.5. Simulated RCS from ground-based lidar (red line) and spaceborne lidar (green line) signals (a); retrieved aerosol backscatter coefficient (dots and line, respectively) and its solution (red square) (b); retrieved aerosol extinction coefficient (dots and line, respectively) and its solution (green circle) (c). The vertical resolution of the two RCS is 60 m.

6.6. Application to real data

The CESC algorithm is applied also to real data from CALIPSO and the Naples lidar station.

6.6.1 First case

On 20th August 2006, a CALIPSO overpass happened around 01:17:24 UT (Universal Time) and the distance from the Naples lidar station and the CALIPSO footprint track was about 50 km. This distance is lower than the typical aerosol air masses correlation scales (50-100 km) [Anderson, 2003].

During this measurement a wide soil dust layer was detected from lidar measurements. The layer base was situated at 1.5 km height extending up to 8.5 km. Analytical back-trajectories from HYSPLIT model [Draxler, 2003] show that the origin of incoming air masses at these altitudes was located above the Sahara desert.

As shown in paragraph 6.4, the CESC algorithm does not require normalization or calibration of range corrected signals for its application; nevertheless, in the analysis of this case study, the total

attenuated backscatter signal (ABS) (range-scaled, energy and gain normalized) at 532 nm, as available from CALIPSO products and the range corrected signal (RCS) at the same wavelength from the ground-based lidar in Naples have been considered.
The RCS temporal and spatial evolution in Fig. 6.6(a) at 532 nm shows that the main hypothesis of atmospheric stability is rather well verified close to the spacecraft overpass (pink line). Horizontal homogeneity of aerosol layer was also checked by observing the Sea WiFS images [Sea WiFS website], which clearly show the Saharan dust layer covering all the Mediterranean Sea. Moreover, the CALIPSO ABS map in Fig. 6.6(b) shows that close to Naples, CALIPSO looks at a cloud free region as well, while the dust layer thickness was almost stable during the time interval considered in the analysis. The thick pink line marks the overpass of the CALIPSO spacecraft.
In the application of CESC algorithm an integration of signals has been performed in order to increase the signal to noise ratio (SNR). The choice of the number of CALIPSO profiles to integrate has been done by taking into account the distance of the spacecraft ground track to the lidar station. 326 CALIPSO profiles (~ 10 seconds) have been averaged because this corresponds to a footprint path of the order of the distance between CALIPSO ground track and the position of Naples lidar station.
Signals from ground based lidar are acquired with a time resolution of 1 min. To increase the SNR, ten signals profiles (10 minutes) from ground based lidar have been averaged, centered on the overpass time.

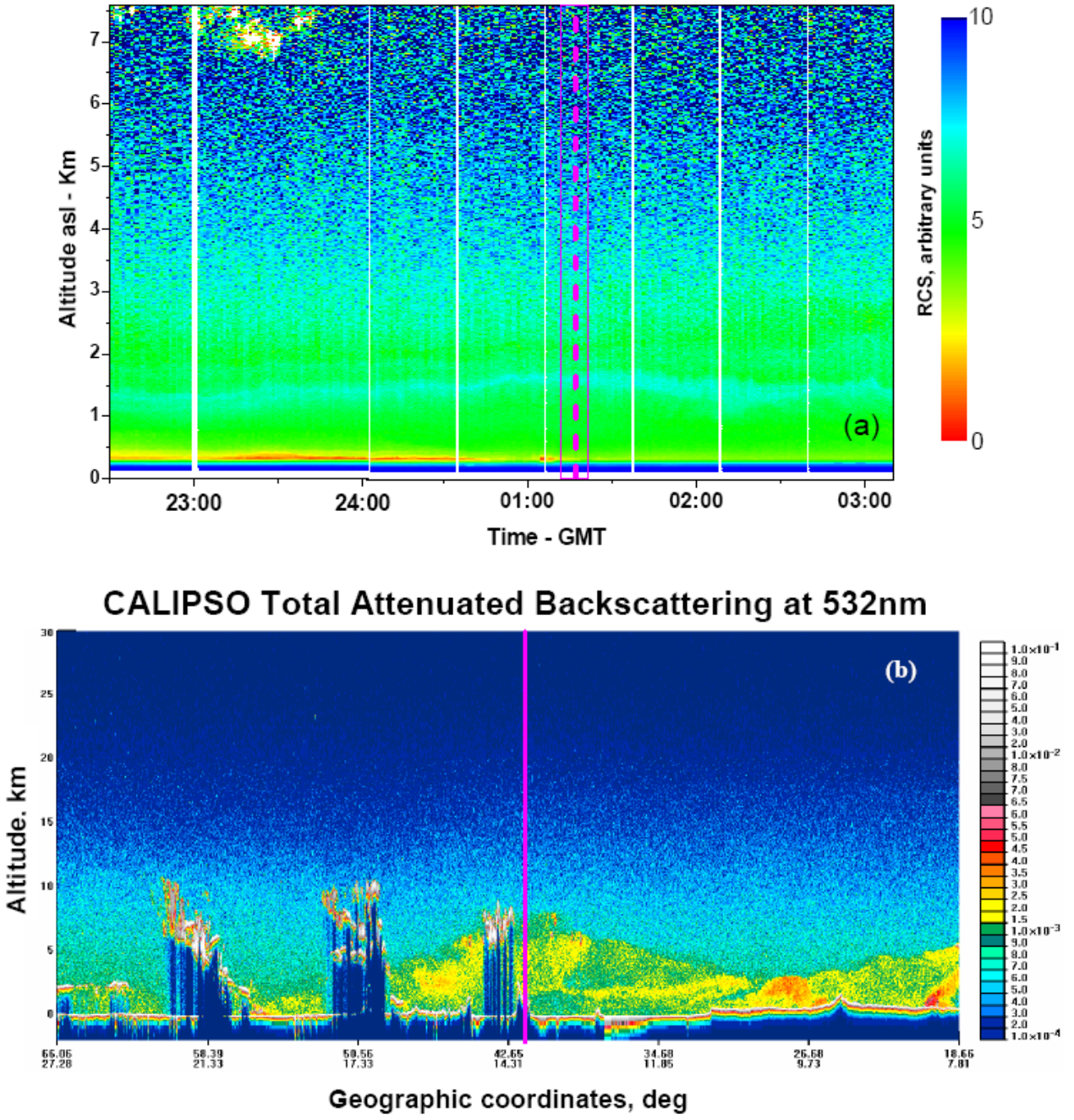

Fig. 6.6. Time series of Naples RCS profile: pink lines indicate the limits of time integration, and dash line is the overpass time (a); CALIPSO total ABS (km^{-1} sr^{-1}), measured from 20 August 2006. The thick pink line marks the overpass of CALIPSO spacecraft (b).

Fig. 6.7(a) shows the averaged total attenuated backscatter and range corrected signal profiles. Appling Eqs. 6.6 and 6.9 to these two elastic signals, the backscattering and the extinction profiles has been retrieved, respectively. The reference height has been chosen in the free aerosol region between 9 and 11 km. Errors were calculated on the basis of error propagation and assuming the error on molecular profile to be negligible. For CALIPSO ABS the standard error on the averaged profile was considered. This takes into account both the statistical error on single profile signal and fluctuations due to different atmospheric conditions sounded along the considered path of CALIPSO.

Fig. 6.7(b) shows the backscatter coefficient profile determined by the CESC algorithm and by the conventional Raman method [Ansmann, 1992]. For this calculation, the same molecular profiles

have been used. Since the two methods use different signals, the retrieved profiles are completely independent. The agreement of the two profiles is quite good. Discrepancies at the lowest heights are mainly due to atmospheric differences inside the PBL, where orography and aerosol local sources play a significant role.
Fig. 6.7(c) shows the extinction coefficient profiles retrieved by CESC algorithm and by conventional Raman method. The agreement of the two profiles is rather good.
The error bars reported in Figs. 6.7(b) and 6.7(c) account for statistical errors only and do not include the uncertainty on the pure molecular profile, which is about 2-5%.

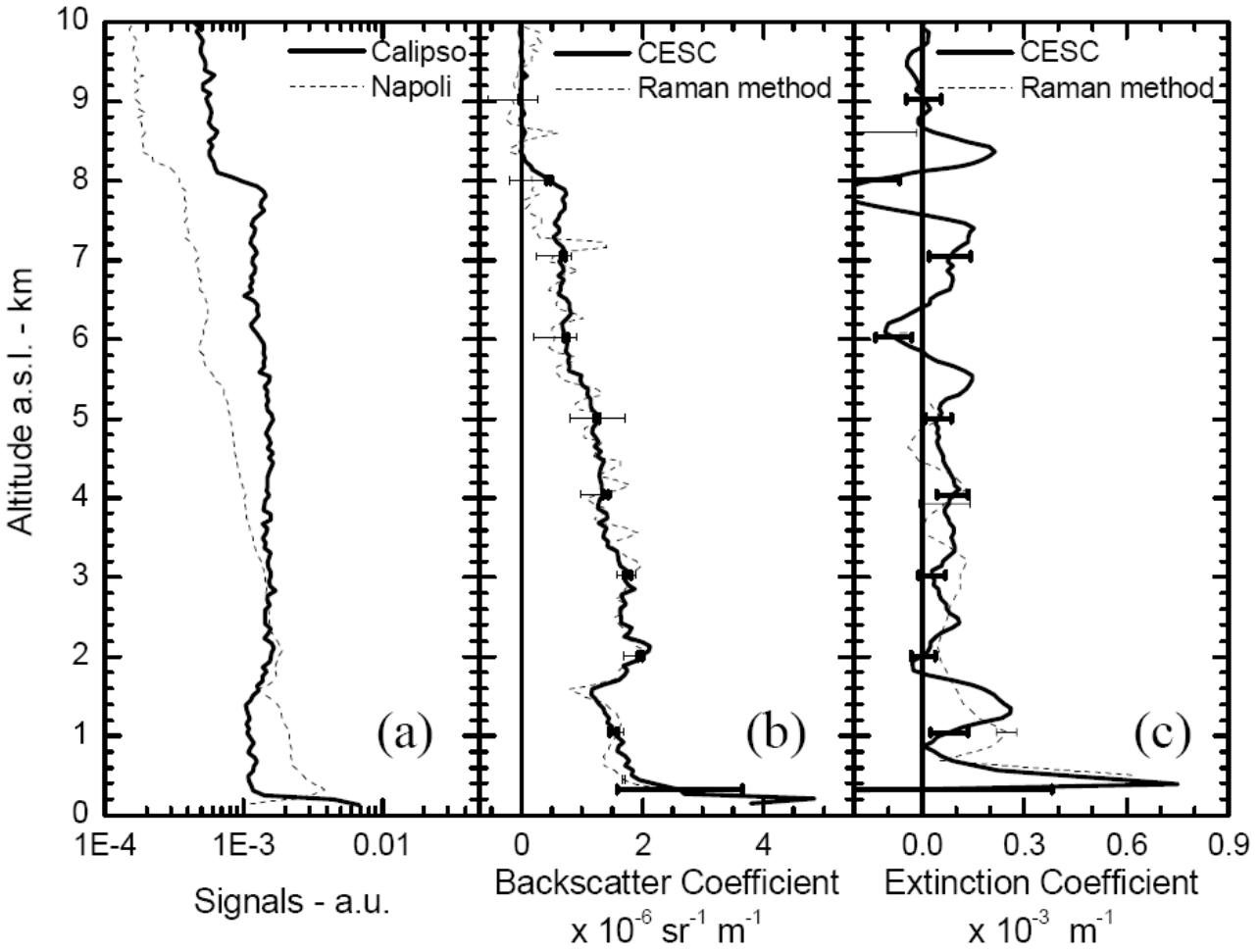

Fig. 6.7. CALIPSO ABS as obtained by averaging of 326 profiles (thick line) and RCS from Naples lidar (dash line) as obtained by averaging 10 min acquisition profiles (a); Backscatter coefficient as obtained from the CESC algorithm (thick line) and from Raman method (dash line) (b); Extinction profile from CESC (thick line) and from nitrogen Raman method (c)

6.6.2 Second case

On 22th July 2007, a CALIPSO overpass happened around 01:17:30 UT and the distance from the Naples lidar station and the CALIPSO footprint track was about 40 km. For this case, atmospheric conditions are very stable as Fig. 6.8 shows.

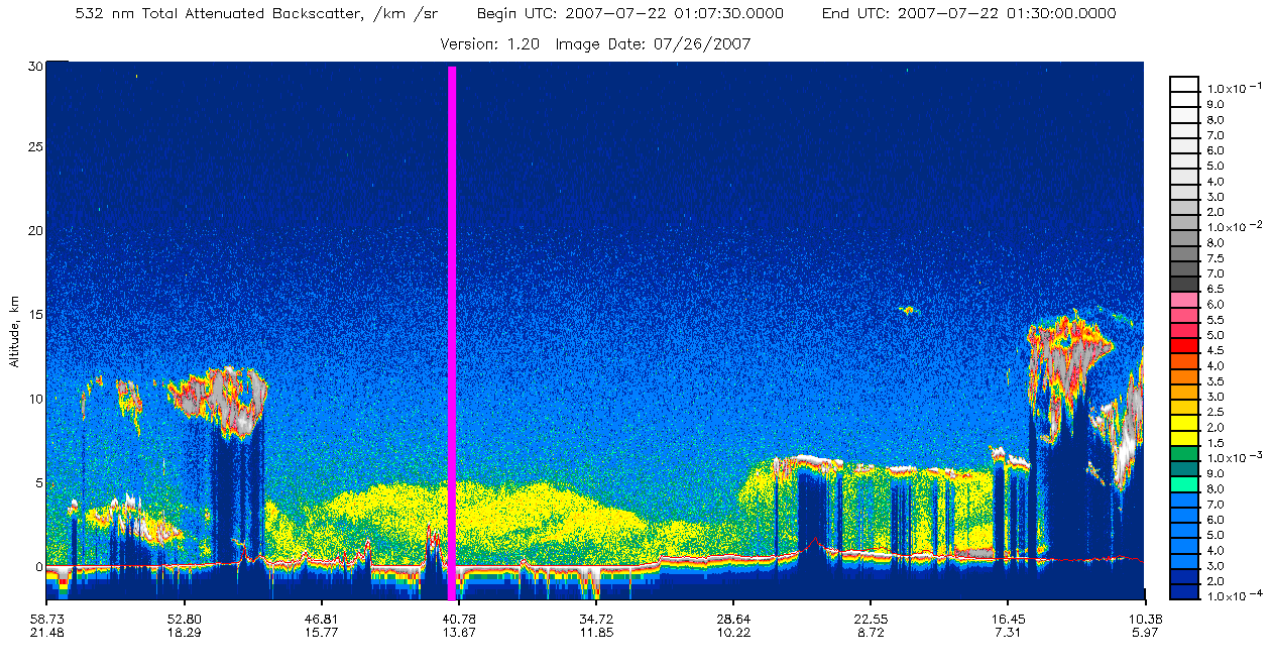

Fig. 6.8. The CALIPSO total ABS (km^{-1} sr^{-1}), measured at 22 July 2007. The thick pink line marks the overpass of CALIPSO spacecraft.

CALIPSO profiles on ~ 10 seconds, corresponding to footprint path of the order of the distance between CALIPSO ground track and the position of the Naples lidar station (~ 40 km) have been averaged. Signal from ground has been averaged on 10 minutes centered on the overpass time.
Fig. 6.9 shows the vertical profiles of the averaged total attenuated backscatter and range corrected signal (a), the backscattering coefficient (b) and the extinction coefficient (c). The two profiles have been retrieved with the same criteria of the first case (see paragraph 6.6.1).

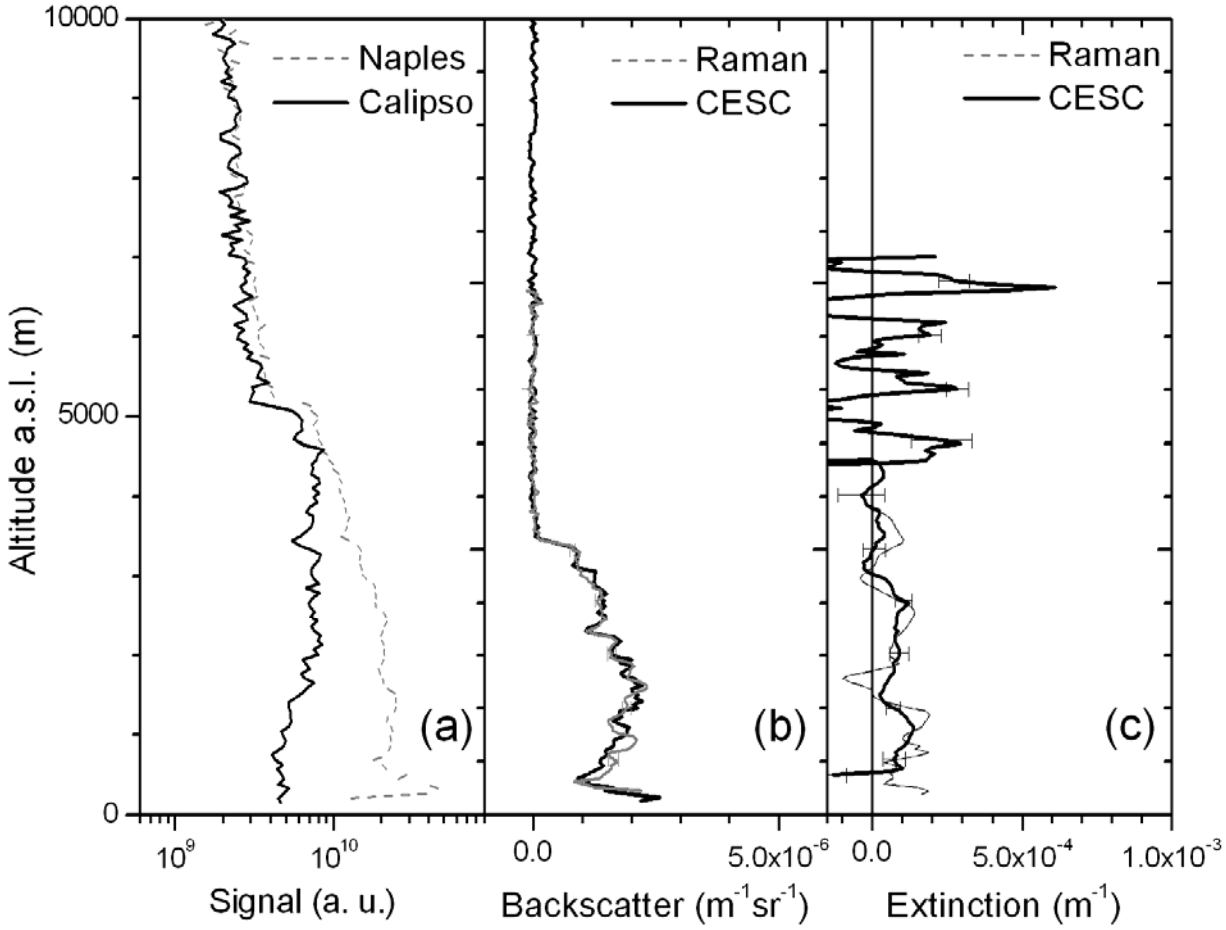

Fig. 6.9. CALIPSO ABS (line) and RCS from Naples lidar (dash) as obtained by averaging 10 min acquisition profiles (a); Backscatter coefficient as obtained from the CESC algorithm (line) and from Raman method (dash) (b); Extinction profile from CESC (line) and from nitrogen Raman method (dash) (c)

Also in this case the agreement between the backscatter coefficient profile determined by CESC algorithm and by the conventional Raman method is very good. For the extinction profile, the agreement is rather good, and the extinction profile retrieved by CESC algorithm seems to be less noisy than that retrieved by the Raman method.

6.6.2 Third case

On 26th June 2007, a CALIPSO overpass happened around 01:17:50 UT and the distance from the Naples lidar station and the CALIPSO footprint track was about 50 km. Fig. 6.9 shows the CALIPSO ABS map. The thick pink line marks the overpass of the CALIPSO spacecraft.
CALIPSO profiles on ~ 10 seconds, corresponding to footprint path of the order of the distance between CALIPSO ground track and the position of the Naples lidar station (~ 50 km) have been averaged. Signal from ground has been averaged on 10 minutes centered on the overpass time.

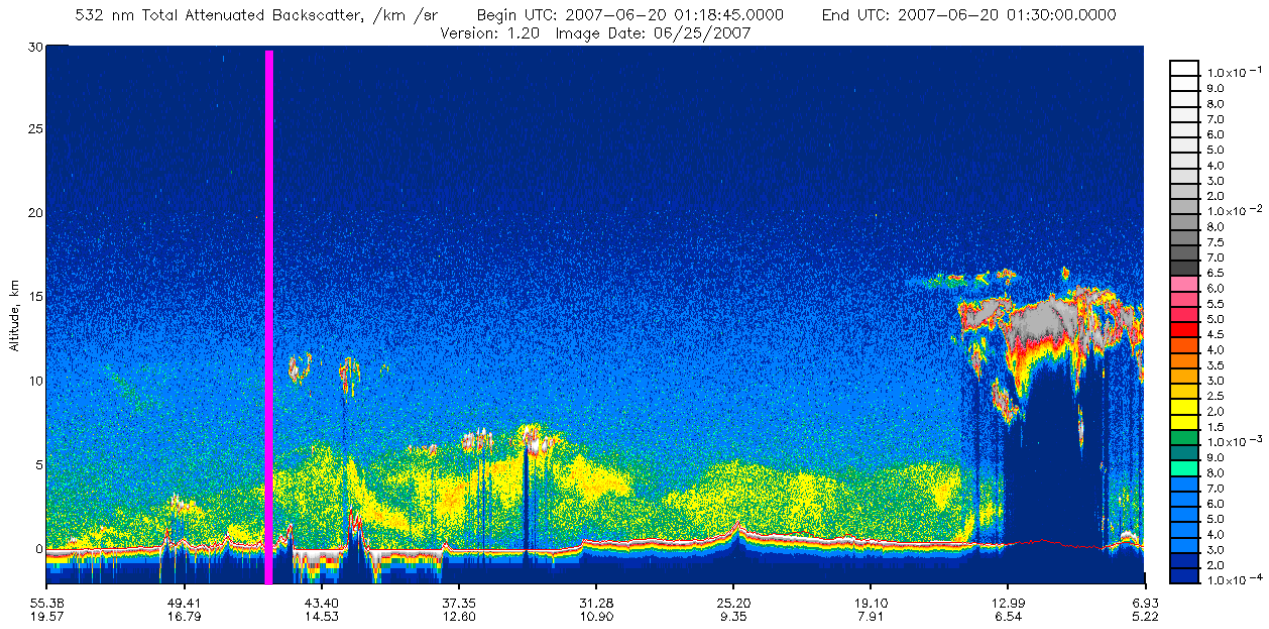

Fig. 6.10. The CALIPSO total ABS (km^{-1} sr^{-1}), measured at 26 June 2007. The thick pink line marks the overpass of CALIPSO spacecraft.

Fig. 7.1 shows the vertical profiles of the averaged total attenuated backscatter and range corrected signal (a), the backscattering coefficient (b) and the extinction coefficient (c). The two profiles have been retrieved with the same criteria of the first case (see paragraph 6.6.1).
For this case the agreement between the backscatter coefficient profile determined by the CESC algorithm and by the conventional Raman method is less good with respect to the previous cases. In fact, below 1.5 km the two backscattering profiles are different. This is probably due to inhomogeneous atmospheric conditions, which occurred during this overpass.
Also for the extinction profile, the agreement is not good.

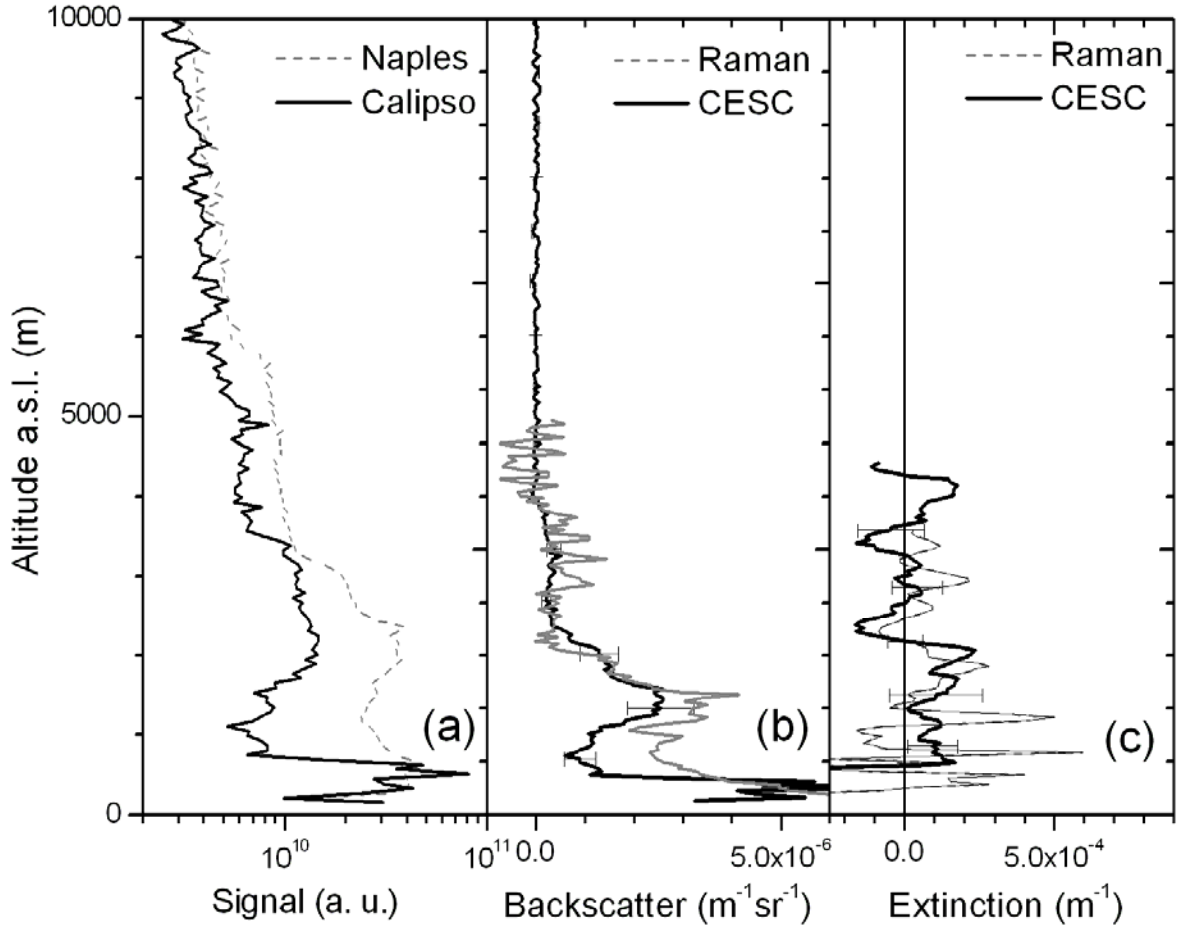

Fig. 7.1 CALIPSO ABS (line) and RCS from Naples lidar (dash) as obtained by averaging 10 min acquisition profiles (a); Backscatter coefficient as obtained from the CESC algorithm (line) and from Raman method (dash) (b); Extinction profile from CESC (line) and from nitrogen Raman method (dash) (c)

From the simulation and the application to real data, the principal features of the CESC algorithm are:

- only two "counter looking" elastic backscatter signals are needed (one from ground-based and one from spaceborne or airborne lidar);
- calibration or normalization of the signals are not required and only the presence of an aerosol-free layer is needed;
- direct retrieval of backscattering, extinction and lidar ratio profiles in the infrared region is also possible;
- taking into account that the CESC algorithm uses only elastic signals, its performances are expected to be very high also in day-time measurements.
- if ground based lidar and footprint of spaceborne lidar are very well aligned it is possible to evaluate the overlap function of ground-based Raman lidar.

As a consequence, the CESC algorithm seems to be very pioneering and useful for retrieving aerosol optical properties both from space and airborne measurements campaign.

6.7. Conclusion

In this chapter the CESC algorithm, which permits to directly retrieve the aerosol backscatter and extinction profiles from simultaneous measurements from ground-based and spaceborne lidars, is described. The algorithm is wavelength independent and it allows evaluating the lidar ratio without any assumption on particles properties. This appears extremely interesting, in particular whenever the application of Raman method is difficult or impossible, e.g. for infrared lidar.

Results of numerical simulation and application of the algorithm to real signals from ground-based and CALIPSO spaceborne lidar have been reported. In perfect atmosphere horizontally homogeneous condition, the CESC algorithm can give a perfect backscatter profile and a reasonable extinction profile.

Satellite observations are a powerful tool to global monitoring the atmosphere and study of the Earth's climate and its changes. They are able to provide a global temporal and spatial coverage and thus they facilitate the understanding of aerosol transports.

Through only satellites can provide the coverage, continuity, and consistency that climate change research requires, it would very useful also to have remote sensing data in conjunction with satellite information.

6.8. References

Anderson T. L., R. J.Charlson, D. M.Winker, J. A.Ogren, and K. Holmen, **Mesoscale variations of tropospheric aerosols**, J. Atmos. Sci. **60**, 119-136, (2003).

Ansmann A., **Ground-truth aerosol lidar observations: can the Klett solution obtained from ground and space be equal for the same aerosol case?**, Appl. Opt. **45**, 3367-3371, (2006).

Ansmann A., U. Wandinger, **Combined Raman Elastic Backscatter LIDAR for vertical profiling of moisture, aerosol extinction, backscatter and lidar ratio**, Appl. Phys. B **55**, 18-28, (1992).

Ansmann A., M. Riebesell, C. Weitkamp, **Measurement of atmospheric aerosol extinction profiles with a Raman lidar**, Opt. Lett. **15,** 746-748, (1990).

CALIPSO mission on NASA website: http://www.nasa.gov/mission_pages/calipso/main/index.html

Cattrall C., J. Reagan, K. Thome, O. Dubovik, **Variability of aerosol and spectral lidar and backscatter and extinction ratios of key aerosol types derived from selected Aerosol Robotic Network locations,** J. Geophys. Research **110**, D10S11, 10.1029/2004JD005124, (2005).

Charlson R. J., *et al.*, **Climate forcing of anthropogenic aerosols**, Science, **255**, 423-430, (1992).

Chen W., C. Chiang, and J. Nel, **Lidar ratio and depolarization for cirrus clouds**, Appl. Opt. **30**, 6470- 6476, (2002).

Collins W. D., et al., **Simulating aerosols using a chemical transport model with assimilation of satellite aerosol retrievals: Methodology for INDOEX**, *J. Geophys. Res. 106*, pp. 7313-7336, (2001).

Cuesta J. and P. H. Flamant, **Two-stream lidar inversion algorithm for airborne and satellite validations**, in *Proceedings of 22nd International Laser Radar Conference (ILRC 2004)*, G. Pappalardo and A. Amodeo, eds., *ESA SP-561* **1**, pp. 471–474, (2004).

Draxler U., G.D.v Rolph NOAA ARL HYSPLIT model. NOAA/Air Resource Laboratory, Silver Spring, MD, http://www.arl.noaa.gov/ready/hysplit4.html, (2003).

EARLINET website: http://www.earlinet.org/

Matthis I., L. Mona, D. Muller, G. Pappalardo, **EARLINET correlative measurements for CALIPSO**, Proceedings SPIE Europe Remote Sensing 2007 (*in press*).

Kiehl J. T. and B. P. Brieglieb, **The relative roles of sulfate and aerosols and greenhouse gases in climate forcing**, *Science 260*, pp. 311-314, (1993).

Klett J. D., **Lidar inversion with variable backscatter/extinction ratios**, Appl. Opt. **24**, 1638-1643, (1985).

Kovacs, *et al*., **Cloud Aerosol Lidar and Infrared Pathfinder Satellite Observations (CALIPSO) Quid Pro Quo Validation**, 12th ARM Science Team Meeting Proceedings, (2002).

Kunz, **Bipath method as a way to measure the spatial backscatter and extinction coefficients with lidar**, *Applied Optics* **26***,* 794-795, (1987).

Fernald F. G., B. J. Herman, and J. A. Reagan, **Determination of aerosol height distributions by Lidar**, Journal of Applied Meteorology **11**, 482-489, (1972).

Matthias V. et al., **Aerosol lidar intercomparison in the framework of the EARLINET project. 1. Instruments**, Appl. Opt. 43, pp. 961–976, (2004).

Muller D., U. Wandinger, and A. Ansmann, **Microphysical particle parameters from extinction and backscatter lidar data by inversion with regularization: theory**, Appl. Opt. 38(12), pp. 2346–2357, (1999).

Omar A.H., J.-G. Won, D. M. Winker, S.-C. Yoon, O. Dubovik, and M. P. McCormick, **Development of global aerosol models using cluster analysis of Aerosol Robotic Network (AERONET) measurements**, J. Geophys. Res, **110**, D10S14, doi:10.1029/2004JD004874, (2005).

Pappalardo G. et al., **Aerosol lidar intercomparison in the framework of the EARLINET project. 3. Raman lidar algorithm for aerosol extinction, backscatter, and lidar ratio**, Appl. Opt. 43, pp. 5370–5385, (2004).

Platt C. M. R., **Lidar and Radiometric Observations of Cirrus Clouds**, J. Atmos. Sci. **30**, 1191-1204, (1973).

Quid Pro Quo website: http://calipsovalidation.hamptonu.edu/

Ramanathan V., et al., **Aerosols, climate, and the hydrological cycle**, *Science 294*, pp. 2119-2124, (2001).

Randall D. A., T. G. Corsetti, Harshvardhan, and D. A. Dazlich, **Interactions among radiation, convection, and large-scale dynamics in a general circulation model**, *J. Atmos. Sci. 46*, pp. 1943-1970, 1989.

Sea WiFS website http://oceancolor.gsfc.nasa.gov/SeaWiFS/

Spinhirne J. D., *et al.*, **Cloud and aerosol measurements from GLAS: Overview and initial results**, J. Geophys. Res **32**, L22S03, doi:10.1029/2005GL023507 (2005)

Stachlewska I. S., Ritter C. and Neuber R., **Application of the two-stream inversion algorithm for retrieval of extinction, backscatter and lidar ratio for clean and polluted Arctic air, Lidar Technologies, Techniques, and Measurements for Atmospheric Remote Sensing**, edited by Upendra N. Singh, Proc. of SPIE Vol. 5984, 598403, (2005) · 0277-786X/05/$15 · doi: 10.1117/12.629317 Proc. of SPIE Vol. 5984 598403-1.

Troy Anselmo, *et al.*, **Cloud – Aerosol LIDAR Infrared Pathfinder Satellite Observations, Data Management System and Data Products Catalog**, Release 2.2 Document No. PC-SCI-503, (2006).

Twomey S. A., M. Piepgrass, and T. L. Wolfe, **An assessment of the impact of pollution on the global albedo**, *Tellus 36B*, pp. 356-366, (1984).

Vaughan M.A., *et al.*, **CALIOP Algorithm Theoretical Basis Document**, PS-SCI-202 Part 2.

Vaughan M., *et al*., **Fully automated analysis of space-based lidar data: an overview of the CALIPSO retrieval algorithms and data products**, Proc. SPIE **5575**, 16-30, (2004).

Vaughan M., **Algorithm for retrieving lidar ratio at 1064 nm from space-based lidar backscatter**, Proc. SPIE **5240**, 104-115, (2004).

Veselovskii I., A. Kolgotin, V. Griaznov, D. M¨uller, U. Wandinger, and D. N. Whiteman, **Inversion with regularization for the retrieval of tropospheric aerosol parameters from multiwavelength lidar sounding**, Appl. Opt. 41, pp. 3685–3699, (2002).

Wandinger U., D. Müller, C. Böckmann, D. Althausen, V. Matthias, J. Bösenberg, V. Weiß, M. Fiebig, M. Wendisch, A. Stohl, and A. Ansmann, **Optical and microphysical characterization of biomass-burning and industrial-pollution aerosols from multiwavelength lidar and aircraft measurements**, J. Geophys. Res. **107**, 10.1029/2 000JD000202, (2002).

Wang X., Frontoso M.G., Pisani G., Spinelli N.: **Retrieval of aerosol optical properties by combining ground-based and space-born lidar elastic scattering profiles,** Optic Express, **15**, Iss. 11, 6534-7094, (2007).

Wang X., Armenante M., Frontoso M.G., Pisani G., Spinelli N.: **CALIPSO correlative measurements at Napoli EARLINET station,** Proceedings SPIE Europe Remote Sensing 2007 (*in press*).

Winker D. M., R. H. Couch, and M. P. McCormick, **An overview of LITE: NASA's Lidar In-space Technology Experiment**, *Proc. IEEE* **84**, 164-180, (1996).

Winker D. M., J. R. Pelon, and M. P. Cormick, **The CALIPSO mission: spaceborn lidar for observation of aerosols and clouds**, Proc. SPIE **4893**, 1-11, (2003).

Winker D. M., W. Hunt, and C. Hostetler, **Status and performance of the CALIOP lidar**, Proc. SPIE **5575-3**, (2003).

Conclusions

The focus of the present thesis was to investigate, measure, and analyze the optical properties of the atmospheric aerosol on different spatial scales through the remote sensing lidar technique.
In addiction to the lidar technique, in the present thesis also satellite lidar data and numerical models are used for the study of aerosols. Experiments-and-observations and data analysis have been performed during the PhD research project.

A short description of the atmospheric physical properties has been done, emphasizing some aspects with respect to aerosols. Then, the interaction between atmospheric components and sounding light was drawn: the different kinds of atmospheric scattering have been discussed as well as the extinction of the light. The remote sensing lidar technique has been introduced, describing the fundamental equations, the optical parameters that can be retrieved, and the main inversion algorithms. Afterwards, the multiwavelenghts Raman lidar system located in Naples has been described in detail.
Due to the properties of the interaction between the radiation and the atmosphere, the lidar technique has demonstrated to be a powerful tool to measure and monitor the optical parameters of the atmosphere with high spatial and temporal evolution. The knowledge of the aerosol optical parameters is very important because it permits to extract information about the aerosol distribution. Aerosols have been studied on different spatial scales.

Measurements on local scale are very important because they provide information which is generally parameterized by models. Two field campaigns have been performed and the observations show interesting results which could be assimilated by models. Using aerosol as tracers, it was possible to determine the temporal evolution of the planetary boundary layer height both for urban and rural sites.

A comprehensive analysis of the aerosol vertical distribution over the western and central Mediterranean during Saharan Dust episodes, by the synergy between model and lidar data has been realized. The aerosol extinction vertical distribution simulated by the **D**ust **RE**gional **A**tmospheric **M**odel (DREAM) has showed a rather good agreement with the lidar profiles both in Barcelona and in Naples. At low height, the deviations between model and lidar data are reasonably due to the local and/or anthropogenic aerosols that contribute significantly to the measured aerosol extinction.
Collecting several complementary information as geopotential, surface temperature and wind fields, backtrajectories and satellite observations, the synoptic situation associated with Saharan Dust episodes over the western and central Mediterranean has been studied.
The DREAM model has also demonstrated to be able to reproduce the main seasonal features of the Saharan Dust vertical distribution over the western and central Mediterranean. The major differences in Saharan Dust concentration between the western and the central Mediterranean have been found in spring, in agreement with the Sharav cyclone, which moves the Saharan Dust toward eastern Mediterranean. In summer and autumn, the Saharan Dust concentration is approximately the same, but in autumn the dust plume is at higher height in western than in central Mediterranean.

Satellite observations are a powerful tool to global monitor the atmosphere and study of the Earth's climate and its changes, because they are able to provide a global temporal and spatial coverage. Though only satellites can provide the coverage, continuity, and consistency that climate change research requires, it would very useful also to have ground-based data in conjunction with satellite information. The synergy between ground-based and spaceborne lidars permits to investigate the optical properties of atmospheric aerosol on large scale.
In the framework of the CALIPSO (**C**loud-**A**erosol **L**idar and **I**nfrared **P**athfinder **S**atellite **O**bservation) satellite mission, several measurements have been performed by the Naples lidar

system in coincidence with the satellite's overpasses. An algorithm CESC (CESC, **C**ounter-propagating **E**lastic **S**ignals **C**ombination), which permit to directly retrieve the aerosol backscatter and extinction profiles from simultaneous measurements from ground-based and spaceborne lidars, has been realized. The algorithm is wavelength independent and it allows evaluating the lidar ratio without any assumption on particles properties. This appears extremely interesting, in particular whenever the application of Raman method is difficult or impossible, e.g. for infrared lidar. Results of numerical simulation and application of the algorithm to real signals from ground-based and CALIPSO spaceborne lidar are very encouraging.

All the promising results in the present thesis encourage the continuation of the work; they show the importance of the remote sensing lidar technique for the study of the atmospheric aerosols.
They are also intended to stimulate focus upon specific issues requiring detailed follow-up studies.
In the framework of the CALIPSO campaign, many works are already in progress: (1) a sensitivity analysis of the CESC algorithm; (2) the application of the CESC algorithm to the 1064-nm wavelength; (3) a statistical analysis of the CALIPSO data products in the area of Naples.
Moreover, in order to better understand the Saharan Dust vertical distribution over the Eastern Mediterranean, also lidar data from the Athens EARLINET station and model simulation will be analyzed.
Furthermore, more technical aspects mainly related to the upgrade of the experimental setup will be also performed. Another two channels will be implemented: the elastic channel in the infrared and the depolarization channel in the visible. This permits a very good opportunity to applied data inversion algorithm in order to have a more complete characterization of the microphysical properties of the aerosol.

Acknowledgment

First, I thank my tutor prof. Nicola Spinelli, who dedicated his time for supporting me during my Ph.D. research project. He showed me different ways to approach a research problem. He also taught me how to show scientific data into academic papers.

I also thank Dr. Wang Xuan for helping me at any time. Its dedication for science was a constant encouragement during my PhD research project.

A special thanks goes to my co-tutor, prof. Adolfo Comerón, who gave me useful and interesting suggestions to improve the writing of my thesis. I also thank him and all the "Barcelona-staff" for their help to accomplish my scientific goals and the accommodation they reserved me during my period in Barcelona.

The beautiful atmosphere of the Atom laboratory (Mario, Libera, Yiming, Xiaomei, Marina, Alessia e Annalisa) has kept me in good mood. Thanks, Atomers!

Last, but not least, I thank my family: my parents Antonio e Lina, my sister Imma and my brother Paolo for their confidence in me and their unconditional support to pursue my interests.

During the PhD research project, I was partly supported by the European Commission under the EARLINET-ASOS project (EU Coordination Action, contract nº 025991 (RICA)) and by the University of Naples "Federico II" for the Short Mobility Research grant.